Osaka University

Doctoral Thesis

Dynamical property of charmonia and charm quark diffusion coefficient at finite temperature in quenched lattice

Author:
Atsuro Ikeda

Supervisor:
Prof. Dr. Masayuki Asakawa

A thesis submitted in fulfillment of the requirements for the degree of Doctor of Science

in the

Nuclear Theory Group
Department of Physics

February 2, 2017

OSAKA UNIVERSITY

Abstract

Graduate School of Science
Department of Physics

Doctor of Science

Dynamical property of charmonia and charm quark diffusion coefficient at finite temperature in quenched lattice

by Atsuro IKEDA

We study in-medium properties of charmonia at the finite temperature and charm quark diffusion coefficient on quenched lattices.

We reconstruct the spectral functions with nonzero momenta from the lattice Euclidean correlators with the maximum entropy method. The properties of charmonia, especially their dispersion relation and weight of the peak, are analyzed with the maximum entropy method together with the errors estimated probabilistically in this method. We find significant increase of the masses of charmonia in medium. It is also found that the functional form of the charmonium dispersion relations is not changed from that in the vacuum within the error even at $T \simeq 1.6T_{\rm c}$ for all the channels we analyzed.

We also study the transport property of charm quarks by analyzing the momentum dependence of the current-current Euclidean correlator in temporal channel. The diffusion coefficient and relaxation time are analyzed by imposing moderate assumptions on the form of the spectral function. We obtain inequalities which constrain these transport coefficients using the momentum derivatives of the Euclidean correlator in temporal channel. Numerical simulation is performed in SU(3) gauge theory for $1.7 < T/T_{\rm c} < 4.7$. It is demonstrated that the transport coefficients are nicely constrained by the inequalities and the numerical results.

Contents

List of Figures

List of Tables

Chapter 1

Introduction

The nuclei are formed by protons and neutrons. Since the protons have positive electric charge, to form the nuclei there must exist a "strong" force between nucleons enough to resist the electric repulsive force. The force is called the strong force and the interaction between quarks, gluons and their composites, the so-called hadrons, is called the strong interaction. The strong interaction is described by Quantum Chromodynamics (QCD), which is clarified as SU(3) gauge theory. QCD is on the basis of Yang-Mills theory [1]. In 1954, C. N. Yang and R. L. Mills extended the gauge theory to non-Abelian group. Renormalizability of Yang-Mills theory was proved by G. 'tHooft in 1971 [2, 3]. Furthermore asymptotic freedom in Yang-Mills theory was proved by F. Wilczek and D. Gross [4], and independently H. D. Politzer [5]. Since quarks and gluons are confined in hadrons in the low temperature and low baryon density, we cannot extract "one" quark from a hadron. Asymptotic freedom can explain this phenomena. Coupling constant in a quantum field theory is "running", which means that an effective coupling constant varies depending on the energy scale. In the asymptotic free theory, the running coupling constant goes small at short-distance. This property can explain that quarks are confined in hadrons. On the other hand, in 1964, the quark model was proposed by M. Gell-Mann [6] and G. Zweig [7] independently. In 1965, M. Y. Han and Y. Nambu introduced the new degree of freedom "color" to explain the three s-quark state Ω [8], whose existence is prohibited by Pauli exclusion principle without the new degree of freedom. After these discoveries, QCD have been known as the fundamental theory of the strong interaction. Since QCD is a strongly coupled theory, a standard technique for a quantum field theory, the perturbation, can be applied only to the asymptotic free region, such as a calculation of a parton distribution function. When we study the strongly coupled region of QCD, we have to employ a non-perturbative method.

The hadrons consist of two type colorless composites; the baryons, as which the proton and neutron are classified, are the composite of the three quarks and the mesons are the composites of the quark and anti-quark. Especially the mesons consist of the quark and its anti-particle are called the quarkonia. Today the number of the flavors of the quarks is known as six, the up, down, strange, charm, bottom, and top quarks. The masses and charges of quarks are shown in Table. 1.1. The quarks have fractional charges and the hadrons have integer charges. From the table, we can see that the scales of the quark masses are different. The up and down quarks are called the light

TABLE 1.1: Quark masses and charges in $\overline{\text{MS}}$ scheme [9].

Flavor	mass	charge
up	$2.2^{+0.6}_{-0.4}$ MeV	$2/3$
down	$4.7^{+0.5}_{-0.4}$ MeV	$-1/3$
charm	1.27 ± 0.03 GeV	$2/3$
strange	96^{+8}_{-4} MeV	$-1/3$
top	160^{+5}_{-4} GeV	$2/3$
bottom	$4.18^{+0.04}_{-0.03}$ GeV	$-1/3$

quarks. The strange quark mass is larger than the light quark mass. However, since the strange quark mass is smaller than $\Lambda_{\rm QCD}$, one sometimes can treat the up, down, and strange quark masses are degenerating. The charm and bottom are called the heavy quarks. The existence of the charm quark is predicted by S. Glashow, J. Iliopoulos, and L. Maiani in 1970 [10]. In 1974 the first discovered charmed particle, J/ψ meson, which is the bound state of the charm quark and its anti-particle ($c\bar{c}$), was discovered at the Stanford Linear Accelerator Center [11] and at the alternating-gradient synchrotron at Brookhaven National Laboratory (BNL) [12]. The existence of the bottom and top quarks are predicted by M. Kobayashi and T. Maskawa [13]. In 1977 Υ, $b\bar{b}$ meson, was discovered at Fermilab [14]. The top quark was discovered by CDF [15] and D0 [16] experiments at Fermilab in 1995.

As we mentioned in the above paragraphs, the quarks and gluons are confined in the hadrons in our Universe. However, the quarks and gluons can be deconfined in some extreme conditions because of the asymptotic freedom of QCD. In 1975 J. C. Collins and M. J. Perry suggested that the quarks can be the fundamental freedom in the superdense matter [17]. In the same year, N. Cabibbo and G. Parisi predicted the existence of a phase of the vacuum in which quarks are not confined at the high temperature or at the high density [18]. The confined and deconfined phases are called the hadronic phase and the quark-gluon plasma (QGP) phase, respectively. The lattice QCD simulations suggest that the phase transition between the hadronic and the QGP phases at zero baryon chemical potential is a cross over phase transition and the pseudo critical temperature is about 150MeV [19–22]. The QGP phase is believed to exist at early Universe, about 10^{-5} second after the cosmic Big Bang and the deconfinement-confinement cross over phase transition is believed to be happened in the evolution of the Universe [23].

1.1 Quantum ChromoDynamics

QCD describes the interaction between quarks and gluons, which is called the strong interaction, and is the SU(3) component of the SU(3) $\times$ SU(2) $\times$ U(1) Standard Model of particle physics. QCD Lagrangian density at zero chemical potential is given by

$$\mathcal{L}_{\rm QCD} = \mathcal{L}_{\rm gluon} + \mathcal{L}_{\rm quark}, \tag{1.1}$$

where the fermion part is

$$\mathcal{L}_{\rm quark} = \bar{\psi}(x)(i\gamma^\mu(\partial_\mu - gA_\mu(x)) - m)\psi(x), \tag{1.2}$$

and

$$A_\mu(x) = \sum_{a=1}^{8} A_\mu^a \frac{\lambda^a}{2}, \tag{1.3}$$

and $\psi(x)$ is the dirac spinor field with color degree of freedom

$$\psi = \begin{pmatrix} \psi^1 \\ \psi^2 \\ \psi^3 \end{pmatrix}, \tag{1.4}$$

Here, λ^a are the generator of SU(3), $a = 1,\ 2, \ldots,\ 8$, and γ-matrix satisfies

$$\{\gamma^\mu, \gamma^\nu\} = 2g^{\mu\nu}. \tag{1.5}$$

The number of the components of ψ in Eq. (1.4) is corresponds to three "colors" of quarks. Therefore, ψ lies in the fundamental representation of SU(3). Similarly, A_μ,

which corresponds to gluons, is the adjoint representation of SU(3).

$\mathcal{L}_{\text{quark}}$ is invariant under the local SU(3) transformation,

$$\psi'(x) = G(x)\psi(x), \tag{1.6}$$
$$\bar{\psi}'(x) = \bar{\psi}(x)G^{-1}(x), \tag{1.7}$$
$$A'_\mu(x) = G(x)A_\mu(x)G^{-1}(x) - \frac{i}{g}G(x)\partial_\mu G^{-1}(x). \tag{1.8}$$

where

$$G(x) = \exp\left(-i\theta^a(x)\frac{\lambda^a}{2}\right), \tag{1.9}$$

and $\theta^a(x)$ is a coordinate dependent real parameter. The gluonic part is given by

$$\mathcal{L}_{\text{gluon}} = \frac{1}{4}F^a_{\mu\nu}F^{a\mu\nu}, \tag{1.10}$$

where

$$F^a_{\mu\nu} = \partial_\mu A^a_\nu - \partial_\nu A^a_\mu - gf^{abc}A^b_\mu A^c_\nu, \tag{1.11}$$

and f^a_{bc} is a structure constant, defined as

$$\left[\lambda^a, \lambda^b\right] = 2if^{abc}\lambda_c. \tag{1.12}$$

The parameters of QCD are the coupling constant g and quark mass m.

When the quark mass m is zero, $\mathcal{L}_{\text{quark}}$ is invariant under the independent phase rotation of the left-handed and right-handed components of ψ, $\psi_L = (1-\gamma_5)\psi/2$ and $\psi_R = (1+\gamma_5)\psi/2$, respectively. Here $\gamma_5 \equiv i\gamma^0\gamma^1\gamma^2\gamma^3$. This symmetry is called the chiral symmetry. In the real world, since the quarks have non-zero quark mass, the chiral symmetry is broken. However, because u and d quark masses are MeV scale ,when we are interested in the high energy scale larger than this scale, the chiral symmetry can be regarded as approximately correct. For example, in the high temperature deconfined phase, the chiral symmetry for the light quark is approximately restored.

The interaction between the quarks and gluons is represented by the second term in Eq. (1.2), $g\bar{\psi}A_\mu\psi$. When the interaction term does not exist, $\mathcal{L}_{\text{quark}}$ is invariant under the global SU(3) transformation. The interaction term is naturally introduced supposing the "local" SU(3) invariance for $\mathcal{L}_{\text{quark}}$.

Owing to the third term in Eq. (1.11), $\mathcal{L}_{\text{gluon}}$ has the gluon self-interaction terms. This is a big difference with Quantum electrodynamics, which is the $U(1)$ Abelian gauge theory.

1.1.1 Running coupling constant

In perturbative QCD, the renormalized coupling constant $g(\mu_R)$ depends on the renormalization scale μ_R. Though μ_R itself is unphysical, when we are interested in a process with the momentum transfer Q, $g(\mu_R)$ with $\mu_R \sim Q$ represents the effective strength of the strong interaction in the process.

The running coupling constant for $SU(N)$ gauge theory satisfies the renormalization group equation

$$\mu_R\frac{\partial\bar{g}}{\partial\mu_R} = \beta(\bar{g}). \tag{1.13}$$

The sign of $\beta(g)$ determines whether the theory is asymptotic free or not. In the 1-loop analysis, $\beta(g)$ is calculated as

$$\beta(g) = -\frac{g^3}{(4\pi^2)}\left(\frac{11}{3}N - \frac{2}{3}n_f\right), \tag{1.14}$$

where n_f is the number of the flavors. The solution of Eq. (1.13) is obtained as

$$\bar{\alpha}(\mu_{\rm R}) = \frac{12\pi}{(11N - 2n_f)\ln\left(\mu_R^2/\Lambda^2\right)}, \tag{1.15}$$

with $\bar{\alpha}(\mu_{\rm R}) = \bar{g}(\mu_{\rm R})^2/4\pi$. We can easily see that if $n_f < 5.5N$, when $\mu_R \to \infty$, $\bar{\alpha} \to 0$. In the case of QCD, since $n_f = 6$ and $N = 3$, $\beta(g)$ is negative and QCD is asymptotic free. The QCD energy scale Λ is the free parameter. The numerical value of Λ depends on the gauge and the renormalization scheme and is determined by compared with an experiment.

1.2 Heavy Ion Collisions

The experimental study of QGP have been started after the theoretical predictions. In the late 20th century, the experiments with a high-energy heavy ion beam and a fixed target had been carried out at the Alternating Gradient Synchrotron (AGS) at BNL and the Super Proton Synchrotron (SPS) at CERN. These experiments provided interesting results. However, since the maximum center-of-mass collisional energies per nucleon pair for AGS and SPS were $\sqrt{s_{NN}} \simeq 5$ and 17 GeV, respectively, the clear evidence of the QGP formation could not be found [24]. It is believed that the first generating QGP in the laboratory was realized by the heavy ion collisions (HIC) at BNL's Relativistic Heavy Ion Collider (RHIC), whose operation started in 2000. The highest RHIC energy (the center-of-mass energy per nucleon pair) is 200 GeV, which is much higher than the AGS and SPS energies. In RHIC, the gold nuclei are accelerated in the two 3.8 km ring and collide. In 2010, HIC using Pb nuclei have started at the Large Hadron Collider (LHC) at CERN. The circumference of the ring is 27 km and the highest LHC energy is 2.76 TeV. In the HIC, the synchronized two heavy nuclei collide and the hot matter is generated at the collisional point. Even if the generated hot matter is in the deconfined phase, the temperature cools down quickly in the expansion process and the matter goes back to the confined phase. The schematic picture of the space-time evolution of

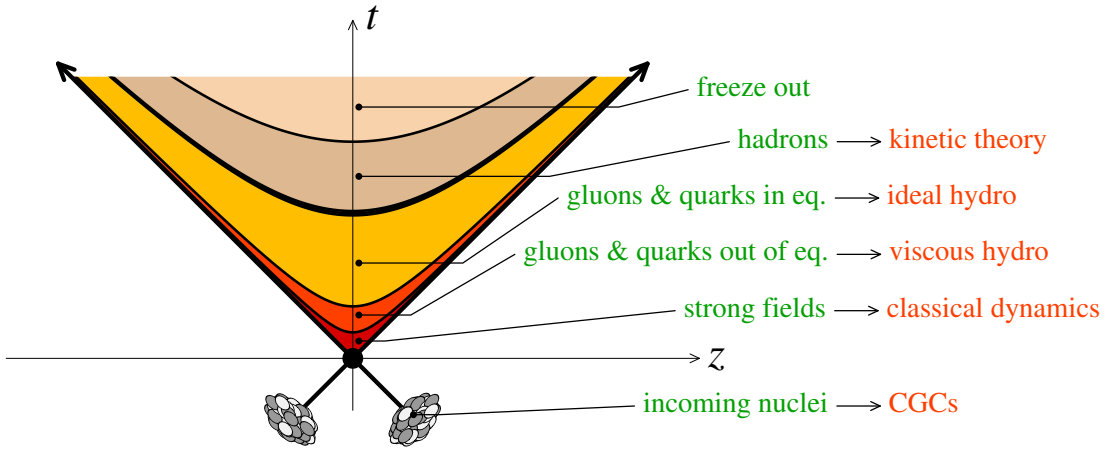

FIGURE 1.1: Light-cone diagram for time evolution of HIC as a function of time t and the collisional axis z. Contours indicate the constant proper time $\tau = \sqrt{t^2 - z^2}$. The picture is taken from Ref. [25].

TABLE 1.2: Mass, binding energy, and radius for charmonia and bottomonia from Non-relativistic potential theory [28]

state	J/ψ	χ_c(1P)	ψ(2S)	Υ(1S)	χ_b(1P)	Υ(2S)	χ_b(2P)	Υ(3S)
Mass [GeV]	3.10	3.53	3.68	9.46	9.99	10.02	10.26	10.36
Binding [GeV]	0.64	0.20	0.05	1.10	0.67	0.54	0.31	0.20
Radius [fm]	0.50	0.72	0.90	0.28	0.44	0.56	0.68	0.78

HIC is shown in Fig. 1.1. After the collisions of the nuclei, the gluons in the nuclei are interacting and the matter in the highly non-equilibrium state is generated. Next the system reaches the equilibrium state and QGP is formed. The experimental results suggest the time evolution of QGP can be interpreted by the viscous hydrodynamics with a small shear viscosity. As the system expands, the mean free time of the particle composing the plasma becomes larger than the time scale of the expansion and the system can no longer be treated as an equilibrium system. First, the chemical freeze out, after which the species of the particles does not change, takes place. Next the kinetic freeze out, after which the particles dose not interact with each other, occurs. Finally the non-interacting hadrons, photons and charged leptons are detected by the detectors.

Since the observables in HIC are not those in the deconfined phase, we have to find the indirect evidence of the QGP formation. The J/ψ suppression, proposed in 1986 [26, 27], is believed as one of the signals of the formation of QGP. T. Matsui and H. Satz suggested that if QGP is formed in HIC, $c\bar{c}$ binding in the deconfined medium is prevented owing to the color Debye screening, which is the analogy of the Debye screening of the electric charge in plasmas [27]. If the color Debye radius is smaller than the J/ψ radius, J/ψ is dissociated in the medium and the yield of J/ψ is suppressed. Table. 1.2 shows the masses, binding energies, and radiuses of the charmonia and bottomonia, which are the charmed and bottomed quarkonia, respectively. Since the radiuses of charmonia are larger than those of bottomonia as shown in the table, it is believed that the dissociation temperatures of the charmonia are lower than those of bottomonia. Owing to the idea of the J/ψ suppression, understanding properties of heavy quarkonia in hot medium near and above the critical temperature T_c of the deconfinement phase transition is one of the important subjects in the relativistic heavy ion collisions and has been studied actively over the last 30 years, both experimentally and theoretically [29, 30].

The experimental detection of the J/ψ suppression is more complicated than the theoretical idea. First we consider the case of HIC at RHIC. Below the top RHIC energy $\sqrt{s_{NN}} = 200$ GeV, the thermal production of $c\bar{c}$ pair is suppressed because the J/ψ mass $m_{J/\psi}$ is much larger than the temperature of the generated medium. Therefore, $c\bar{c}$ pairs are mainly produced by the hard process. However, even if the charmonium produced in the hard process survives in QGP, the charmonium may be destroyed by the final state interaction with surrounding hadronic matters, the so-called nuclear absorption. Furthermore, the presence of nuclei in the initial state will affect the J/ψ production, which is known as the Cold Nuclear Matter (CNM) effects [30]. To study the medium effects for J/ψ yield, therefore, one has to make use of the results of the pp and pA collisions [31]. To clarify the medium effects on quarkonia, a nuclear modification factor is used [23]. The nuclear modification factor is defined by the ratio of the p_T distribution from AA collisions $\sigma_{AA}(p_T)$ and the p_T distribution from pp collisions $\sigma_{NN}(p_T)$ at the same energy, scaled by the number of primary nucleon-nucleon collisions $\langle N_{\rm binary}\rangle$ (estimated by the Glauber model [32]),

$$R_{AA}(p_T) = \frac{\sigma_{AA}(p_T)}{\langle N_{\rm binary}\rangle \sigma_{NN}(p_T)}. \tag{1.16}$$

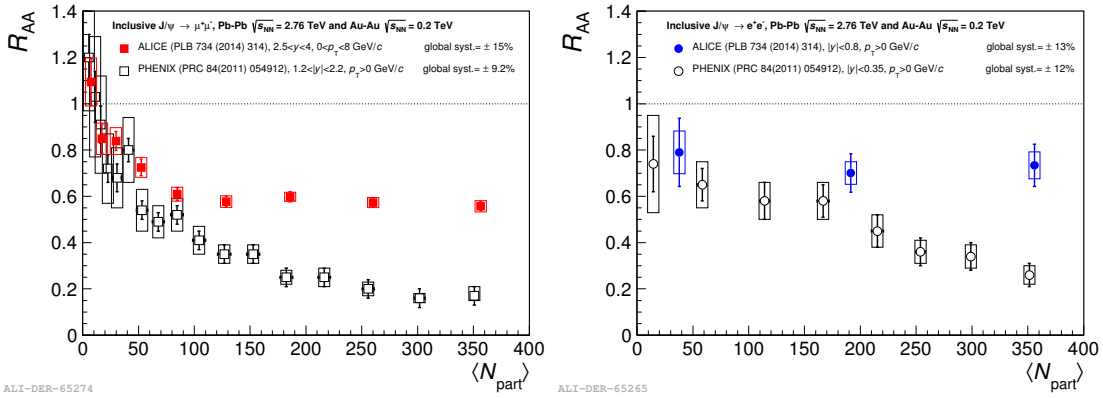

FIGURE 1.2: Inclusive J/ψ nuclear modification factor versus the number of participant nucleons at ALICE [33, 34] and PHENIX [35] , at forward rapidity (left) and mid rapidity (right). The figures are taken from Ref. [30].

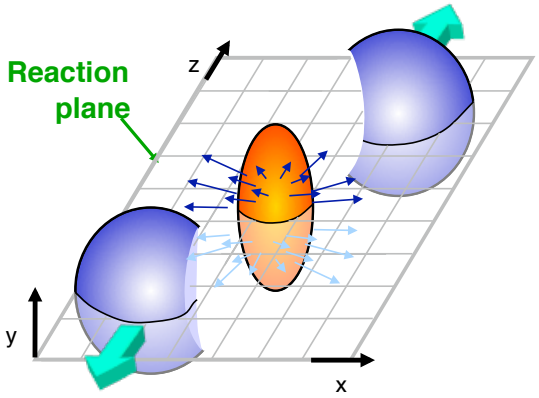

FIGURE 1.3: Geometry of the non-central HIC. The z-axis is the longitudinal axis. The x-axis and y-axis are the transverse coordinate and the x-axis is determined as the short axis of the almond shape overlapped region of nuclei. The picture is taken from Ref. [37].

If there is no medium effect for the AA collisions, $R_{AA}(p_T)$ becomes unity.

At the LHC energy, the highest energy is $\sqrt{s_{NN}} = 2.76$ TeV, the situation is quite different. Since the temperature of the medium is not much smaller than the charmonium mass, the thermal production of $c\bar{c}$ pair is not negligible. Because of the increase of the charm (and anti-charm) quarks in the medium, the recombination of the thermal charm quarks at the deconfinement-confinement transition must be considered. The ALICE and PHENIX R_{AA} of J/ψ at forward and mid rapidities are shown in Fig. 1.2. We see that the RHIC R_{AA} is significantly suppressed and the suppression is increased towards more central collisions. On the other hand, the LHC R_{AA} shows a flat behavior at forward and mid rapidities as a function of the centrality. This flat behavior can be explained by that the abundance of the charm quarks in the medium compensates the suppression from the color Debye screening.

One of the big discoveries at RHIC is that the relativistic hydrodynamic equation, such as the Israel-Stewart equation [36], can describe the time evolution of the hot matter created in HIC. This is believed to be the one of the evidences of the formation of QGP in HIC. In HIC the overlapped region of the collided nuclei pair is different for each event. Figure 1.3 shows the sketch of the geometry of the non-central, not a head-on, collision. Since the overlapped region of the non-central HIC has a almond shape, the almond shaped hot matter is created at the collisional point. When the almond shaped matter reaches equilibrium, the pressure in the surface of the matter should be zero.

Since the distance of the center from the surface is different for the long-axis and short-axis directions, the pressure gradient along the short-axis is larger than that along the long-axis. As a consequence of the large pressure gradient, the number of particles with a large transverse momentum p_T emitted along the short-axis becomes larger than that along long-axis. This anisotropic distribution of particle emission is called the elliptic flow. In the experiment, the elliptic flow is analyzed as the second harmonics of the Fourier expansion of the azimuthal distribution of particle emission given by

$$E\frac{d^2N}{2\pi p_T dp_T dy} = \left(1 + \sum_{n=1}^{\infty} 2v_n \cos[n(\phi - \Phi_r)]\right), \tag{1.17}$$

where ϕ is the azimuthal angle and Φ_r is the angle of the reaction plane. The second Fourier coefficient v_2 indicates the strength of the elliptic flow. If the charm quark behaves as a constituent of the fluid, nonzero v_2 for charmed particles will be observed. The left panel in Fig. 1.4 shows the v_2 of heavy-flavor electrons and π^0 at the same p_T

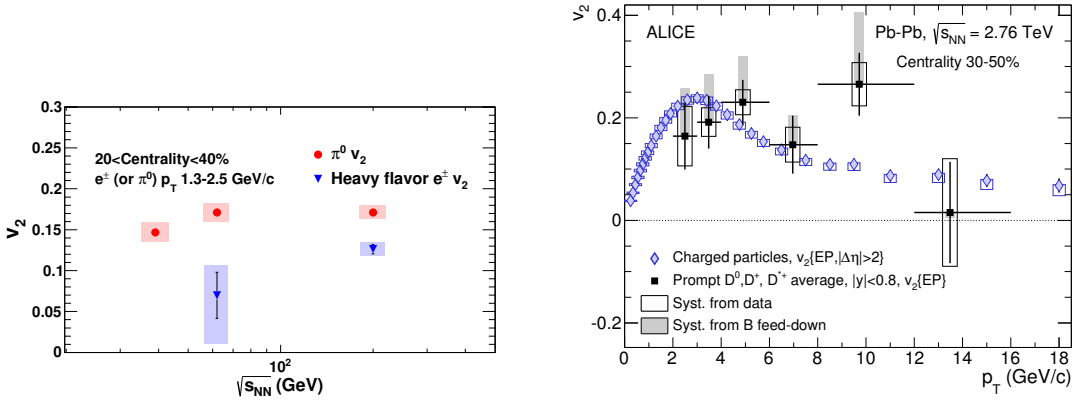

FIGURE 1.4: *left:* v_2 of heavy-flavor electrons and π^0 measured at $\sqrt{s_{NN}} = 62.4$ and 200 GeV in Au+Au collisions in the $20-40\%$ centrality for the interval $1.3 < p_T < 2.5$ GeV at PHENIX [38]. The figure is taken from Ref. [30]. *right:* Average of D^0, D^+, and D^{*+} mesons v_2 as a function of p_T in the $30-50\%$ centrality, compared with the v_2 of charged particles at ALICE [33].

interval at semi-peripheral collisions with $\sqrt{s_{NN}} = 62.4$ and 200 GeV measured by the PHENIX Collaboration. The figure suggests that v_2 of the heavy flavor and the neutral pion, which is one of the main components of the medium, become closer as $\sqrt{s_{NN}}$ is increased. The right panel in Fig. 1.4 shows the v_2 of D-meson and the charged particles measure by the ALICE Collaboration. We can see that the v_2 of D-meson is comparable with that of the charged particles in the p_T interval $2 < p_T < 6$ GeV. Therefore, the properties of the charm in the hydrodynamic medium, such as the transport coefficients of the charm quarks, are important to understand the experimental results.

1.3 Lattice study of the deconfined medium

The lattice QCD numerical simulation is a powerful tool to study the physics where the non-perturbative effect of QCD plays a crucial role. The study of the properties of charmonia at the finite temperature is one of the longstanding subjects on the lattice [39–47]. In lattice QCD numerical simulations, which rely on the imaginary time formalism, however, one cannot analyze dynamical properties encoded in spectral functions directly. Instead, only Euclidean correlation functions are calculable on the lattice. To obtain the spectral functions from the Euclidean correlators, one has to take an analytic

continuation from imaginary time to real time. This procedure, however, is an ill-posed problem, because the information obtained numerically on the correlator for discrete points is insufficient to reconstruct a continuous spectral function. The maximum entropy method (MEM) is a useful method to perform this analytic continuation on the basis of probabilistic theory [48, 49]. The studies of charmonium spectral functions with MEM qualitatively agree with each other in that the charmonia in the vector and pseudoscalar channels survive up to around $T \simeq 1.5T_c$ [39, 40, 42, 47].

In the previous studies on heavy quarkonia on the lattice, the analyses have been performed only for zero momentum with a few exceptions [50–54]. The spectral function with zero momentum represents the spectral properties of a charmonium at rest in medium. On the other hand, charmonia in the hot medium created by heavy ion collisions typically have nonnegligible velocity against the rest frame of the medium because charmonia generated by hard processes in the early stage can have large momentum. The finiteness of the velocity of charmonia may modify their properties, such as the stability [55] and the dispersion relation, i.e. the momentum dependence of excitation energy. Here it is worthwhile to note that such modifications of the dispersion relations in medium are suggested in various systems [56–58], and such a modification can give rise to novel phenomena such as van Hove singularity [59–62]. It thus is interesting to explore the momentum dependence of spectral functions of charmonia and their dispersion relations near and above T_c with the first principle simulation on the lattice.

An another interesting topic of the lattice simulation at the finite temperature is the determination of transport coefficients in the hot medium described by QCD near and above the (pseudo) critical temperature T_c of deconfinement transition. In fact, this subject has acquired attentions over the last few decades [63–70]. This subject is to a large extent motivated by experimental results in relativistic heavy-ion collisions [71, 72]. The elliptic flow observed at RHIC (Relativistic Heavy Ion Collider) and the LHC (Large Hadron Collider) suggests the shear viscosity to entropy density ratio close to a conjectured lower bound $\eta/s = 1/(4\pi)$ [66] near but above T_c. Understanding the origin of the small shear viscosity based on QCD is an important subject for theoretical researches in this field. As we saw in Sec. 1.2, diffusion coefficient of heavy quarks also attracts much interests inspired by the elliptic flow of heavy flavor in heavy-ion collisions [30, 73, 74], which suggests a relatively small value for charm quarks [75–77]. Once quantitative constraints on these transport coefficients are obtained, they also serve as valuable inputs for phenomenological studies on these experiments.

The measurement of transport coefficients on the lattice has been attempted by many studies, such as on shear and bulk viscosities [63, 64, 66–69, 78], electrical conductivity [79–84] and heavy-quark diffusion coefficients [85–89]. The transport coefficients can be read from the low energy region of the relevant spectral functions. Therefore, the main difficulty of the measurement of transport coefficients on the lattice arises from the extraction of the information of the spectral function in the low energy region from the Euclidean correlator. In almost all previous studies, the transport coefficients are analyzed with the use of the Kubo formulas in forms which relate a coefficient with a spectral function in the low-energy limit at zero momentum [90, 91]. In this approach, the entire form of the spectral function has to be reconstructed by the analytic continuation from the numerical results on the Euclidean correlators. The reconstruction of the spectral function from the lattice Euclidean correlator is a difficult problem owing to the ill-posed problem. Even worse, the Euclidean correlators are insensitive to the change of the low-energy structure of spectral functions [92], although this structure is crucial for the analysis of transport coefficients. Figure 1.5 shows the heavy quark diffusion coefficients in the gluon plasma obtained by the lattice QCD with MEM [87], the Heavy Quark Effective Theory (HQEFT) on the lattice [88, 93], the AdS/CFT correspondence [94], and pQCD calculations [95]. The orders of these results are consistent. However,

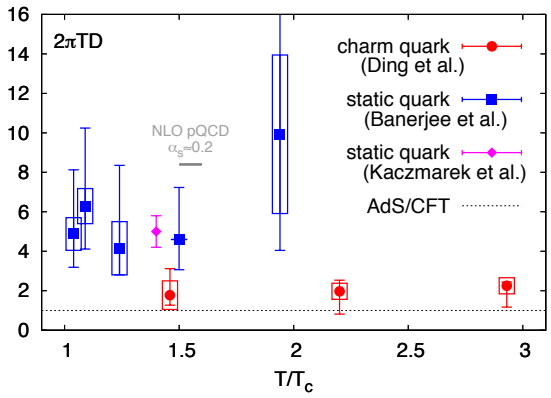

FIGURE 1.5: Temperature in units of T_c v.s. Heavy quark diffusion coefficients multiplied by 2π in quenched lattice. The charm quark diffusion coefficient is obtained by reconstructing the spectral function with MEM [87]. The results for static quark diffusion coefficient are calculated by HQEFT on the lattice [88, 93], whose diffusion coefficients are obtained by fitting the correlators with theoretical motivated anzats. The boxes and the error bars show the statistical error and the systematic error, respectively. The horizontal dotted line shows the $2\pi DT$ in the heavy quark limit calculated by the AdS/CFT correspondence [94]. The horizontal short line shows the result obtained by the nest-to-leading order pQCD calculations at $\alpha_s \simeq 0.2$ [95]. The figure is taken from Ref. [96].

the their errors are still large. Moreover, the error estimation for the charm quark diffusion coefficient, obtained by using MEM, is not on the basis of MEM, which we will discuss in Chap. 4. Since the resolution of MEM is too coarse to read the slope of the spectral function at the origin, MEM is not a suitable method. If one estimates the error on the basis of MEM, the error will be much larger than that shown in the figure. The heavy quark diffusion coefficients with HQEFT are calculated in the heavy quark limit. HQEFT is a good effective theory for studying the physics of the bottom quarks. However, when these results are applied to charm quark diffusion coefficient, the systematic uncertainties become large since the charm quark mass is not much larger than the temperature of the medium [89]. The method to measure the transport coefficients on the lattice with good accuracy is still not well established.

1.4 Purpose of this thesis

In this thesis, we study two topics related with the charmonium spectral function at nonzero momentum using the numerical simulation of the quenched lattice QCD.

First, we explore the properties of charmonia in the vector and pseudoscalar channels, corresponding to J/ψ and η_c, respectively, at nonzero momenta on anisotropic quenched lattices [97]. In addition to the standard analysis of the spectral functions in MEM, we study the dispersion relations and the momentum dependence of the spectral weights of the peaks on the basis of MEM. To perform the measurement of the dispersion relation with a quantitative error analysis in MEM, we analyze the center of weight of the peak in the spectral function. As we will see later, this quantity is identical to the peak position for sufficiently narrow peaks, but error analysis can be carried out in MEM. Similarly, we analyze the weight of the peak, which corresponds to the residue of the peak, with the error analysis. For the vector channel, the transverse and longitudinal components are investigated separately in the analysis.

We find that the masses of J/ψ and η_c defined by the dispersion relation at zero momentum show significant increase as T is raised. It is also found that the dispersion relation of charmonia continues to take the Lorentz covariant form, i.e. the same form

as in the vacuum, even well above T_c within the error. Our numerical analysis also suggests that the weight of the peak at the finite temperature does not have momentum dependence within the error.

Second, we analyze the charm quark diffusion coefficients by lattice simulations with a novel approach. The characteristics of this study is the use of the current-current correlator in temporal channel at nonzero momentum. This is contrasted to the previous studies with the Kubo formulas which analyze the spatial correlators at zero momentum. At zero momentum, owing to the charge conservation the temporal Euclidean correlator temporal is given by a constant proportional to susceptibility. The correlator at nonzero momentum, on the other hand, is dependent on imaginary time and contain the information on dynamics. As we will see later, the temporal channel at nonzero momentum is more sensitive to the low-energy part of dynamical properties than the spatial one. The purpose of the present study is to exploit this sensitivity in the analysis of the transport coefficients.

In order to see the effectiveness of the use of the nonzero momentum correlator in temporal channel, instead of the standard approach with the Kubo formula and spectral function, we attempt to constrain the transport coefficient by imposing moderate assumptions on the spectral function. We obtain two inequalities constraining the diffusion coefficient and the corresponding relaxation time from the momentum derivatives of Euclidean correlators in temporal channel. Numerical analysis of the correlator are performed for the charm quark current on the quenched lattice for $1.7 < T/T_c < 4.7$. We demonstrate that the transport coefficients are nicely constrained numerically in this method.

The results obtained in the present analysis suggest that the nonzero momentum correlators are indeed quite useful for the analysis of transport coefficients on the lattice. Based on this result, we discuss further improvement of the analysis of transport coefficients using nonzero momentum correlators. Although we restrict our attention to the diffusion of charm quarks throughout this thesis, our analysis can be applied to another transport coefficients, such as shear and bulk viscosities, in a straightforward manner.

This thesis is organized in two parts comprising Chaps. 1 through 5 and 6 through 9. Roughly speaking the first gives the reviews of background and the theoretical groundwork of our work while the second gives our original work.

In Chap. 2, we review the lattice field theory, which is one of the main tools of our work. We show the definition of QCD on the lattice especially focusing on the Wilson gauge and Wilson fermion actions. We also show how the lattice action is modified on the anisotropic lattice.

In Chap. 3, we summarize the relations between real time correlators and a Euclidean correlator. The basic properties of the spectral function is also discussed.

Chapter 4 is the review of Maximum Entropy Method. We show the basics of MEM and the definition of the MEM error. The numerical procedure of the MEM analysis is also shown.

In Chap. 5, we present the relation between the hydrodynamics and the spectral function. We start from the diffusion equation with the relaxation time and derive the low energy structure of the spectral function using the linear response theory. We also show the derivation of the Kubo formula.

In Chap. 6, we discuss the main target observables in this thesis and how they are measured on the lattice. We show definitions of the dispersion relation and the strength of the peak of the spectral function of quarkonium with MEM. We derive an inequality for the diffusion coefficient differentiating the Euclidean correlator in temporal channel with respect to momentum. We discuss the measurement of this inequality on the lattice and an advantage. The common lattice set up of these studies are shown.

The numerical results of the dispersion relations and the momentum dependence of the strength of the peak of the spectral function of charmonium in the pseudoscalar and vector channels with MEM are shown in Chap. 7. We analyze the peaks of the spectral functions with zero and nonzero momenta corresponding to J/ψ and η_c at the zero temperature and finite temperature.

The numerical results of the inequality for the charm quark diffusion coefficient is shown in Chap. 8. We analyze the temporal Euclidean correlators. The derivatives of the correlators with respect to momentum at origin are analyzed by taking the zero momentum extraction of the numerical difference of the correlators.

Finally Chap. 9 gives the summary of shown results and an outlook.

Chapter 2

Lattice Field Theory

Yang-Mills theory, which was proposed in 1950s [1], is one of the bases of modern physics. Quantum ChromoDynamics (QCD), which describes the strong interaction, is SU(3) Yang-Mills theory. Since QCD is a strongly coupled theory as shown in Sec. 1.1, the perturbative analysis cannot be applicable to the studies of QCD matter around the critical temperature (T_c). Lattice field theory is one of the regularization methods for a quantum field theory. Lattice regularization was first proposed by K. G. Wilson in 1974 [98]. Wilson discussed about the quark confinement in a gauge theory using the lattice regularization and the strong-coupling expansion in Ref. [98]. Because space-time is discretized in the lattice field theory, this formalism is suitable to a numerical simulation on a computer. First lattice numerical simulation of non-Arberian gauge theory was performed by M. Creutz [99, 100]. Today the lattice simulation have become an active of elementary particle physics and nuclear physics.

In this chapter we review the lattice field theory on the basis of the textbooks [101–103]. We first define the quantum field theory on the lattice in Sec. 2.1. Next we show you the QCD action on the lattice in Sec. 2.2. Next, we discuss the meson correlators, which are the main target of the present thesis. In Sec. 2.4, we review the anisotropic lattice simulations, which is useful method for studies of momentum dependence of lattice observables. Finally we review some numerical techniques of the lattice QCD in Sec. 2.5.

2.1 Quantum field theory on the lattice

Lattice field theory is one of the methods to define a quantum field theory (QFT). In the lattice field theory, one define the theory on the lattice with a finite lattice spacing and volume. After calculating observables on the lattice, one takes the continuum and infinite volume limits. Because of a finite lattice spacing and a finite volume, the ultraviolet and the infrared divergences are removed naturally.

2.1.1 Scalar field on the lattice

Let us see how a scaler field is defined on the lattice. The action of a scalar field $\phi(x)$ in the continuum theory is

$$S = -\frac{1}{2}\int d^4x\phi(x)(\Box + M^2)\phi(x), \tag{2.1}$$

where $\Box$ is the d'Alembert operator. The classical equation of motion is the Klein-Gordon equation,

$$(\Box + M^2)\phi(x) = 0. \tag{2.2}$$

In the quantum field theory, $\phi(x)$ is replaced by an operator $\Phi(x)$. The correlation function in the path integral representation is obtained as

$$\langle\Omega|T(\Phi(x)\Phi(y)\cdots|\Omega\rangle = \frac{\int \mathcal{D}\phi\phi(x)\phi(y)\cdots e^{iS}}{\int \mathcal{D}\phi e^{iS}}, \tag{2.3}$$

where $|\Omega\rangle$ denotes a vacuum state and $T(\cdots)$ means the time-ordered product. Discussing in the Euclidean space is convenient because we can treat time and space with same ways. Let us consider an analytic continuation from a real time to an imaginary time, $x^0 \to -ix^4$. The Euclidean action, which corresponds to Eq. (2.1), is given by

$$S_E = \frac{1}{2}\int d^4x\phi(x)(-\Box + M^2)\phi(x), \tag{2.4}$$

where $x = (\boldsymbol{x}, x^4)$ is the 4-vector in the Euclidean space, and $\Box$ denotes 4-dimensional Laplacian

$$\Box = \sum_{\mu=1}^{4}\partial_\mu\partial_\mu. \tag{2.5}$$

The Euclidean correlation function, which corresponds to Eq. (2.3), is

$$\langle\phi(x)\phi(y)\cdots\rangle = \frac{\int \mathcal{D}\phi\phi(x)\phi(y)\cdots e^{-S_E}}{\int \mathcal{D}\phi e^{-S_E}}, \tag{2.6}$$

The path integral formulation in Eq. (2.6) is just a schematic formulation. The most famous method to calculate the path integral is a perturbative expansion. However, the perturbation theory cannot be applied to a strongly coupled theory. To calculate the right hand side of Eq. (2.6) without the use of perturbation, we introduce a space-time lattice with a lattice spacing a. The space-time is denoted by four integers $n = (n_1, n_2, n_3, n_4)$. On the lattice, the quantities in the continuum space are discretized as

$$\begin{aligned} x_\mu &\to n_\mu a, \\ \phi(x) &\to \phi(na), \\ \int d^4x &\to a^4\sum_n, \\ \Box\phi(x) &\to \frac{1}{a^2}\hat{\Box}\phi(na), \\ D\phi &\to \prod_n d\phi(na), \end{aligned} \tag{2.7}$$

where the dimensionless lattice Laplacian $\hat{\Box}$ is defined as

$$\hat{\Box}\phi(na) = \sum_\mu(\phi(na+\hat{\mu}a) + \phi(na-\hat{\mu}a) - 2\phi(na)), \tag{2.8}$$

where $\hat{\mu}$ is a unit vector pointing the direction μ.

For the convenience of notation, we introduce

$$\hat{\phi}_n = a\phi(na), \tag{2.9}$$

$$\hat{M} = aM. \tag{2.10}$$

Substituting Eqs. (2.7) and (2.10) into Eq. (2.6), we find

$$\langle \hat{\phi}_n \hat{\phi}_m \cdots \rangle = \frac{\prod_l d\hat{\phi}_l \hat{\phi}_n \hat{\phi}_m \cdots e^{-S_E[\hat{\phi}]}}{\prod_l d\hat{\phi}_l e^{-S_E[\hat{\phi}]}}, \tag{2.11}$$

where l runs over all lattice points and

$$S_E[\hat{\phi}] = -\frac{1}{2}\sum_{n,\hat{\mu}} \hat{\phi}_n \hat{\phi}_{n+\hat{\mu}} + \frac{1}{2}(8+\hat{M}^2)\sum_n \hat{\phi}_n \hat{\phi}_n, \tag{2.12}$$

and where $\hat{\mu}$ is summed over all positive and negative directions. In Eq. (2.11) the lattice spacing a does not appear. Thus, after we calculate the Euclidean correlator on the lattice with dimensionless quantities, we have to restore the physical dimension using Eq. (2.7).

Let us see the characteristics of the lattice correlation function in Eq. (2.11). The lattice Euclidean action Eq. (2.12) can be rewritten as

$$S_E = \frac{1}{2}\sum_{n,m} \hat{\phi}_n K_{nm} \hat{\phi}_m, \tag{2.13}$$

$$K_{nm} = -\sum_{\hat{\mu}>0} [\delta_{n+\hat{\mu},m} + \delta_{n-\hat{\mu},m} - 2\delta_{nm}] + \hat{M}^2 \delta_{nm}, \tag{2.14}$$

where the summation in Eq. (2.14) is understood as the summation over all positive directions of $\hat{\mu}$.

The generating functional

$$Z_0[J] = \int \prod_l d\hat{\phi}_l e^{-S_E[\hat{\phi}] + \sum_n J_n \hat{\phi}_n}, \tag{2.15}$$

where J_n is a source field, is a convenient tool to study the correlation function. We can perform the path integral in Eq. (2.15) using the Gauss integral.

$$\begin{aligned} Z_0[J] &= \int \prod_l d\hat{\phi}_l \exp\left(-\frac{1}{2}\sum_{nm} (\hat{\phi}_n - \sum_a J_a K^{-1}_{an}) K_{nm} (\hat{\phi}_m - \sum_b J_b K^{-1}_{mb}) + \frac{1}{2} J_n K^{-1} J_m \right) \\ &= \frac{1}{\sqrt{\det K}} e^{\frac{1}{2} J_n K^{-1} J_m}, \end{aligned} \tag{2.16}$$

where K^{-1} is the inverse of K in Eq. (2.14). We can easily obtain the two-point function by taking the functional differentiation of Eq. (2.16) as,

$$\langle \hat{\phi}_n \hat{\phi}_m \rangle = \frac{\delta^2}{\delta J_n \delta J_m} Z_0[J] = K^{-1}_{nm}. \tag{2.17}$$

The Fourier transformation of the Kronecker delta δ_{nm} is given by

$$\delta_{nm} = \int_{-\pi}^{\pi} \frac{d^4\hat{k}}{(2\pi)^4} e^{i\hat{k}\cdot(n-m)}, \tag{2.18}$$

where $\hat{k} = (\hat{k}_1, \hat{k}_2, \hat{k}_3, \hat{k}_4)$ is the dimensionless 4-vector, which are restricted in Brillouin zone (BZ) $-\pi < \hat{k}_\mu < \pi$. Using Eq. (2.18), we obtain the Fourier transformation of K

in Eq. (2.14),

$$\begin{aligned} K_{nm} &= \int_{-\pi}^{\pi} \frac{d^4\hat{k}}{(2\pi)^4} \left\{ -\sum_{\hat{\mu}>0} \left[(e^{i\hat{k}_\mu} + e^{-i\hat{k}_\mu}) - 2 \right] e^{i\hat{k}(n-m)} + \hat{M}^2 e^{i\hat{k}(n-m)} \right\} \\ &= \int_{-\pi}^{\pi} \frac{d^4\hat{k}}{(2\pi)^4} \left\{ \sum_{\mu=1}^{4} \left[(2 - \cos\left(\hat{k}_\mu\right) \right] e^{i\hat{k}(n-m)} + \hat{M}^2 e^{i\hat{k}(n-m)} \right\} \\ &= \int_{-\pi}^{\pi} \frac{d^4\hat{k}}{(2\pi)^4} \tilde{K}(\hat{k}) e^{i\hat{k}(n-m)}, \end{aligned} \tag{2.19}$$

where

$$\tilde{K}(\hat{k}) = 4 \sum_{\mu=1}^{4} \sin^2 \left(\frac{\hat{k}_\mu}{2} \right) + \hat{M}^2. \tag{2.20}$$

Since

$$K_{nl} K^{-1}_{lm} = \delta_{nm}, \tag{2.21}$$

the two-point function Eq. (2.17) is given by

$$\langle \hat{\phi}_n \hat{\phi}_m \rangle = \int_{-\pi}^{\pi} \frac{d^4\hat{k}}{(2\pi)^4} \frac{e^{i\hat{k}(n-m)}}{4\sum_{\mu=1}^{4} \sin^2 \left(\frac{\hat{k}_\mu}{2} \right) + \hat{M}^2}. \tag{2.22}$$

We note that only dimensionless quantities are appeared on the right-hand side of Eq. (2.22).

Next, we consider taking the continuum limit $a \to 0$ of the correlator. When we define

$$G(n, m; \hat{M}) \equiv \langle \hat{\phi}_n \hat{\phi}_m \rangle, \tag{2.23}$$

the corresponding two-point function in the continuum limit is given by

$$\langle \phi(x)\phi(y) \rangle = \lim_{a \to 0} \frac{1}{a^2} G\left(\frac{x}{a}, \frac{y}{a}; Ma \right). \tag{2.24}$$

Changing the integration variable Eq. (2.22) we obtain

$$G\left(\frac{x}{a}, \frac{y}{a}; Ma \right) = a^2 \int_{-\pi/a}^{\pi/a} \frac{d^4k}{(2\pi)^4} \frac{e^{ik(n-m)}}{4\sum_{\mu=1}^{4} \tilde{k}_\mu^2 + M^2}, \tag{2.25}$$

where

$$\tilde{k}_\mu = \frac{2}{a} \sin \frac{k_\mu a}{2}. \tag{2.26}$$

From Fig. 2.1, we see that $\tilde{k}_\mu \to k_\mu$ in the continuum limit $a \to 0$ since the integration in Eq. (2.25) is restricted in BZ $-\pi < \hat{k}_\mu < \pi$. As we will show in the next subsection, this limit for Fermion is more complicated.

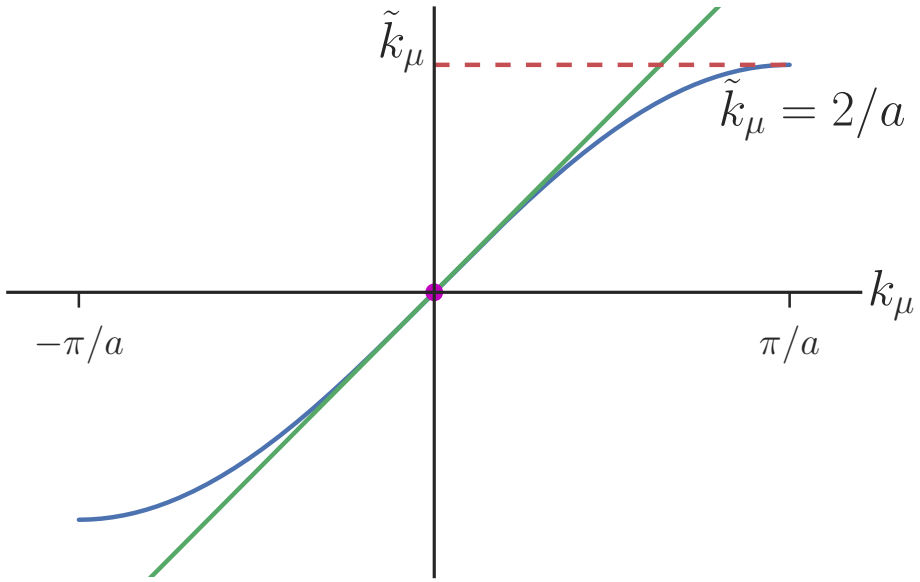

FIGURE 2.1: $2/a \sin(k_\mu a/2)$ versus k_μ

2.1.2 Fermion field on the lattice

The action of the free Dirac field in the Minkowski space is given by

$$S_F\left[\psi, \bar{\psi}\right] = \int d^4x \bar{\psi}(x)(i\gamma^\mu \partial_\mu - M)\psi(x). \tag{2.27}$$

In quantum field theory, ψ and ψ' are replaced with operators Ψ and Ψ', respectively. The correlation function in the path integral representation is obtained as

$$\langle \Omega | T(\Psi_\alpha(x) \cdots \bar{\Psi}_\beta(y) \cdots) | \Omega \rangle = \frac{\int \mathcal{D}\bar{\psi}\mathcal{D}\psi \psi_\alpha(x) \cdots \bar{\psi}_\beta \cdots e^{iS_F}}{\int \mathcal{D}\bar{\psi}\mathcal{D}\psi e^{iS_F}}. \tag{2.28}$$

As before, let us consider an analytic continuation from a real time to an imaginary time. Then, $iS_F[\psi, \bar{\psi}]$ is replaced with the Euclidean action

$$S_F^{(\mathrm{eucl.})} = \int d^4x \bar{\psi}(x)(\gamma_\mu^E \partial_\mu + M)\psi(x), \tag{2.29}$$

where the γ matrix in the Euclidean space is given by γ_μ^E with $\gamma_4^E = \gamma^0$ and $\gamma_i^E = -i\gamma^i$, which satisfies

$$\{\gamma_\mu^E, \gamma_\nu^E\} = 2\delta_{\mu\nu}. \tag{2.30}$$

Note that the Lorentz invariance is replaced with the rotational invariance in the 4-dimensional space. The Euclidean correlation function is given by

$$\langle \psi_\alpha(x) \cdots \bar{\psi}_\beta(y) \cdots \rangle = \frac{\int \mathcal{D}\bar{\psi}\mathcal{D}\psi \psi_\alpha(x) \cdots \bar{\psi}_\beta \cdots e^{-S_F^{(\mathrm{eucl.})}}}{\int \mathcal{D}\bar{\psi}\mathcal{D}\psi e^{-S_F^{(\mathrm{eucl.})}}}, \tag{2.31}$$

where x and y denote 4-vector in the Euclidean space. In the following, we omit the upper script of γ_μ^E which denotes Euclidean space.

Next, we define the Euclidean correlation function Eq. (2.31) on the lattice. When

the fermion fields ψ and $\bar{\psi}$ are on na, where a is a lattice spacing and n denotes the coordinate on the 4-dimension lattice, the integral measure is obtained as

$$\mathcal{D}\bar{\psi}\mathcal{D}\psi = \prod_{\alpha,n} d\bar{\psi}_\alpha(na) \prod_{\beta,m} d\psi_\beta(ma). \tag{2.32}$$

Dimensionless variables corresponding to ψ, $\bar{\psi}$, and M are also defined as

$$M \to \frac{1}{a}\hat{M}, \tag{2.33}$$

$$\begin{aligned} \psi_\alpha(x) &\to \frac{1}{a^{3/2}}\hat{\psi}_\alpha(n), \\ \bar{\psi}_\alpha(x) &\to \frac{1}{a^{3/2}}\bar{\hat{\psi}}_\alpha(n), \\ \partial_\mu\psi_\alpha(x) &\to \frac{1}{a^{5/2}}\hat{\partial}_\mu\hat{\psi}_\alpha(n), \end{aligned} \tag{2.34}$$

where the derivative $\hat{\partial}_\mu\hat{\psi}_\alpha(n)$ is defined as

$$\hat{\partial}_\mu\hat{\psi}_\alpha(n) = \frac{1}{2}[\hat{\psi}_\alpha(n+\hat{\mu}) - \hat{\psi}_\alpha(n-\hat{\mu})]. \tag{2.35}$$

With this discretization, the Fermion action Eq. (2.29) is written as

$$S_F = \sum_{n,m,\alpha,\beta} \bar{\hat{\psi}}_\alpha(n) K_{\alpha\beta}(n,m) \hat{\psi}_\beta(m) \tag{2.36}$$

$$K_{\alpha\beta}(n,m) = \sum_\mu \frac{1}{2}(\gamma_\mu)_{\alpha\beta}[\delta_{m,n+\hat{\mu}} - \delta_{m,n-\hat{\mu}}] + \hat{M}\delta_{mn}\delta_{\alpha\beta}, \tag{2.37}$$

and the correlation function on the lattice is written as

$$\langle \hat{\psi}_\alpha(n)\cdots\bar{\hat{\psi}}_\beta(m)\cdots\rangle = \frac{\int \mathcal{D}\bar{\hat{\psi}}\mathcal{D}\hat{\psi}\hat{\psi}_\alpha(x)\cdots\bar{\hat{\psi}}_\beta\cdots e^{-S_F^{(\text{eucl.})}}}{\int \mathcal{D}\bar{\hat{\psi}}\mathcal{D}\hat{\psi} e^{-S_F^{(\text{eucl.})}}}, \tag{2.38}$$

$$\mathcal{D}\bar{\hat{\psi}}\mathcal{D}\hat{\psi} = \prod_{n,\alpha} d\bar{\hat{\psi}}_\alpha(n) \prod_{m,\beta} d\bar{\hat{\psi}}_\beta(m). \tag{2.39}$$

We note that the correlation function Eq. (2.38) can be obtained by taking an appropriate functional derivatives of the generating functional,

$$Z[\eta,\bar{\eta}] = \int \mathcal{D}\bar{\hat{\psi}}\mathcal{D}\hat{\psi} e^{-S_F + \sum_{n,\alpha}\bar{\eta}_\alpha(n)\hat{\psi}_\alpha(n) + \bar{\hat{\psi}}_\alpha(n)\eta_\alpha(n)}, \tag{2.40}$$

with respect to η_α and $\bar{\eta}_\alpha$, where η_α and $\bar{\eta}_\alpha$ are Grassmann variable external fields. Taking the Grassmann integral in Eq. (2.40), one obtains

$$Z[\eta,\bar{\eta}] = \det K e^{\sum_{n,m,\alpha,\beta}\bar{\eta}_\alpha(n)K^{-1}_{\alpha\beta}(n,m)\eta_\beta(m)}. \tag{2.41}$$

The Doubling Problem

From Eq. (2.41) the two point correlation function on the lattice is given by

$$\langle \hat{\psi}_\alpha(n)\bar{\hat{\psi}}_\beta(m)\rangle = \frac{\delta^2}{\delta\eta\delta\bar{\eta}} Z[\eta,\bar{\eta}] = K^{-1}_{\alpha\beta}. \tag{2.42}$$

It seems that the continuum correlation function $\langle\psi_\alpha(x)\bar{\psi}_\beta(y)\rangle$ can be obtained by taking a naive continuum limit of the lattice correlator

$$\langle\psi_\alpha(x)\bar{\psi}_\beta(y)\rangle = \lim_{a\to 0}\frac{1}{a^3}G_{\alpha\beta}\left(\frac{x}{a},\frac{y}{a};ma\right), \tag{2.43}$$

where the factor $1/a^3$ come from the scale factor of the fermion field and $G_{\alpha\beta}(n,m;\hat{m}) \equiv K^{-1}_{\alpha\beta}(n,m)$. However, a problem occurs in this step. The Fourier transformation of the left-hand side of Eq. (2.43),

$$\langle\psi_\alpha(x)\bar{\psi}_\beta(y)\rangle = \lim_{a\to 0}\int_{-\pi/a}^{\pi/a}\frac{d^4p}{(2\pi)^4}\frac{[-i\sum\gamma_\mu\tilde{p}_\mu + M]_{\alpha\beta}}{\sum_\mu\tilde{p}_\mu^2 + M^2}e^{-ip(x-y)}, \tag{2.44}$$

with

$$\tilde{p}_\mu = \frac{1}{a}\sin(p_\mu a). \tag{2.45}$$

Taking the continuum limit $a \to 0$, the momentum in continuum space p_μ will be obtained. The problem comes from this continuum limit owing to the interval of integration of Eq. (2.44), $I = [-\pi/a, \pi/a]$. $\tilde{p}_\mu$ as a function of p_μ in the Brillouin zone (BZ) is shown

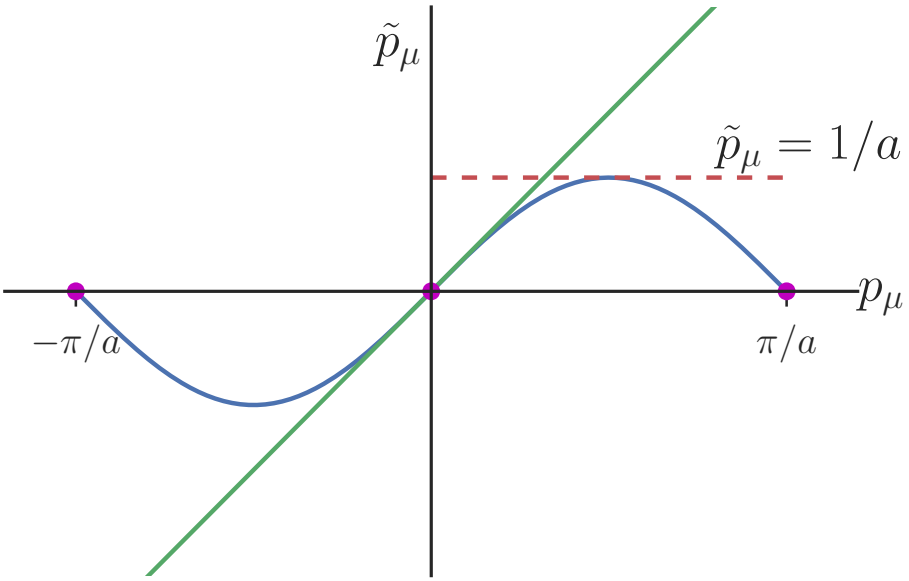

FIGURE 2.2: $\sin(p_\mu a)/a$ versus p_μ

in Fig. 2.2. The linear solid line expresses $\tilde{p}_\mu = p_\mu$. We can see that $p \simeq \tilde{p}$ around origin of p_μ. and $\tilde{p}_\mu = p_\mu$ in the limit $a \to 0$. However, this continuum limit fails around the edge of BZ. Because $\sin(p_\mu a) \to 0$ around the edge of BZ, this zero mode survives in the continuum limit. Since Eq. (2.44) has the 4-dimensional integral, $\tilde{p}$ has zero modes at 2^4 corners of BZ. Fifteen of them are lattice artifacts, the so-called doublers, which do not have physical correspondences. This problem is called the fermion doubling problem.

It is known as the Nielsen-Ninomiya theorem that one has to break the chiral symmetry to solve the fermion doubling problem respecting the Hermitian symmetry, the locality of interaction, and the translational symmetry [104, 105].

To eliminate the fermion doublers, one has to modify the definition of the discrete action. The lattice actions must converge on the continuum action Eq. (2.29) in the

continuum limit and many varieties of the lattice action are proposed.

2.1.3 Wilson Fermion

In this subsection we introduce the Wilson fermion, one of the definitions of the lattice action where the fermion doubling problem is eliminated in the continuum limit.

Wilson fermion is composed of S_F in Eq. (2.36) and an additional Wilson term,

$$S_F^{(W)} = S_F - \frac{r}{2}\sum_n \bar{\hat{\psi}}(n)\hat{\Box}\hat{\psi}(n), \tag{2.46}$$

where $\hat{\Box}$ is a dimensionless Laplacian defined as

$$\hat{\Box}\hat{\psi}(n) = \sum_\mu (\hat{\psi}(n+\mu) + \hat{\psi}(n-\mu) - 2\hat{\psi}(n)), \tag{2.47}$$

and the parameter r is called Wilson parameter. Since $\hat{\psi} = a^{3/2}\psi$ and $\hat{\Box} = a^2\Box$, the second term in Eq. (2.46) is linear with respect to a and vanishes in the continuum limit. Substituting Eq. (2.47) into Eq. (2.46), we obtain

$$S_F^{(W)} = \sum_{n,m} \bar{\hat{\psi}}_\alpha(n) K^{(W)}_{\alpha\beta}(n,m)\hat{\psi}(m), \tag{2.48}$$

$$\begin{aligned} K^{(W)}_{\alpha\beta}(n,m) &= (\hat{M}+4r)\delta_{n,m}\delta_{\alpha\beta} \\ &\quad - \frac{1}{2}\sum_\mu \left[(r-\gamma_\mu)_{\alpha\beta}\delta_{m,n+\hat{\mu}} + (r+\gamma_\mu)_{\alpha\beta}\delta_{m,n-\hat{\mu}}\right]. \end{aligned} \tag{2.49}$$

The two point correlation function obtained from $S_F^{(W)}$ in Eq. (2.48) is

$$\langle \hat{\psi}_\alpha(x)\bar{\hat{\psi}}_\beta(y)\rangle = \lim_{a\to 0}\int_{-\pi/a}^{\pi/a} \frac{d^4p}{(2\pi)^4}\frac{[-i\gamma_\mu\tilde{p}_\mu + M(p)]_{\alpha\beta}}{\sum_\mu \tilde{p}_\mu^2 + M(p)^2}, \tag{2.50}$$

$$M(p) = M + \frac{2r}{a}\sum_\mu \sin^2(p_\mu a/2). \tag{2.51}$$

2.1.4 Gauge field on the lattice

In this subsection we introduce the SU(3) gauge field on the lattice. The Lagrangian for the gauge field is determined naturally when we require the local gauge invariance. Therefore, to obtain the formulation of the gauge field on the lattice, we first consider the non-interacting Lagrangian of a fermion field.

Using Wilson fermion action Eq. (2.48) the fermion part of QCD Lagrangian Eq. (1.2) without the gauge field term can be written as

$$\begin{aligned} S_F^{(W)} =& (\hat{M}+4r)\sum_n\sum_{a=1}^{3}\bar{\psi}^a(n)\psi^a(n) \\ &- \frac{1}{2}\sum_{n,\mu}\sum_{\alpha=1}^{3}[\bar{\psi}^\alpha(n)(r-\gamma_\mu)\psi^\alpha(n+\hat{\mu}) + \bar{\psi}^\alpha(n+\hat{\mu})(r+\gamma_\mu)\psi^\alpha(n)]. \end{aligned} \tag{2.52}$$

This action is invariant under the global SU(3) gauge transformation,

$$\psi^{\alpha\prime}(n) = G_{\alpha\beta}\psi^\beta(n), \tag{2.53}$$

$$\bar{\psi}^{\alpha\prime}(n) = \bar{\psi}^\beta(n)G^{-1}_{\beta\alpha}, \tag{2.54}$$

with the element of SU(3),

$$G_{\alpha\beta} = \exp\left(-i\theta^a \frac{\lambda^a_{\alpha\beta}}{2}\right). \tag{2.55}$$

To obtain the theory with the local SU(3) invariance, we make the gauge transformation operator coordinate dependent,

$$G_{\alpha\beta}(n) = \exp\left(-i\theta^a(n) \frac{\lambda^a_{\alpha\beta}}{2}\right). \tag{2.56}$$

The first term on the right-hand side of Eq. (2.52) is invariant under the local gauge transformation since the term is local. On the other hand, the second term is gauge dependent because of non-locality of the term. Thus we have to modify the second term gauge to be gauge invariant. To make the second term gauge invariant, we introduce the link variable $U_\mu(n)$. If the gauge transformation of $U_\mu(n)$ is given by

$$U_\mu(n) \to G(n)U_\mu(n)G^{-1}(n + a\hat{\mu}), \tag{2.57}$$

$\bar{\psi}(n)U_\mu(n)\psi(n + a\hat{\mu})$ is gauge invariant. The object corresponding to $U_\mu(n)$ in the continuum theory is the Wilson line connecting the $x = na$ and $x + a\hat{\mu}$,

$$U(x, x + a\hat{\mu}) = P \exp\left(ig_0 \int_x^{x+a\hat{\mu}} dx_\mu A_\mu(x)\right), \tag{2.58}$$

where P means the path-ordered integral. Because of the gauge transformation of $A_\mu(x)$ shown in Eq. (1.8), the Wilson line satisfies the desired gauge transformation. When the gauge field $A_\mu(x)$ varies slowly in a small interval a, one can expand $U(x, x + a\hat{\mu})$ as

$$U(x, x + a\hat{\mu}) \simeq 1 + ig_0 a A_\mu(x). \tag{2.59}$$

Thus, when we define

$$U_\mu(n) \equiv e^{ig_0 a A_\mu(n)}, \tag{2.60}$$

$U_\mu(n)$ satisfies the gauge transformation Eq. (2.57). It is easily seen that the simplest gauge invariant composite of the link variables is the plaquette,

$$U_{\mu\nu}(n) = \mathrm{tr}(U_\mu(n)U_\nu(n + \hat{\mu})U^\dagger_\mu(n + \hat{\nu})U^\dagger_\nu(n)). \tag{2.61}$$

One also find the simplest gauge action, which is called Wilson gauge action, is given by

$$S_G = \beta \sum_{n,\mu>\nu} \left[1 - \frac{1}{6}\mathrm{tr}\left(U_{\mu\nu}(n) + U^\dagger_{\mu\nu}(n)\right)\right], \tag{2.62}$$

where

$$\beta = \frac{6}{g_0^2}. \tag{2.63}$$

2.2 Quantum Chromodynamics on the lattice

As we have shown in above section, we can modify the non-local term in the Wilson action Eq. (2.52) to be gauge invariant using $U_\mu(n)$ in Eq. (2.60). Then, the gauge

invariant Wilson fermion action is given by

$$S_F^{(W)} =(\hat{M}+4r)\sum_n\sum_{a=1}^{3}\bar{\psi}^a(n)\psi^a(n) \\ -\frac{1}{2}\sum_{n,\mu}\sum_{a=1}^{3}[\bar{\psi}^a(n)(r-\gamma_\mu)U_\mu(n)\psi^a(n+\hat{\mu})+\bar{\psi}^a(n+\hat{\mu})(r+\gamma_\mu)U_\mu^\dagger(n)\psi^a(n)]. \tag{2.64}$$

When we introduce the hopping parameter

$$\kappa=\frac{1}{8r+2\hat{M}}, \tag{2.65}$$

and redefine $\psi\to\frac{1}{\sqrt{2\kappa}}\psi$, Eq. (2.64) is written as

$$S_F^{(W)}=\sum_n\sum_{a=1}^{3}\bar{\psi}^a(n)K_{nm}(U)\psi^a(m), \tag{2.66}$$

$$K_{nm}(U)=\delta_{nm}-\kappa\sum_\mu\left[(r-\gamma_\mu)U_\mu(n)\delta_{n+\hat{\mu},m}+(r+\gamma_\mu)U_\mu^\dagger(n-\hat{\mu})\delta_{n-\hat{\mu},m}\right]. \tag{2.67}$$

Finally, from Eqs. (2.52) and (2.66), the QCD action with the Wilson gauge action and the Wilson fermion action is given by

$$S_{\mathrm{QCD}}=S_G+S_F^{(W)}. \tag{2.68}$$

2.3 Meson correlation function on the lattice

Two-point function measured on the lattice $\langle O_X(x)O_X^\dagger(0)\rangle$ can be used as a tool to access the stable hadronic states, with the operator $O_X(x)$ whose quantum numbers are same with those of the target hadronic states. In the case for the mesons, the operator is set as $O_X(x)=J^l(\tau,\boldsymbol{x})=\bar{\psi}(\tau,\boldsymbol{x})i\Gamma_H\psi(\tau,\boldsymbol{x})$, where the Dirac structure $\Gamma_H=1,\ \gamma^i,\ \gamma_5$, and $\gamma^i\gamma_5$ for the scalar, vector, pseudoscalar, and axial vector channels, respectively. In usual case, it is convenient to consider the Fourier transformation in the spatial coordinate of a Euclidean correlator

$$G_{XX}(\tau,\boldsymbol{p})=\sum_{\boldsymbol{x}}\langle O_X(\tau,\boldsymbol{x})O_X^\dagger(0,0)\rangle e^{-i\boldsymbol{p}\cdot\boldsymbol{x}}. \tag{2.69}$$

This correlator contains the information on hadronic states which couples to the measured operator. Inserting a complete set of states, $\sum_i\int\frac{d^3p'}{(2\pi)^3}\frac{1}{2E_i(\boldsymbol{p}')}|E_i(\boldsymbol{p}')\rangle\langle E_i(\boldsymbol{p}')|=1$, into Eq. (2.69), one obtains

$$G_{XX}(\tau,\boldsymbol{p})=\sum_{i=0}^{\infty}\frac{1}{2E_i(\boldsymbol{p})}\langle 0|O_X(0)|E_i(\boldsymbol{p})\rangle\langle E_i(\boldsymbol{p})|O_X^\dagger(0)|0\rangle e^{-E_i(\boldsymbol{p})\tau}, \tag{2.70}$$

where E_i is the i-th eigenvalue of H and we set $H|0\rangle=0$. When τ is long enough, the high energy states are suppressed exponentially and $G_{XX}(\tau,\boldsymbol{p})$ is dominated by the ground state $|E_0(\boldsymbol{p})\rangle$,

$$G_{XX}(\tau,\boldsymbol{p})\xrightarrow{\tau\to\infty}\frac{1}{2E_0(\boldsymbol{p})}\langle 0|O_X(0)|E_0(\boldsymbol{p})\rangle\langle E_0(\boldsymbol{p})|O_X^\dagger(0)|0\rangle e^{-E_0(\boldsymbol{p})\tau}. \tag{2.71}$$

In the right-hand side of Eq. (2.71), only $e^{-E_0(\boldsymbol{p})\tau}$ depends on τ. Thus one can extract information on the energy of the hadron state, which corresponds to the hadron mass when $\boldsymbol{p} = 0$, by fitting $G_{XX}(\tau, 0)$ by the exponentially damping function at the large τ. The effective mass is a useful indicator for a hadron mass [103]. The effective mass is defined as

$$m_{\text{eff}}(\tau)a = -\log \frac{G_{XX}(\tau + a)}{G_{XX}(\tau)}. \tag{2.72}$$

$m_{\text{eff}}(\tau)$ converge the grand state mass at $\tau \to \infty$.

Above discussion assumes that the length of τ can be taken infinitely large. In the finite temperature lattice simulation, the time extent is finite, $0 < \tau < aN_\tau$, and the periodic boundary condition (PBC) is imposed (in standard simulations). Since the correlator in PBC has a forward term $e^{-\tau m}$ and a backward term $e^{-m(1/T-\tau)}$, these contributions are mixed around $\tau \sim 1/T$. When $m_{\text{eff}}(\tau)a$ has a plateau as a function of τ, $m_{\text{eff}}(\tau)a$ in the region indicates the ground state mass which couples to the operator X.

2.4 Anisotropic lattice

The lattice gauge theory with a finite lattice spacing and finite volume has already been regularized. The ultraviolet and infrared cut off are the inverse of the lattice size and the inverse of the lattice spacing, respectively. To obtain a reasonable result concerning with heavy quarks the inverse of temporal lattice spacing $1/a_\tau$ must be sufficiently smaller than the quark mass. On the other hand, the resolution of momentum depends on the spatial length of the lattice. Therefore, an anisotropic lattice with a temporal lattice spacing smaller than the spatial one is a useful tool to study heavy quarks with finite momentum on the lattice [106]. Furthermore, the anisotropic lattice is suitable to increase the number of the temporal data points for an analysis [107]. It is a convenient feature for MEM analysis, which will be discussed in Chap. 4.

On the anisotropic lattice, the gauge couplings and hopping parameters for temporal and spatial components in the lattice action take different values. The Wilson gauge and Wilson fermion actions Eq. (2.68) is modified as [106–109]

$$S_G = \beta \sum_n \left[\sum_{i<j=1}^{3} \frac{1}{\xi_0} \left(1 - \frac{1}{6} \text{tr} \left(U_{ij}(n) + U_{ij}^\dagger(n) \right) \right) + \sum_{i=1}^{3} \xi_0 \left(1 - \frac{1}{6} \text{tr} \left(U_{i4}(n) + U_{i4}^\dagger(n) \right) \right) \right], \tag{2.73}$$

$$\begin{aligned} S_F^{(W)} = & \sum_n \sum_{a=1}^{3} \{ \bar{\psi}^a(n)\psi^a(n) \\ & - \kappa_t [\bar{\psi}^a(n)(r_t - \gamma_4)U_4(n)\psi^a(n+\hat{4}) + \bar{\psi}^a(n)(r_t + \gamma_4)U_4^\dagger(n-\hat{4})\psi^a(n-\hat{4})] \\ & - \kappa_s \sum_i [\bar{\psi}^a(n)(r_s - \gamma_i)U_i(n)\psi^a(n+\hat{i}) + \bar{\psi}^a(n)(r_s + \gamma_i)U_i^\dagger(n-\hat{i})\psi^a(n-\hat{i})] \}, \end{aligned} \tag{2.74}$$

where ξ_0 is bare anisotropy and, κ_t and κ_s are the temporal and spatial hopping parameters, respectively. The fermion anisotropy γ_F is defined as $\gamma_F = \kappa_\tau/\kappa_\sigma$. γ_F should be tuned to match the effective mass along spatial and temporal directions.

We note that ξ_0 is equivalent to the renormalized anisotropy $\xi = a_s/a_t$ only for the tree level analysis. In the lattice numerical simulations, the renormalized anisotropy must be determined non-perturbatively. The non-perturbative relation $\xi = \xi(\xi_0, \beta)$ for fixed β can be determined by Wilson loop matching [106, 110]. An analytic parametrization of

the renormalized anisotropy for the Wilson gauge action Eq. (2.73) is given in Ref. [106],

$$\frac{\xi(\xi_0,\beta)}{\xi_0} = 1 + \left(1 - \frac{1}{\xi_0}\right)\frac{\hat{\eta}_1(\xi_0)}{6}\frac{1+a_1 g^2}{1+a_0 g^2}g^2, \tag{2.75}$$

with

$$\hat{\eta}_1(\xi_0) = \frac{1.002503\xi_0^3 + 0.39100\xi_0^2 + 1.47130\xi_0 - 0.19231}{\xi_0^3 + 0.26287\xi_0^2 + 1.59008\xi_0 - 0.18224}, \tag{2.76}$$

$a_0 = -0.77810$, and $a_1 = -0.55055$.

The fermion anisotropy γ_F should also be determined non-perturbatively. In Ref. [39], $\gamma_F = 3.476$ for $\beta = 7.0$ and $\xi = 4$ is determined by comparing the temporal and spatial effective masses of the pseudoscalar and vector mesons.

2.5 Numerical simulation in lattice QCD

One of the advantages of the lattice QCD is that one can study the non-perturbative region of QCD using a numerical simulation on a computer.

Euclidean correlator of an operator $O(\bar{\psi},\psi,U)$ in the lattice QCD can be obtained by

$$\langle O(\bar{\psi},\psi,U)\rangle = \frac{\int dU d\bar{\psi} d\psi O(\bar{\psi},\psi,U)e^{-S}}{\int dU d\bar{\psi} d\psi e^{-S}}, \tag{2.77}$$

where S is the QCD action discussed in Sec. 2.1.4. Since the quark fields $\bar{\psi}$ and ψ are Grassmann variables, the integrals of $\bar{\psi}$ and ψ cannot be calculated on the computer straightforwardly. Because the fermion action is given by a bilinear form such as the Wilson fermion action in Eq. (2.48), the fermion degrees of freedom can be integrated out by performing the Grassmann integration. After the integrating out, the correlator Eq. (2.77) is given by

$$\langle O(U)\rangle = \frac{\int dU O(U) e^{-S_{\text{eff}}(U)}}{\int dU e^{-S_{\text{eff}}(U)}}, \tag{2.78}$$

$$S_{\text{eff}}(U) = S_G(U) - \ln\det K(U). \tag{2.79}$$

We note that a physical quantity in Eq. (2.78) is expressed by only the integral of the link variable U.

Let us consider the case for the two-point function of the interpolating operator $O_H(\tau,\boldsymbol{x}) = \bar{\psi}(x)\Gamma_H\psi(x)$. The two-point function is given by

$$\langle O_H(\tau,\boldsymbol{x})O_H^\dagger(0,0)\rangle = \langle\bar{\psi}(x)\Gamma_H\psi(x)\bar{\psi}(0)\overline{\Gamma}_H\psi(0)\rangle \tag{2.80}$$

$$= \frac{1}{Z}\int dU \det K(U) e^{-S_G(U)}\text{tr}\left[K^{-1}(x,0)\Gamma_H K^{-1}(0,x)\Gamma_H^\dagger\right] - \frac{1}{Z}\int dU \det K(U) e^{-S_G(U)}\text{tr}\left[K^{-1}(0,0)\Gamma_H\right]\text{tr}\left[K^{-1}(x,x)\Gamma_H^\dagger\right], \tag{2.81}$$

where the traces run over color and spinor indices, and $K^{-1}(x,0)$ is the quark propagator. If one performs the integral of U numerically, we can obtain $\langle O_H(\tau,\boldsymbol{x})O_H^\dagger(0,0)\rangle$. However, the dimension of the integrals is too large to perform on the computer in a naive algorithm. The integrals cannot be finished in realistic time with enough numerical precision.

Fortunately, since the paths mainly contributing for the path integral concentrate on a part of the phase space, one can use the importance sampling method to evaluate a correlation function.

The Euclidean correlation function with zero chemical potential can be interpreted as a statistical average of an observable with probability $e^{-S_{\rm eff}(U)}$, since $S_{\rm eff}(U)$ is a real functional. When we generate gauge configurations following the probability distribution, we thus obtain

$$\langle O(U)\rangle = \frac{1}{Z}\int dU O(U) e^{-S_{\rm eff}(U)} \tag{2.82}$$

$$\simeq \frac{1}{N}\sum_{i=1}^{N} O_i, \tag{2.83}$$

where N is the number of the generated configurations and O_i is the value of$O(U)$ measured on the i-th gauge configuration. In the lattice numerical simulation, one generate gauge configurations with Monte Carlo methods and measure a physical quantity using Eq. (2.83).

Because the numerical cost calculating $\det K(U)$ is large, one sometimes employs the approximation $\det K(U) \to 1$, which is called the quench approximation. The quench approximation corresponds to the one which neglects the corrections arising from the pair creation and annihilation of quarks and anti-quarks in vacuum. Adopting the quench approximation causes uncontrollable systematic errors. One of the significant difference between the quenched QCD and the full QCD is the critical temperature ($T_{\rm c}$): $T_{\rm c} \sim$ 150MeV for the full QCD [19–22], while $T_{\rm c} \sim$ 270MeV for the quenched QCD [111]. However, there is many interesting observables for which the systematic errors are small. For example, difference between the light meson mass spectrum on the quenched lattice and the experimental data is about 10% [112].

Chapter 3

Correlators and Spectral Functions

In this chapter, we review the relation between the Minkowski-space correlators and the Euclidean-space correlators, which are relevant to our study. After the definition of the correlators, we discuss the properties of the spectral functions, such as a peak corresponding to a bound state and the relation between the temporal and spatial spectral functions in the vector channel.

3.1 Definition of Correlators

These relations are shown in many textbooks and reviews in the finite temperature quantum field theory [49, 91, 113, 114].

In the following discussions, $\langle \hat{A} \rangle$ is understood as the thermal expectation value,

$$\langle \hat{A} \rangle = \langle \mathrm{Tr}\{\hat{\rho}\hat{A}\} \rangle \tag{3.1}$$

$$= \sum_n \langle n|\hat{\rho}\hat{A}|n\rangle, \tag{3.2}$$

with a density matrix

$$\hat{\rho} \equiv \frac{1}{Z} e^{-\beta \hat{H}}, \tag{3.3}$$

where the partition function Z is a normalization constant such that $\langle \hat{\rho} \rangle = 1$, β is the inverse temperature $\beta = 1/T$, and the trace is taken over all eigenstates of $\hat{H}$. For convenience, we drop the hat from operators in the following without the confusing situations.

First, we introduce the following correlation functions:

$$G^{>}_{XY}(t) \equiv \mathrm{Tr}\left\{\hat{\rho}X(t)Y(0)\right\}, \tag{3.4}$$

$$G^{<}_{XY}(t) \equiv \mathrm{Tr}\left\{\hat{\rho}Y(0)X(t)\right\}, \tag{3.5}$$

$$G^{R}_{XY}(t) \equiv i\mathrm{Tr}\{\hat{\rho}[X(t), Y(0)]\}\theta(t), \tag{3.6}$$

where $G^{R}_{XY}(t)$ is the retarded correlator. Let us see the properties of $G^{>}_{XY}(t)$, $G^{<}_{XY}(t)$, and $G^{R}_{XY}(t)$. Because of time-translation invariance of the density matrix Eq. (3.3), we find

$$G^{<}_{XY}(t) = G^{>}_{YX}(-t). \tag{3.7}$$

The reality property is given as

$$\begin{aligned} G^{>}_{X^\dagger Y^\dagger}(t) &= \mathrm{Tr}\{\hat{\rho} X^\dagger(t) Y^\dagger(0)\} \\ &= (\mathrm{Tr}\{\hat{\rho}^* Y(0) X(t^*)\})^* \\ &= G^{>}_{YX}(-t^*)^* \end{aligned} \tag{3.8}$$

Furthermore, when we express $X(t)$ with the Heisenberg representation $X(t) = e^{iHt}X(0)e^{-iHt}$, we find

$$G^{>}_{XY}(t) = G^{>}_{YX}(-t - i\beta), \tag{3.9}$$

where we have used the cyclic property of the trace.

Next, we introduce the expectation value of a commutator,

$$G_{XY}(t) = i\mathrm{Tr}\{\hat{\rho}[X(t), Y(0)]\} = i(G^{>}_{XY}(t) - G^{<}_{XY}(t)), \tag{3.10}$$

From Eqs. (3.7) and (3.8), we obtain

$$G_{XY}(-t) = -G_{YX}(t), \tag{3.11}$$

$$G_{X^\dagger Y^\dagger}(t) = G_{XY}(t^*)^*. \tag{3.12}$$

The spectral function is defined as the Fourier transform of Eq. (3.10),

$$\rho_{XY}(\omega) = \frac{1}{2\pi i}\int_{-\infty}^{\infty} dt e^{i\omega t} G_{XY}(t). \tag{3.13}$$

Taking the Fourier-Laplace transform of $G_{XY}(t)$ over the positive half-axis, we obtain

$$G^R_{XY}(\omega) = \int_0^{\infty} dt e^{i\omega t} G_{XY}(t), \tag{3.14}$$

which is analytic in the half upper plane $\mathrm{Im}\,\omega > 0$.

From Eqs. (3.11) and (3.12), one finds

$$\rho_{XY}(\omega) = \frac{1}{2\pi i}\left(G^R_{XY}(\omega) - G^R_{Y^\dagger X^\dagger}(\omega)^*\right). \tag{3.15}$$

In the case for $Y = X^\dagger$, the spectral function is given by the imaginary part of the retarded correlator divided by π,

$$\rho_{XX^\dagger}(\omega) = \frac{1}{\pi}\,\mathrm{Im}\, G^R_{XX^\dagger}(\omega), \tag{3.16}$$

which means that $\rho_{XX^\dagger}(\omega)$ is a real function.

The Euclidean correlator $G^E_{XY}(t)$ is defined as the forward correlator $G^{>}_{XY}(t)$ in imaginary time space,

$$G^E_{XY}(t) = G^{>}_{XY}(-it). \tag{3.17}$$

In the following, we denote imaginary time by τ . We obtain

$$G^E_{XY}(\beta - \tau) = G^E_{YX}(\tau), \tag{3.18}$$

as a special case of Eq. (3.9).

Let us consider the spectral representation of these correlators to find the relation between them. First, inserting the complete set of energy eigenstates $1 = \sum_m |m\rangle\langle m|$

into $G^{>}_{XY}(t)$ and $G^{<}_{XY}(t)$, we obtain

$$\begin{aligned} G^{>}_{XY}(t) &= \sum_n \langle n|\hat{\rho}X(t)Y(0)|n\rangle \\ &= \frac{1}{Z}\sum_{n,m}\langle n|e^{-\beta H}e^{itH}X(0)e^{-itH}|m\rangle\langle m|Y(0)|n\rangle \\ &= \frac{1}{Z}\sum_{n,m} e^{-\beta E_n}e^{it(E_n-E_m)}X_{nm}Y_{mn}, \end{aligned} \tag{3.19}$$

$$G^{<}_{XY}(t) = \frac{1}{Z}\sum_{n,m} e^{-\beta E_n}e^{it(E_m-E_n)}Y_{nm}X_{mn}, \tag{3.20}$$

with the matrix element $X_{nm} \equiv \langle n|X(0)|m\rangle$. The spectral representation for $G^{R}_{XY}(t)$ and $G^{E}_{XY}(\tau)$ is given by

$$\begin{aligned} G^{R}_{XY}(t) &= i(G^{>}_{XY}(t) - G^{<}_{XY}(t)) \\ &= \frac{2i}{Z}\sum_{n,m} X_{mn}Y_{nm}e^{-\beta(E_n+E_m)/2}\sinh\left(\frac{\beta E_{nm}}{2}\right)e^{-iE_{nm}t}, \end{aligned} \tag{3.21}$$

$$G^{E}_{XY}(\tau) = \frac{1}{Z}\sum_{n,m} e^{-\beta E_m}e^{-\tau(E_{nm})}X_{mn}Y_{nm}, \tag{3.22}$$

where $E_{nm} = E_n - E_m$. The spectral representation for the retarded correlator is obtained by integrating Eq. (3.21) over the real t,

$$G^{R}_{XY}(\omega) = \frac{2}{Z}\sum_{n,m}\frac{-X_{mn}Y_{nm}}{\omega - E_{nm}}e^{-\beta(E_n+E_m)/2}\sinh\left(\frac{\beta E_{nm}}{2}\right). \tag{3.23}$$

Substituting Eq. (3.23) into Eq. (3.15), we obtain

$$\frac{\rho_{XY}(\omega)}{2\sinh\frac{\beta\omega}{2}} = \frac{1}{Z}\sum_{m,n} X_{mn}Y_{nm}e^{-\beta(E_n+E_m)/2}\delta(\omega - E_{mn}). \tag{3.24}$$

Finally, from Eqs. (3.22) and (3.24) we find the relation between the Euclidean correlator and the spectral function,

$$G^{E}_{XY}(\tau) + G^{E}_{XY}(\beta-\tau) = \int_{-\infty}^{\infty} d\omega\rho_{XY}(\omega)\frac{\cosh\left(\left(\tau-\frac{\beta}{2}\right)\omega\right)}{\sinh\beta\omega/2}, \tag{3.25}$$

In a special case $Y = X^\dagger$, from Eq. (3.24) we find $\rho_{XX^\dagger}(\omega)$ is an odd function in this case and we have

$$G^{E}_{XX^\dagger}(\tau) = \int_{0}^{\infty} d\omega\rho_{XX^\dagger}(\omega)\frac{\cosh\left(\left(\tau-\frac{\beta}{2}\right)\omega\right)}{\sinh\beta\omega/2}, \tag{3.26}$$

We also find $\rho_{XX^\dagger}(\omega \geq 0) \geq 0$ in this case.

The difference between the finite-temperature and zero-temperature is interpreted as the change of the spectral function. To study the change of the spectral function from $G^{E}_{XX^\dagger}(\tau)$, the reconstructed correlator defined as

$$G^{E,\mathrm{rec}}_{XX^\dagger}(\tau, T; T') \equiv \int_{0}^{\infty} d\omega\rho_{XX^\dagger}(\omega, T')\frac{\cosh\left(\left(\tau-\frac{\beta}{2}\right)\omega\right)}{\sinh\beta\omega/2}, \tag{3.27}$$

is a convenient tool [91]. The difference between $G^{E}_{XX^\dagger}(\tau, T')$ and $G^{E,\mathrm{rec}}_{XX^\dagger}(\tau, T; T')$ represents the thermal modification for the spectral function. Using the identity

$$\frac{\cosh\left(\left(\tau - \frac{\beta}{2}\right)\omega\right)}{\sinh \beta\omega/2} = \sum_{m\in \boldsymbol{Z}} e^{-\omega|\tau+m\beta|}, \tag{3.28}$$

we obtain the exact relation

$$G^{E,\mathrm{rec}}_{XX^\dagger}\left(\tau, T; \frac{1}{2}T\right) = G^{E}\left(\tau, \frac{1}{2}T\right) + G^{E}\left(\beta - \tau, \frac{1}{2}T\right). \tag{3.29}$$

3.2 Spectral function and Euclidean correlator

Dynamical properties of quarkonia in the vector and pseudoscalar channels are encoded in the Euclidean correlators

$$G^{lm}(\tau, \boldsymbol{p}) = \int d^3x e^{i\boldsymbol{p}\cdot\boldsymbol{x}} \left\langle J^l(\tau, \boldsymbol{x}) J^{m\dagger}(0,0)\right\rangle, \tag{3.30}$$

where the imaginary time τ is restricted to the interval $0 \le \tau < 1/T$ and $J^l(\tau, \boldsymbol{x}) = \bar{\psi}(\tau, \boldsymbol{x}) i\gamma^l \psi(\tau, \boldsymbol{x})$ is the local interpolating operator in the Heisenberg representation with the quark field $\psi(\tau, \boldsymbol{x})$ with $l = 0, 1, 2$, and 3 for the vector channel and $l = 5$ for the pseudoscalar channel.

From Eq. (3.25) the spectral function $\rho^{lm}(\omega, \boldsymbol{p})$ corresponding to $G^{lm}(\tau, \boldsymbol{p})$ is given by

$$G^{lm}(\tau, \boldsymbol{p}) + G^{lm}(\beta - \tau, \boldsymbol{p}) = \int_{-\infty}^{\infty} d\omega \rho^{lm}(\omega, \boldsymbol{p}) \frac{\cosh\left(\left(\tau - \frac{\beta}{2}\right)\omega\right)}{\sinh \beta\omega/2}. \tag{3.31}$$

In the special case of the diagonal components of the spectral functions $\rho^{ll}(\omega, \boldsymbol{p})$, the relation Eq. (3.31) is rewritten by the Laplace-like transformation shown in Eq. (3.26) as

$$G^{ll}(\tau, \boldsymbol{p}) = \int_0^{\infty} K(\tau, \omega) \rho^{ll}(\omega, \boldsymbol{p}) d\omega, \tag{3.32}$$

with

$$K(\tau, \omega) = \frac{e^{-\tau\omega} + e^{-(1/T-\tau)\omega}}{1 - e^{-\omega/T}}. \tag{3.33}$$

In the following, we represent the diagonal components of the spectral functions as

$$\rho^{l}(\omega, \boldsymbol{p}) = \rho^{ll}(\omega, \boldsymbol{p}). \tag{3.34}$$

In the vacuum, as a consequence of Lorentz invariance and charge conservation, the vector spectral function can be represented as

$$\rho^{\mu\nu}(\omega, \boldsymbol{p}) = \left(\frac{p^\mu p^\nu}{P^2} - g^{\mu\nu}\right) \rho_{\mathrm{V}}(P^2), \tag{3.35}$$

with $\mu, \nu = 0, 1, 2$, and 3 and $P^2 = \omega^2 - |\boldsymbol{p}|^2$. When there is a bound state which couples to J^l, the corresponding spectral function $\rho_{\mathrm{V}}(\omega, p) = \rho_{\mathrm{V}}(P^2)$ or $\rho_{\mathrm{PS}}(\omega, p) = \rho^5(\omega, \boldsymbol{p})$ has a peak structure around $\omega \simeq \pm E(p)$, where $E(p)$ is the dispersion relation of the bound

state with $p = |\boldsymbol{p}|$. The peak structure is approximately given by a delta function,

$$Z\delta(\omega^2 - E(p)^2) = \frac{Z}{2E(p)}\delta\left(\omega - E(p)\right), \tag{3.36}$$

where the right-hand side represents the peak at $\omega > 0$, and $Z > 0$ is the residue. Because of Lorentz invariance, $E(p)$ in the vacuum is given by

$$E(p) = \sqrt{m^2 + p^2}, \tag{3.37}$$

where m is the mass of the bound state. It is also shown from Lorentz invariance that Z in Eq. (3.36) does not have momentum dependence.

The property of the bound state peak in Eqs. (3.36) and (3.37) is modified at finite temperature. First, the width of the peak becomes larger and the delta function in Eq. (3.36) is replaced by a smooth function with a peak. Second, because Lorentz invariance is lost in medium, Z can depend on momentum. The dispersion relation $E(p)$ can also be modified from the Lorentz covariant form Eq. (3.37).

At finite temperature, $\rho^{\mu\nu}(\omega, \boldsymbol{p})$ in Eq. (3.35) is decomposed into the transverse and longitudinal components as [114]

$$\rho^{\mu\nu}(\omega, \boldsymbol{p}) = P_{\mathrm{T}}^{\mu\nu}\rho_{\mathrm{T}}(\omega, p) + P_{\mathrm{L}}^{\mu\nu}\rho_{\mathrm{L}}(\omega, p), \tag{3.38}$$

where the projection operators onto the transverse and longitudinal components, P_{T} and P_{L}, respectively, are defined as

$$P_{\mathrm{T}}^{00} = P_{\mathrm{T}}^{0i} = P_{\mathrm{T}}^{i0} = 0, \tag{3.39}$$

$$P_{\mathrm{T}}^{ij} = \delta^{ij} - p^i p^j / p^2, \tag{3.40}$$

$$P_{\mathrm{L}}^{\mu\nu} = p^\mu p^\nu / P^2 - g^{\mu\nu} - P_{\mathrm{T}}^{\mu\nu}, \tag{3.41}$$

with $i, j = 1, 2$, and 3. The transverse and longitudinal spectral functions $\rho_{\mathrm{T}}(\omega, p)$ and $\rho_{\mathrm{L}}(\omega, p)$ are identical in the vacuum, $\rho_{\mathrm{T}}(\omega, p) = \rho_{\mathrm{L}}(\omega, p) = \rho_{\mathrm{V}}(\omega, p)$, from Eq. (3.35). When the momentum is taken as $\boldsymbol{p} = (p, 0, 0)$, $\rho_{\mathrm{T}}(\omega, p)$ and $\rho_{\mathrm{L}}(\omega, p)$ are related to $\rho^i(\omega, \boldsymbol{p})$ as

$$\rho_{\mathrm{T}}(\omega, p) = \frac{1}{2}\left(\rho^2(\omega, \boldsymbol{p}) + \rho^3(\omega, \boldsymbol{p})\right), \tag{3.42}$$

$$\rho_{\mathrm{L}}(\omega, p) = \frac{\omega^2 - p^2}{\omega^2}\rho^1(\omega, \boldsymbol{p}). \tag{3.43}$$

From the general property of the spectral function, $\rho^l(\omega, \boldsymbol{p})$ are semi-positive for $\omega > 0$ [114]. The semi-positivity of $\rho_{\mathrm{T}}(\omega, p)$ is then guaranteed from Eq. (3.42). On the other hand, Eq. (3.43) shows that $\rho_{\mathrm{L}}(\omega, p)$ is semi-negative in the space-like region $0 < \omega < p$.

As we will see in Chap. 5, the slope of $\rho_L(\omega, 0)$ at the origin of ω is related with the transport coefficient by the Kubo formula.

Chapter 4

Maximum entropy method

In this chapter, I give a review of the maximum entropy method (MEM) on the basis of Ref. [48, 49, 115].

To obtain the spectral function from the lattice Euclidean correlator, we have to take the inverse transformation of Eq. (3.26). The simplest approach to take the transformation is to employ the ansatz for the structure of the spectral function. In this case, however, one have to take a continuum limit to remove an unphysical object deriving from doubler and the result depend on ansatz. MEM [48, 49] is a method to infer the most probable image of the spectral function from a limited number of data points for a Euclidean correlator on the basis of Bayes' theorem. An advantage of MEM is that a tool to study the plausibility of a reconstructed image is provided in MEM itself. MEM analysis requests to introduce the default model, which expresses the prior knowledge on the spectral function, such as the semi-positivity, the high energy behavior of the spectral function and etc. One can examine the validity of a default model by the error analysis of MEM. If an employed default model is not good, the plausibility of the reconstructed image become small and one cannot find a significant conclusion.

This chapter is organized as follows. We first show you the basic of MEM in Sec. 4.1. Next, we review the method of the numerical MEM analysis in Sec. 4.2.

4.1 Reconstruction of the spectral function

In the analysis of a spectral function $A(\omega)$ corresponding to a Euclidean correlator $G(\tau)$ obtained in a Monte Carlo simulation with Eq. (3.32), the most important quantity is the χ-square,

$$\chi^2 = \sum_{i,j} \left(G(\tau_i) - G_\rho(\tau_i)\right) C_{ij}^{-1} \left(G(\tau_j) - G_\rho(\tau_j)\right), \tag{4.1}$$

where the correlation between different temporal points τ_i is encoded in the covariance matrix

$$C_{ij} \equiv \frac{1}{N(N-1)} \sum_{n=1}^{N} \left(G_n(\tau_i) - G(\tau_i)\right) \left(G_n(\tau_j) - G(\tau_j)\right), \tag{4.2}$$

i and j run over discrete temporal points, N is the number of the gauge configuration and $G_\rho(\tau_i)$ is the correlator defined by Eq. (3.32) from the spectral function $\rho(\omega)$.

In the standard least-square method, $\rho(\omega)$ is determined so as to minimize Eq. (4.1). Because the number of the degrees of the freedom of the continuous function $\rho(\omega)$ is larger than the one of the discrete data for $G(\tau)$, however, the minimum of χ^2 is heavily degenerating. To choose one, some ansatz to constrain the functional form of $\rho(\omega)$ is required.

In order to remove this degeneracy, MEM introduces a prior probability represented by the Shannon-Jaynes entropy [115],

$$S = \int_0^\infty \left[\rho(\omega) - m(\omega) - \rho(\omega)\log\left(\frac{\rho(\omega)}{m(\omega)}\right)\right] d\omega, \tag{4.3}$$

where the default model $m(\omega)$ expresses prior knowledge. From Bayes' theorem, it is obtained that the conditional probability of having $\rho(\omega)$ from $G(\tau)$ and the prior knowledge is proportional to $P(\rho,\alpha) = \exp[Q(\rho,\alpha)]$ [49], where

$$Q(\rho,\alpha) = \alpha S(\rho) - \frac{1}{2}\chi^2(\rho). \tag{4.4}$$

The parameter α controls the relative weight between χ^2 and S. It is known that the spectral image that maximizes $P(\rho,\alpha)$ for a given α is unique if it exists [49]. The final output image $\rho_{\rm out}(\omega)$ is obtained by integrating $\rho(\omega)$ with a weight $P(\rho,\alpha)$ over α and ρ space as

$$\rho_{\rm out}(\omega) = \langle\!\langle \rho(\omega) \rangle\!\rangle, \tag{4.5}$$

where

$$\langle\!\langle \mathcal{O} \rangle\!\rangle = \frac{1}{Z_{\rm P}} \int d\alpha \int [d\rho]\, P(\rho,\alpha)\mathcal{O}, \tag{4.6}$$

is the average over the plausibility $P(\rho,\alpha)$ with $Z_{\rm P} \equiv \int d\alpha \int [d\rho] P(\rho,\alpha)$. Here, the measure $[d\rho]$ is defined as

$$[d\rho] \equiv \lim_{N_\omega\to\infty} \prod_{l=1}^{N_\omega} \frac{d\rho_l}{\sqrt{\rho_l}}, \tag{4.7}$$

with the discretized spectral function $\rho_l = \rho(\omega_l)$ with discrete ω values ω_l [49]. When $P(\rho,\alpha)$ is sharply peaked around $\rho_\alpha(\omega)$, Eq. (4.5) is well approximated as

$$\rho_{\rm out}(\omega) \simeq \frac{1}{Z_{\rm P}} \int d\alpha \rho_\alpha(\omega) P(\alpha), \tag{4.8}$$

where

$$P(\alpha) \equiv \int [d\rho] P(\rho,\alpha). \tag{4.9}$$

4.1.1 Error analysis

A characteristic of MEM is that this method enables us to estimate the error of quantities given by the integral of a function of $\rho_{\rm out}(\omega)$ quantitatively.

Let us consider a quantity given by the weighted integral of $\rho(\omega)$ with a weight function $f(\omega)$ and an interval $I = [\omega_{\rm min}, \omega_{\rm max}]$,

$$W = \int_I f(\omega)\rho(\omega) d\omega. \tag{4.10}$$

In MEM, the average of W is estimated as

$$\langle W \rangle = \left\langle\!\!\left\langle \int_I d\omega f(\omega)\rho(\omega) \right\rangle\!\!\right\rangle, \tag{4.11}$$

and the error of $\langle W \rangle$ is given by the variance of W in $P(\rho, \alpha)$ space as

$$\Delta W = \sqrt{\langle\!\langle (\delta W)^2 \rangle\!\rangle}, \tag{4.12}$$

where $\delta W = W - \langle\!\langle W \rangle\!\rangle$.

Typically, the magnitude of the error estimated in this way becomes larger as the interval I becomes narrower. In particular, when one makes the error estimate of $\rho_{\rm out}(\omega)$ at a given ω with $f(\omega') = \delta(\omega' - \omega)$, one obtains a huge error $\Delta\rho_{\rm out}(\omega) \gg \rho_{\rm out}(\omega)$. This means that the functional form of $\rho_{\rm out}(\omega)$ itself does not have quantitative meaning. For example, it does not make sense to distinguish whether the functional form of a peak structure in $\rho_{\rm out}(\omega)$ is Gaussian or Lorentzian in MEM. The values of the position and width of the peak do not have statistically relevant meanings, either. In order to obtain a moderate value of the error, the interval I has to be chosen sufficiently large. This limitation of the analysis is associated with reconstructing apparently more information than the original one. Even if the correlators $G(\tau_i)$ for discrete τ_i's are determined with an infinitesimal statistical error, the reconstructed image $\rho_{\rm out}(\omega)$ still have error. This is because the error in MEM includes intrinsic one associated with the introduction of the entropy, in addition to statistical one. Thus, for instance, it is not sufficient to estimate the error in the result with the Jackknife methods, which takes account of only the statistical error. The error analysis with Eq. (4.12) is essential and absolutely necessary [49].

4.2 Numerical analysis

In practical numerical analysis of MEM one reconstructs the spectral function on the basis of Eq. (4.8). The outline of our procedure is following:

1. Search $\alpha = \hat{\alpha}$ maximizing $P(\hat{\alpha})$ in Eq. (4.9).
2. Search the range of α, $[\alpha_{\rm min}, \alpha_{\rm max}]$, where $P(\alpha) \geq P(\hat{\alpha})/10$.
3. Approximate Eq. (4.8) as

$$\rho_{\rm out}(\omega) \simeq \frac{1}{Z_{\rm P}} \sum_{i=0}^{N_\alpha} \rho_{\alpha_i} P(\alpha_i) \Delta\alpha, \tag{4.13}$$

   where $\Delta\alpha = (\alpha_{\rm max} - \alpha_{\rm min})/(N_\alpha + 1)$ and $\alpha_i = \alpha_{\rm min} + i\Delta\alpha$.
4. Search ρ_{α_i} and calculate Eq. (4.13).
5. Estimate the error Eq. (4.12) using ρ_{α_i} and $P(\alpha_i)$.

In these steps one (usually) uses a few techniques. First one uses the method of steepest descent to calculate the integration in Eq. (4.9) [48, 49]. To use the method of steepest descent one has to find the saddle point solving the optimization problem where the degree of freedom is N_ω. Since the integration in Eq. (4.9) has to be performed many times in MEM analysis, The numerical cost is large.

Second one have to solve the optimization problem where the degree of freedom is N_ω to use the method of steepest descent. The degree of freedom can be reduced into N_τ by using Bryan's method [115]. The singular value decomposition and the saddle point method play important roles in this method.

For the numerical analysis we introduce a discretized quantity in ω-space

$$\omega_l = l \cdot \Delta\omega, \;\; \rho_l = \rho(\omega_l) \cdot \Delta\omega, \qquad\qquad (l = 1, 2, \cdots, N_\omega). \tag{4.14}$$

4.2.1 Method of steepest descent

In numerical analysis the multiple-integration about ρ_l in Eq. (4.9) cannot be performed exactly. First, thus, we suppose that $P(\rho, \alpha)$ has a sharp peak around $\rho = \rho_\alpha$, where ρ_α is ρ which maximizes $Q(\rho, \alpha)$ with the fixed α,

$$\left.\frac{\delta Q}{\delta \rho}\right|_{\rho=\rho_\alpha} = 0. \tag{4.15}$$

When we change variable $\varepsilon_l = \sqrt{\rho_l}$ and use the Gaussian approximation, we obtain

$$\begin{aligned} P(\rho, \alpha) &= \exp\left(\alpha S(\rho) - \frac{1}{2}\chi^2(\rho)\right) \\ &\approx \exp\left(Q(\rho_\alpha, \alpha) + \frac{1}{2}\sum_{ijkl} \delta\varepsilon_i \delta\varepsilon_j \frac{\partial \rho_k}{\partial \varepsilon_i}\frac{\partial \rho_l}{\partial \varepsilon_j}\left.\frac{\partial^2 Q(\rho, \alpha)}{\partial \rho_k \partial \rho_l}\right|_{\rho=\rho_\alpha}\right), \end{aligned} \tag{4.16}$$

where $\delta\varepsilon_i = \varepsilon_i - \varepsilon_{\alpha i}$. Because

$$\frac{\partial^2 Q}{\partial \rho_k \partial \rho_l} = -\frac{\alpha \delta_{kl}}{\sqrt{\rho_k \rho_j}} - \frac{\partial^2 L}{\partial \rho_k \partial \rho_l}, \tag{4.17}$$

$$\frac{\partial^2 L}{\partial \rho_k \partial \rho_l} = \sum_{ij} K_{ki} C_{ij}^{-1} K_{lj}, \tag{4.18}$$

$$\frac{\partial \rho_k}{\partial \varepsilon_l} = \sqrt{\rho_k}\delta_{kl}. \tag{4.19}$$

Eq. (4.16) can be rewritten as

$$P(\rho, \alpha) \approx \exp\left(Q(\rho_\alpha, \alpha) + \frac{1}{2}\sum_{kl} \delta\varepsilon_k (\alpha\delta_{kl} + \Lambda_{kl})\delta\varepsilon_l\right), \tag{4.20}$$

where

$$\Lambda_{kl} = \sqrt{\rho_k}\left.\frac{\partial^2 L}{\partial \rho_k \partial \rho_l}\sqrt{\rho_l}\right|_{\rho=\rho_\alpha}. \tag{4.21}$$

Substituting Eq. (4.20) into Eq. (4.9), we find

$$P(\alpha) = (2\pi)^{N_\omega/2} \exp\left(\frac{1}{2}\sum_k \log\frac{\alpha}{\alpha + \lambda_k} + Q(\rho_\alpha, \alpha)\right), \tag{4.22}$$

where λ_k is the eigen value of Λ_{kl}. When we find ρ_α numerically, we can calculate Eq. (4.11).

To calculate the error of MEM in Eq. (4.12) we need one more step. Now we want to calculate

$$\left\langle\!\left\langle (\delta W)^2 \right\rangle\!\right\rangle = \frac{1}{Z_P}\int d\alpha \int [d\rho] \int_{I\times I} d\omega d\omega' f(\omega)\delta\rho(\omega) f(\omega')\delta\rho(\omega') P(\rho, \alpha) \tag{4.23}$$

$$\simeq \int d\alpha \int_{I\times I} d\omega d\omega' f(\omega) f(\omega') \left(\frac{\delta^2 Q}{\delta\rho(\omega)\delta\rho(\omega')}\right)^{-1}_{\rho=\rho_\alpha}, \tag{4.24}$$

where in the second line we used the saddle point method and the Gaussian integration. For the discretized quantities,

$$\frac{\delta^2 Q}{\delta\rho_l \delta\rho_m} = -\alpha\frac{\delta_{lm}}{\rho_l} - K_{li}^T C_{ij}^{-1} K_{jm}. \tag{4.25}$$

Taking the inverse of Eq. (4.25), Eq. (4.24) can be calculated numerically.

4.2.2 Singular value decomposition

To find ρ_α we have to solve the optimization problem with the degree of freedom is N_ω. R. K. Bryan proposed the method reducing the degree of freedom using the singular value decomposition[115].

Now we are interested in solving Eq. (4.15). Substituting Eq. (4.4) into Eq. (4.15) we find

$$-\alpha \log\frac{\rho_l}{m_l} = \sum_i K_{il}\frac{\partial L}{\partial G_{\rho_i}}, \tag{4.26}$$

where $K_{il} = K(\tau_i, \omega_l)$.

Let us introduce the singular value decomposition of the kernel,

$$K = V\Sigma U^T, \tag{4.27}$$

where V is a $N_\tau \times N_\tau$ orthogonal matrix, U is a $N_\omega \times N_\tau$ orthogonal matrix and Σ is a $N_\tau \times N_\tau$ matrix. Σ is a diagonal matrix, $\Sigma_{ii} = \sigma_i, i = 1, \ldots, N_\tau$, where σ_i is called a singular value of K and $N_\tau = rank(K)$. The column space of U is called the singular value space.

Because we can see that the right-hand side of Eq. (4.26) is in the singular space, the left-hand side of Eq. (4.26) also should be in the singular space. We, thus, parametrize ρ_l as

$$\rho_l = m_l \exp a_l, \ (1 \le l \le N_\omega), \tag{4.28}$$

$$a_l = \sum_{t=1}^{N_\tau} U_{lt} b_t \tag{4.29}$$

where $\boldsymbol{a} = (a_1, a_2, \ldots, a_{N_\omega})$ is a real vector. Because of the semi-positivity of the spectral function, this parametrization is valid. Substituting Eq. (4.28) into Eq. (4.26), we find

$$-\alpha U\boldsymbol{b} = U\Sigma V^T \frac{\partial L}{\partial G_\rho}. \tag{4.30}$$

Using orthogonality of U, $UU^T = I$,

$$-\alpha\boldsymbol{b} = \Sigma V^T \frac{\partial L}{\partial \boldsymbol{G}_\rho} \equiv \boldsymbol{g}. \tag{4.31}$$

Eq. (4.31) can be solved using Newton's method. The Jacobian of the system is given by

$$J = \alpha I + \frac{\partial \boldsymbol{g}}{\partial \boldsymbol{b}}, \tag{4.32}$$

$$\frac{\partial \boldsymbol{g}}{\partial \boldsymbol{b}} = \Sigma V^T \frac{\partial^2 L}{\partial \boldsymbol{G}_\rho \partial \boldsymbol{b}} \tag{4.33}$$

$$= \Sigma V^T \frac{\partial^2 L}{\partial \boldsymbol{G}_\rho^2} \frac{\partial \boldsymbol{G}_\rho}{\partial \boldsymbol{\rho}} \frac{\partial \boldsymbol{\rho}}{\partial \boldsymbol{b}}, \tag{4.34}$$

$$\frac{\partial \boldsymbol{\rho}}{\partial \boldsymbol{b}} = \mathrm{diag}\{\boldsymbol{\rho}\} U. \tag{4.35}$$

thus

$$\frac{\partial \boldsymbol{g}}{\partial \boldsymbol{b}} = \Sigma V^T \frac{\partial^2 L}{\partial \boldsymbol{G}_\rho^2} V \Sigma U^T \mathrm{diag}\{\rho\} U \tag{4.36}$$

$$= MT, \tag{4.37}$$

where $M \equiv \Sigma V^T \frac{\partial^2 L}{\partial \boldsymbol{G}_\rho^2} V \Sigma$ and $T \equiv U^T \mathrm{diag}\{\rho\} U$. When we solve

$$(\alpha I + MT)\delta \boldsymbol{b} = -\alpha \boldsymbol{b} - \boldsymbol{g} \tag{4.38}$$

by the iteration, we can solve Eq. (4.15). We note that the degrees of freedom of Eq. (4.38) is N_τ and the numerical cost to solve is much reduced.

The uniqueness of the solution of Eq. (4.38) is proved in Ref. [49]. The uniqueness is guaranteed when the Hessian $H = \alpha I + MT$ is nonzero and satisfies

$$\sum_{l,l'=1}^{N_\omega} z_l H_{ll'} z_{l'} = \sum_{l,l'=1}^{N_\omega} z_l \frac{\partial^2 (\alpha S - L)}{\partial \rho_l \partial \rho_{l'}} z_{l'} < 0, \tag{4.39}$$

with a real vector $\boldsymbol{z} = (z_1, \cdots, z_{N_\omega})$. By differentiating S with respect to ρ_l and $\rho_{l'}$, and taking the inner products, we find

$$\sum_{l,l'=1}^{N_\omega} z_l \frac{\partial^2 (\alpha S)}{\partial \rho_l \partial \rho_{l'}} z_{l'} = -\alpha \frac{z_l^2}{\rho_l} < 0. \tag{4.40}$$

Next, we introduce the unitary matrix R diagonalizing the covariance matrix C, $T^{-1} C R = \mathrm{diag}[\bar{\sigma}_i^2]$. Taking the transformations,

$$K \to \bar{K} = R^{-1} K, D \to \bar{D} = R^{-1} D, \tag{4.41}$$

we have

$$L = \frac{1}{2} \sum_{i=1}^{N} \left(\bar{D}_i - \sum_{l=1}^{N_\omega} \bar{K}_{il} \rho_l \right)^2 / \bar{\sigma}_i^2. \tag{4.42}$$

By differentiating Eq. (4.42) with respect to ρ_l and taking the inner products, we find

$$\sum_{l,l'=1}^{N_\omega} z_l \frac{\partial^2(-L)}{\partial\rho_l \partial\rho_{l'}} z_{l'} = -\sum_{i=1}^{N} \frac{\bar{z}_i^2}{\bar{\sigma}_i^2} \leq 0, \tag{4.43}$$

$$\bar{z}_i = \sum_{l=1}^{N_\omega} \bar{K}_{il} z_l. \tag{4.44}$$

From Eqs. (4.39), (4.40) and (4.43), we find the uniqueness of the solution of Eq. (4.38) is guaranteed.

Chapter 5

Hydrodynamics and Spectral functions

The transport properties of quark gluon plasma (QGP) attract much attention for a few decades. The results of relativistic heavy ion collisions, such as the elliptic flow of the particles emitted from hot matter [71, 72], suggest that the time revolution of the hot QCD matter near and above the critical temperature (T_c) can be well described by hydrodynamics. Transport coefficients of the conserved charges are the important parameters for hydrodynamics.

Recently the D meson elliptic flow at heavy ion collisions attracts the interest. The strength of the D meson elliptic flow observed at LHC energy is comparable to the strength of the charged-particle anisotropic flow [73, 74]. This suggests that the time evolution of charm quarks created in the early stage of heavy ion collision reach local equilibrium rapidly and thermal charm quarks in QGP are described by hydrodynamics. The transport coefficients of heavy quark, the parameter of the hydrodynamics, is an important information to understand the relatively strong anisotropic flow of heavy quarks.

The non-perturbative effect of QCD plays an important role in this region. The lattice numerical simulation is a powerful method to access such a non-perturbative region of QCD. First measurement of the shear viscosity, the transport coefficient of the energy-momentum tensor, on the lattice have been attempted by F. Karsch and H. W. Wyld in Ref. [63]. They have discussed the framework for a calculation of transport coefficient on the lattice. There is a big difficulty to measure the transport coefficients on the lattice. It is called ill-posed problem. Only Euclidean correlators are the measurable quantities in the lattice simulation. However, we need an information in Minkowski space to access the transport properties. Because of the limitation of the computational power and the fact that the fluctuation of the correlator of the energy-momentum tensor is large, the measurement of the shear viscosity on the lattice is still a ongoing subject in this field.

In the 2000s, the measurement of the transport coefficients, such as the shear viscosity [67, 68, 78], the electrical conductivity [79–84] and the heavy quark diffusion coefficients [85–89] , have been studied actively. In these works, they have tried to extract the transport coefficient from the lattice correlator using Kubo formula.

In this chapter, we give a review of the measurement of the transport coefficients on the lattice. First we show you the derivation of Kubo formula for a quark diffusion coefficient. After that we review the recent works which measure the quark diffusion coefficients.

5.1 Hydro structure of the spectral function

5.1.1 Diffusion equation

Let us first discuss the diffusion equation and its generalized version called the Maxwell-Cattaneo equation. We consider a conserved current $J_\mu(t, \boldsymbol{x})$ defined by a macroscopic

average in a slowly varying system near equilibrium. Because of the current conservation, $J_\mu(t, \boldsymbol{x})$ satisfies the continuity equation,

$$\frac{\partial}{\partial t} J_0(t, \boldsymbol{x}) + \nabla \cdot \boldsymbol{J}(t, \boldsymbol{x}) = 0. \tag{5.1}$$

For slowly varying system, a constitutive equation called the Fick's law,

$$\boldsymbol{J}(t, \boldsymbol{x}) = -D \nabla J_0(t, \boldsymbol{x}), \tag{5.2}$$

is a good phenomenological approximation, where D is the diffusion coefficient. Substituting Eq. (5.2) into Eq. (5.1), we obtain the diffusion equation

$$\frac{\partial}{\partial t} J_0(t, \boldsymbol{x}) = D \nabla^2 J_0(t, \boldsymbol{x}). \tag{5.3}$$

While Eq. (5.2) represents an instantaneous response of the current $\boldsymbol{J}(t, \boldsymbol{x})$ against the change of $J_0(t, \boldsymbol{x})$, in real systems the response generally takes place with a finite time delay. When this delay is not negligible, Eq. (5.2) has to be modified. The simplest extension is

$$\tau_{\mathrm{R}} \frac{\partial}{\partial t} \boldsymbol{J}(t, \boldsymbol{x}) = -D \nabla J_0(t, \boldsymbol{x}) - \boldsymbol{J}(t, \boldsymbol{x}), \tag{5.4}$$

which means that $\boldsymbol{J}(t, \boldsymbol{x})$ relaxes toward the solution of Eq. (5.2) with a time scale τ_{R} called the relaxation time. Substituting Eq. (5.4) into Eq. (5.1), we obtain

$$\left(\tau_{\mathrm{R}} \frac{\partial^2}{\partial t^2} + \frac{\partial}{\partial t} \right) J_0(t, \boldsymbol{x}) = D \nabla^2 J_0(t, \boldsymbol{x}). \tag{5.5}$$

Equation (5.5) is called Maxwell-Cattaneo equation. By taking the small τ_{R} limit of Eq. (5.5), Eq. (5.3) is recovered. It is known that the introduction of τ_{R} can eliminate the acausal behavior of Eq. (5.3), and thus plays a crucial role in relativistic systems [36]. The relaxation time is also known to be important in the diffusion of heavy quarks, because τ_{R} of heavy quarks is proportional to the quark mass in the heavy quark limit [76, 86].

Equation (5.3) has a single solution for a given momentum $\boldsymbol{p}$. By writing the t dependence of a mode with momentum $\boldsymbol{p}$ as $\exp(-i\omega t + i\boldsymbol{k} \cdot \boldsymbol{p})$, the solution of Eq. (5.3) has $\omega = -iDp^2$ with $p = |\boldsymbol{p}|$. On the other hand, Eq. (5.5) has two solutions with

$$\omega = \lambda_\pm \equiv -i \frac{1 \pm \sqrt{1 - 4\tau_R D p^2}}{2\tau_R}. \tag{5.6}$$

In the $p \to 0$ limit, $\lambda_\pm$ behave as

$$\lambda_+ \to -i(\tau_R^{-1} - Dp^2), \quad \lambda_- \to -iDp^2. \tag{5.7}$$

The mode with $\omega = \lambda_-$ corresponds to the solution of Eq. (5.3), which becomes arbitrary slow in this limit.

With the initial condition

$$J_0(t = 0, \boldsymbol{x}) = A e^{i\boldsymbol{p} \cdot \boldsymbol{x}}, \tag{5.8}$$

the solution of Eq. (5.3) is given by

$$J_0(t, \boldsymbol{x}) = A e^{i\boldsymbol{p} \cdot \boldsymbol{x}} e^{-Dp^2 t}. \tag{5.9}$$

By further assuming $\partial J_0(t,\boldsymbol{x})/\partial t = 0$ at $t = 0$, the solution of Eq. (5.5) reads

$$J_0(t,\boldsymbol{x}) = Ae^{i\boldsymbol{p}\cdot\boldsymbol{x}}\left[B_- e^{-i\lambda_- t} + B_+ e^{-i\lambda_+ t}\right], \tag{5.10}$$

with $B_\pm = \mp\lambda_\mp/(\lambda_+ - \lambda_-)$. In the $p \to 0$ limit we have

$$B_- \to 1 + \tau_{\rm R} D p^2, \quad B_+ \to -\tau_{\rm R} D p^2. \tag{5.11}$$

For later convenience, we introduce the Fourier-Laplace transform of Eq. (5.10)

$$\tilde{J}_0(z,\boldsymbol{p}) = \int d\boldsymbol{x} e^{-i\boldsymbol{p}\cdot\boldsymbol{x}} \int_0^\infty dt e^{izt}\left[J_0(t,\boldsymbol{x}) - \bar{J}_0\right], \tag{5.12}$$

where we subtract the average $\bar{J}_0 = (1/V)\int d\boldsymbol{x} J_0(t,\boldsymbol{x})$. Here, the imaginary part of z should be positive for the convergence of the t-integral. Substituting Eq. (5.10) into Eq. (5.12), one obtains

$$\begin{aligned}\tilde{J}_0(z,\boldsymbol{p}) &= -H\left(\frac{B_-}{iz - i\lambda_-} + \frac{B_+}{iz - i\lambda_+}\right) \\ &= H\frac{1 - i\tau_{\rm R} z}{-\tau_{\rm R} z^2 - iz + Dp^2}.\end{aligned} \tag{5.13}$$

5.1.2 Linear response

We next see what we can know about the structure of the spectral function when we assume the diffusion equation can describe the relaxation process of the quark number density. For this purpose, now we consider quantum statistical mechanics and discuss the time evolution of a conserved current in the linear response theory.

Let us consider a response of a system with respect to infinitesimal external perturbation described by Hamiltonian

$$\delta\mathcal{H}(t) = -\int d\boldsymbol{x} h(t,\boldsymbol{x}) j_0(t,\boldsymbol{x}), \tag{5.14}$$

with a conserved current operator $j_\nu(t,\boldsymbol{x})$ and a classical field $h(t,\boldsymbol{x})$. The deviation of the expectation value of $j_\mu(t,\boldsymbol{x})$ from the equilibrium value is then given by [114]

$$\begin{aligned}\delta\langle j_\mu(t,\boldsymbol{x})\rangle &= \langle j_\mu(t,\boldsymbol{x})\rangle - \langle j_\mu(t,\boldsymbol{x})\rangle_{\rm eq} \\ &= -i\int_{-\infty}^{t} dt' \langle[j_\mu(t,\boldsymbol{x}), \delta\mathcal{H}(t')]\rangle_{\rm eq}, \\ &= \int_{-\infty}^{\infty} dt' \int d\boldsymbol{x}' h(t',\boldsymbol{x}') G^{\rm R}_{\mu 0}(t-t', \boldsymbol{x}-\boldsymbol{x}'),\end{aligned} \tag{5.15}$$

with the retarded propagator defined by

$$\begin{aligned}G^{\rm R}_{\mu\nu}(t-t',\boldsymbol{x}-\boldsymbol{x}') &= i\theta(t-t')\langle[j_\mu(t,\boldsymbol{x}), j_\nu(t',\boldsymbol{x}')]\rangle_{\rm eq} \\ &= \int\frac{d\omega}{2\pi}\int\frac{d\boldsymbol{p}}{(2\pi)^3} G^{\rm R}_{\mu\nu}(\omega,\boldsymbol{p}) e^{i(\boldsymbol{p}\cdot(\boldsymbol{x}-\boldsymbol{x}') - \omega(t-t'))},\end{aligned} \tag{5.16}$$

where the expectation value $\langle\cdot\rangle_{\rm eq}$ is taken for thermal ensemble. The spectral function of the current is given by

$$\rho_{\mu\nu}(\omega,\boldsymbol{p}) = \frac{1}{\pi}{\rm Im} G^{\rm R}_{\mu\nu}(\omega + i\varepsilon, \boldsymbol{p}). \tag{5.17}$$

We now suppose that the external field $h(t, \boldsymbol{x})$ in Eq. (5.14) is adiabatically applied at $t = -\infty$ and suddenly turned off at $t = 0$ as

$$h(t, \boldsymbol{x}) = he^{i\boldsymbol{p}\cdot\boldsymbol{x}}e^{\varepsilon t}\theta(-t), \tag{5.18}$$

with an infinitesimal positive number ε and small momentum $\boldsymbol{p}$.

We now suppose that the external perturbation is applied to the system with an infinitesimal number $\varepsilon > 0$, i.e. the external field with momentum $\boldsymbol{p}$ is turned on adiabatically from $t = -\infty$ and turned off suddenly at $t = 0$.

Just before $t = 0$, the system should be in a local equilibrium state with an expectation value

$$\lim_{t\to 0^-} \delta\langle j_0(t, \boldsymbol{x})\rangle = h\chi(p)e^{i\boldsymbol{p}\cdot\boldsymbol{x}}, \tag{5.19}$$

where $\chi(p)$ is the momentum-dependent susceptibility: With $p = 0$, $\chi(p)$ is the susceptibility of the conserved charge defined by $\chi(0) = \chi = \partial\langle j_0(t, \boldsymbol{x})\rangle/\partial\mu$ [116] with chemical potential μ.

After the external force is turned off at $t = 0$, the system start to relax toward the equilibrium value. When p is sufficiently small, this process should be well described by the diffusion equation Eq. (5.3) or (5.5) with an initial condition Eq. (5.19). Since the system is static at $t = 0$, it would be reasonable to further assume that $\langle j_i(t, \boldsymbol{x})\rangle$ is zero at $t = 0$ and becomes nonzero continuously. From Eq. (5.1), we then have $\partial\langle j_0(0, \boldsymbol{x})\rangle/\partial t = 0$ for the initial condition. Therefore, $\langle j_0(t, \boldsymbol{x})\rangle$ for $t > 0$ should be given by Eq. (5.10) with [90]

$$H = h\chi(p). \tag{5.20}$$

On the other hand, the current $\langle j_0(t, \boldsymbol{x})\rangle$ with the perturbation Eqs. (5.14) and (5.18) is given by Eq. (5.15). The Fourier-Laplace transform of $\delta\langle j_0(t, \boldsymbol{x})\rangle$ in Eq. (5.15) for $t > 0$ is given by

$$\begin{aligned}
\tilde{j}_0(z, \boldsymbol{p}) &= e^{-i\boldsymbol{p}\cdot\boldsymbol{x}} \int_0^\infty dt e^{izt} \delta\langle j_0(t, \boldsymbol{x})\rangle \\
&= e^{-i\boldsymbol{p}\cdot\boldsymbol{x}} \int_0^\infty dt e^{izt} \int dt' \int d\boldsymbol{x}' \quad h(t', \boldsymbol{x}')G^{\mathrm{R}}_{00}(t - t', \boldsymbol{x} - \boldsymbol{x}') \\
&= h \int_0^\infty dt e^{izt} \int_{-\infty}^0 dt' \int \frac{d\omega}{2\pi} G^{\mathrm{R}}_{00}(\omega, \boldsymbol{p}) e^{\varepsilon t' - i\omega(t-t')} \\
&= -\int \frac{d\omega}{2\pi} \frac{h}{(\omega - z)(\omega - i\varepsilon)} G^{\mathrm{R}}_{00}(\omega, \boldsymbol{p}),
\end{aligned} \tag{5.21}$$

where in the third equality we used Eq. (5.18). Using the analyticity of $G^{\mathrm{R}}_{00}(\omega, \boldsymbol{p})$ in the upper-half complex-energy plane, the ω integral in Eq. (5.21) is closed in the upper-half plane and is replaced by the contributions of two poles at $\omega = z$ and $i\varepsilon$ as

$$\tilde{j}(z, \boldsymbol{p}) = -ih\frac{G^{\mathrm{R}}_{00}(z, \boldsymbol{p}) - G^{\mathrm{R}}_{00}(0, \boldsymbol{p})}{z}. \tag{5.22}$$

Putting $z = \omega + i\varepsilon$, and taking the real part of both sides, we find,

$$\begin{aligned}
\frac{\mathrm{Re}\tilde{j}_0(\omega + i\varepsilon, \boldsymbol{p})}{h} &= \frac{\mathrm{Im}G^{\mathrm{R}}_{00}(\omega, \boldsymbol{p}) - \mathrm{Im}G^{\mathrm{R}}_{00}(0, \boldsymbol{p})}{\omega} \\
&= \pi\frac{\rho_{00}(\omega, \boldsymbol{p})}{\omega},
\end{aligned} \tag{5.23}$$

where we used Eq. (5.17) and $\rho_{00}(0,\boldsymbol{p}) = 0$ in the last equality. Comparing Eqs. (5.13), (5.20) and (5.23), we obtain [90]

$$\frac{\rho_{00}^{\rm hydro}(\omega,\boldsymbol{p})}{\omega} = \frac{1}{\pi}\frac{\chi(p)Dp^2}{\omega^2 + (Dp^2 - \tau_{\rm R}\omega^2)^2}. \tag{5.24}$$

Here, we represent the spectral function as $\rho_{00}^{\rm hydro}(\omega,\boldsymbol{p})$ because this result is valid only for low energy and low momentum at which the time evolution of $\langle j_0(t,\boldsymbol{x})\rangle$ is well described by Eq. (5.5). For large ω and/or p, $\rho_{00}(\omega,\boldsymbol{p})$ can deviate from this hydrodynamic behavior. Thus, $\rho_{00}(\omega,\boldsymbol{p})$ is generally represented as

$$\rho_{00}(\omega,\boldsymbol{p}) = \rho_{00}^{\rm hydro}(\omega,\boldsymbol{p}) + \rho_{00}^{\rm high}(\omega,\boldsymbol{p}), \tag{5.25}$$

where $\rho_{00}^{\rm high}(\omega,\boldsymbol{p})$ represents the contribution which is not included in $\rho_{00}^{\rm hydro}(\omega,\boldsymbol{p})$. For example, the spectral function of quark current has a continuum contribution for $\omega \gtrsim \sqrt{(2m_q)^2 + p^2}$ with the quark mass m_q. If bound states of quarkonia exist in vector channel, the corresponding peaks also appear. These structures are encoded in $\rho_{00}^{\rm high}(\omega,\boldsymbol{p})$.

From the conservation law, the total charge $Q(t) = \int_V d\boldsymbol{x} j_0(t,\boldsymbol{x})$ is conserved and satisfies $(d/dt)Q(t) = 0$. Moreover the linear response relation connects the susceptibility χ with the fluctuation of $Q(t)$ as $\chi = \langle \delta Q(t)^2\rangle/(TV)$ [116]. From these conditions at zero momentum one obtains

$$\frac{\rho_{00}(\omega,0)}{\omega} = \chi\delta(\omega). \tag{5.26}$$

By taking the $p \to 0$ limit of Eq. (5.24), we see that $\rho_{00}^{\rm hydro}(\omega,0)$ satisfies Eq. (5.26).

5.2 Kubo formula

From the continuity equation Eq. (5.1), we obtain

$$\omega\rho_{00}(\omega,\boldsymbol{p}) = -p_i\rho_{0i}(\omega,\boldsymbol{p}), \tag{5.27}$$
$$\omega\rho_{i0}(\omega,\boldsymbol{p}) = -p_j\rho_{ij}(\omega,\boldsymbol{p}), \tag{5.28}$$
$$\omega^2\rho_{00}(\omega,\boldsymbol{p}) = p_ip_j\rho_{ij}(\omega,\boldsymbol{p}), \tag{5.29}$$

where $i,j = 1,2,3$ and the sums over recursive i and j are taken. Eq. (5.29) is rewritten as

$$\omega^2\rho_{00}(\omega,\boldsymbol{p}) = p^2\rho_{\rm L}(\omega,p), \tag{5.30}$$

with the longitudinal part

$$\rho_{\rm L}(\omega,p) = \frac{p_ip_j}{p^2}\rho_{ij}(\omega,\boldsymbol{p}). \tag{5.31}$$

Similarly to Eq. (5.25), $\rho_{\mu\nu}(\omega,\boldsymbol{p})$ and $\rho_{\rm L}(\omega,\boldsymbol{p})$ are decomposed into hydrodynamic and high-energy parts, which are connected with each other through Eqs. (5.27) – (5.29) and (5.30). From rotational symmetry, $\rho_{00}(\omega,\boldsymbol{p})$ and $\rho_{\rm L}(\omega,\boldsymbol{p})$ depend on $\boldsymbol{p}$ only through p^2.

From Eqs. (5.30) and (5.24), we obtain

$$\frac{\rho_{\rm L}^{\rm hydro}(\omega,p)}{\omega} = \frac{\chi(p)}{\pi}\frac{D\omega^2}{\omega^2 + (Dp^2 - \tau_{\rm R}\omega^2)^2}. \tag{5.32}$$

This form leads to the Kubo formula for the diffusion coefficient

$$D = \frac{\pi}{\chi} \lim_{\omega\to 0} \lim_{p\to 0} \frac{\rho_{\mathrm{L}}(\omega, p)}{\omega} = \frac{1}{3}\frac{\pi}{\chi} \lim_{\omega\to 0} \frac{\rho_{ii}(\omega, 0)}{\omega}, \tag{5.33}$$

where the small ω limit has to be taken after small p limit. This type Kubo formula is used in the many works studying transport coefficients on the lattice, such as the shear viscosity and the electrical conductivity. Eq. (5.33) is the Kubo formula for a quark diffusion coefficient. Kubo formula for other conserved quantities can be obtain by the same derivations, see e.g. [90, 114].

Chapter 6

Observables and Methodology

In this chapter we show the observables studied in this thesis and the methodologies of the measurements. The observables which we have studied are classified into the two topics:

1. Study the dispersion relation and momentum dependence of the strength of the peak of the spectral function of charmonium at the finite temperature from the spectral functions reconstructed by MEM discussed in Chap. 4.

2. Study the charm quark diffusion coefficient from the lattice Euclidean correlators on the basis of the linear response theory discussed in Chap. 5.

The information of these quantities can be extracted from the charmonium correlation functions

$$G^{lm}(\tau, \boldsymbol{p}) = \int d^3x e^{i\boldsymbol{p}\cdot\boldsymbol{x}} \left\langle J^l(\tau, \boldsymbol{x}) J^{m\dagger}(0,0) \right\rangle, \tag{6.1}$$

where the imaginary time τ is restricted to the interval $0 \leq \tau < 1/T$ and $J^l(\tau, \boldsymbol{x}) = \bar{c}(\tau, \boldsymbol{x}) i\gamma^l c(\tau, \boldsymbol{x})$ is the local interpolating operator in the Heisenberg representation with the charm quark field $c(\tau, \boldsymbol{x})$ with $l = 0, 1, 2$, and 3 for the vector channel and $l = 5$ for the pseudoscalar channel.

This chapter is organized as follows. In Sec. 6.1 we introduce the definitions for the dispersion relation and momentum dependence of the strength of the peak of the spectral function using MEM. In Sec. 6.2 we derive an inequality for the quark diffusion coefficient by differentiating the temporal Euclidean correlator with respect to momentum. The common lattice set up for these studies is shown in Sec. 6.3.

6.1 Dynamical property of charmonia at the finite temperature

In this section we show how we analyze the momentum dependence of the spectral weight of the J/ψ and η_c as an application of MEM discussed in Chap. 4. To study these quantities with error estimates in MEM, we represent $E(p)$ and Z in Eq. (3.36) in the form in Eq. (4.10).

For such a quantity corresponding to the residue Z, we consider

$$\bar{Z}(p) = \int_I d\omega 2\omega \rho(\omega, p), \tag{6.2}$$

for a peak in a spectral function $\rho(\omega, p)$, where I is the interval of ω which covers the peak structure. By substituting Eq. (3.36) into Eq. (6.2) one easily finds that for the delta function Eq. (3.36) we have $\bar{Z}(p) = Z$. When the interval I does not include other structures in $\rho(\omega)$, therefore, $\bar{Z}(p)$ corresponds to Z. Note that $\bar{Z}(p)$ defined by Eq. (6.2) is meaningful only for well isolated peaks for which such a choice of I is possible. Since

Eq. (6.2) has the form given in Eq. (4.10), $\bar{Z}(p)$ is a quantity which can be estimated in MEM with error.

Next, to analyze the dispersion relation in MEM, we consider the center of the weight of a peak of the dimensionless spectrum $\rho(\omega)/\omega^2$, which is given by

$$\bar{E}(p) = \frac{\int_I d\omega\omega(\rho(\omega,p)/\omega^2)}{\int_I d\omega(\rho(\omega,p)/\omega^2)}. \tag{6.3}$$

By substituting Eq. (3.36) into Eq. (6.3), it is again checked that $\bar{E}(p) = E(p)$ for this case. In practical analyses, we calculate Eq. (6.3) as

$$\bar{E}(p) = \frac{\langle\!\langle \int_I d\omega\omega(\rho(\omega,p)/\omega^2)\rangle\!\rangle}{\langle\!\langle \int_I d\omega(\rho(\omega,p)/\omega^2)\rangle\!\rangle}, \tag{6.4}$$

in order to perform the analysis with the saddle point approximation for $P(A,\alpha)$ [49]. In the error analysis for Eq. (6.4), we take account of the correlation between the numerator and denominator using the general formula of error propagation. Because the numerator and denominator are positively correlated, the inclusion of this correlation leads to the suppression of the error of Eq. (6.4).

In the above discussions, the definitions of $\bar{Z}(p)$ and $\bar{E}(p)$ depend on the energy interval I. Because the choice of the interval has an arbitrariness, in the analyses of these quantities one has to check the dependence of $\bar{Z}(p)$ and $\bar{E}(p)$ on the interval I by varying it in a moderate range. This analysis will be performed in Sec. 7.4. As we will see there, the peaks corresponding to the J/ψ and η_c analyzed in this study are well isolated and our results on $\bar{Z}(p)$, $\bar{E}(p)$, and their errors are insensitive to the choice of I. We will show the numerical results in Chap. 7.

6.2 Diffusion coefficient of the charm quark

In this section, we discuss the relation between the temporal Euclidean correlator and the transport coefficients, D and $\tau_{\rm R}$, on the basis of the discussion in Chap. 5. We will obtain two inequalities which constrain the coefficients in the D–$\tau_{\rm R}$ plane with the momentum dependence of the temporal Euclidean correlator.

As we mentioned in Sec. 5.2, extracting the transport coefficient from $G_{ii}(\tau,0)$ using Kubo formula is a hard work because of the insensitivity of $G_{ii}(\tau,0)$ to the low energy structure of the spectral function. Therefore, we have focused on the temporal Euclidean correlator with finite momentum $G_{00}(\tau,\boldsymbol{p})$ to extract the information on the transport coefficient. From Eq. (5.29) we can see that the high energy part of $\rho_{00}(\omega,\boldsymbol{p})$ is suppressed by the factor p^2/ω^2 comparing with $\rho_{ii}(\omega,\boldsymbol{p})$. This suggests that $G_{00}(\tau,\boldsymbol{p})$ may be more advantageous to extract the information on the low energy structure of the spectral function than $G_{ii}(\tau,\boldsymbol{p})$.

For simplicity of notation we introduce the following: $\tilde{p} \equiv p/T$ is dimensionless momentum in the unit of the temperature. $\partial_{\tilde{p}^2} \equiv \frac{\partial}{\partial\tilde{p}^2}$ is a differential operator with respect to $\tilde{p}^2$. The quantity which depends on momentum $O(p^2)$ without the argument p^2 is understood as an abbreviation of the limit of the function $O \equiv \lim_{p^2\to 0} O(p)$.

6.2.1 Euclidean correlator and mid-point expansion

The current-current Euclidean correlator Eq. (6.1) with $l,m = 0,\ 1,\ 2$, and 3 is relevant to the charm quark diffusion coefficient. Since $\rho_{\mu\nu}(\omega,\boldsymbol{p})$ with $\mu = \nu$ are odd functions of ω, $G^{\mu\mu}(\tau,\boldsymbol{x})$ and the spectral function $\rho^{\mu\mu}(\omega,\boldsymbol{p})$ are connected by Eq. (3.32) and this

relation can be rewritten as

$$G_{\mu\mu}(\tau,\boldsymbol{p}) = \int_0^\infty \frac{\cosh\left((\tau-\tau_{\rm mid})\,\omega\right)}{\sinh\left(\frac{\omega}{2T}\right)}\rho_{\mu\mu}(\omega,\boldsymbol{p})d\omega, \tag{6.5}$$

where no sum over μ is taken and $\tau_{\rm mid} = 1/(2T)$.

In almost all previous studies on transport coefficients on the lattice, the analysis is performed by the following two steps: (1) The spatial channel $\rho_{ii}(\omega,0)$ is analyzed from $G_{ii}(\tau,0)$ with Eq. (6.5), and (2) the transport coefficient is obtained by the Kubo formula Eq. (5.33) from $\rho_{ii}(\omega,0)$. In this approach, however, the first step has a fundamental difficulty because one has to determine the continuous function $\rho_{ii}(\omega,0)$ from discrete data on $G_{ii}(\tau,0)$ obtained numerically. One thus has to introduce an ansatz or resort to Bayesian analysis in this step. The estimate of the systematic error associated with these treatments, however, is difficult. In particular, the Euclidean correlator $G_{ii}(\tau,0)$ is insensitive to low energy structure of $\rho_{ii}(\omega,0)$, and this makes the analysis of D difficult.

In this study, we focus on the momentum dependence of the correlator in temporal channel $G_{00}(\tau,\boldsymbol{p})$. From Eqs. (5.26) and (6.5) one finds that $G_{00}(\tau,\boldsymbol{p})$ at zero momentum is a constant, $G_{00}(\tau,0) = \chi T$, and does not contain information on transport coefficients. For nonzero p, on the other hand, $G_{00}(\tau,\boldsymbol{p})$ has τ dependence reflecting dynamics of the system. From Eq. (5.30), one sees that $\rho_{00}(\omega,\boldsymbol{p})$ is proportional to $\omega^{-2}\rho_{\rm L}(\omega,p)$. Therefore, the low-energy part of the spectral property is more strongly reflected in $G_{00}(\tau,\boldsymbol{p})$ than spatial channels $G_{ii}(\tau,\boldsymbol{p})$. The purpose of the present study is to take this advantage of $G_{00}(\tau,\boldsymbol{p})$. Another motivation of this strategy is the use of $\rho^{\rm hydro}_{\mu\nu}(\omega,\boldsymbol{p})$ with nonzero ω and p. Compared with the standard method with Eq. (5.33) which focuses only on the spectral function with $p = 0$, our method can make use of the property of $\rho^{\rm hydro}_{\mu\nu}(\omega,\boldsymbol{p})$ with nonzero p.

From Eq. (6.5) one finds that $G_{00}(\tau,\boldsymbol{p})$ at the midpoint $\tau = \tau_{\rm mid}$ is the most sensitive to low energy structure of $\rho_{00}(\omega,\boldsymbol{p})$. In the following, we thus focus on the behavior of $G_{00}(\tau,\boldsymbol{p})$ around $\tau = \tau_{\rm mid}$, and consider the Taylor expansion of $G_{00}(\tau,\boldsymbol{p})$ at $\tau = \tau_{\rm mid}$ given by

$$G_{00}(\tau,\boldsymbol{p}) = \sum_n \frac{1}{n!}M_n(p)(\tau T - \tau_{\rm mid}T)^n. \tag{6.6}$$

Using Eq. (6.5) the coefficients $M_n(p)$ are related to the spectral function as

$$M_n(p) = \left.\frac{d^n G_{00}(\tau,\boldsymbol{p})}{d(\tau T)^n}\right|_{\tau=\tau_{\rm mid}} \tag{6.7}$$

$$= \frac{1}{2}\int_{-\infty}^{\infty} d\omega \left(\frac{\omega}{T}\right)^n \frac{\rho_{00}(\omega,\boldsymbol{p})}{\sinh(\omega/2T)}, \tag{6.8}$$

which shows that the coefficients of the Taylor expansion $M_n(p)$ are the moments of $\rho_{00}(\omega,\boldsymbol{p})/\sinh(\omega/2T)$. Because $\rho_{00}(\omega,\boldsymbol{p})$ is an odd function of ω, $M_n(p)$ vanishes for odd n. It is noteworthy that the moments $M_n(p)$ are observables which can be measured directly in Euclidean space. Because $M_n(p)$ are linear in $\rho_{00}(\omega,\boldsymbol{p})$, they are decomposed into hydrodynamic and high-energy parts as

$$M_n(p) = M_n^{\rm hydro}(p) + M_n^{\rm high}(p), \tag{6.9}$$

in accordance with the decomposition Eq. (5.25).

From Eq. (5.26), at $p = 0$ one obtains

$$M_0(0) = \chi T, \tag{6.10}$$

$$M_n(0) = 0 \qquad \text{for } n \geq 1. \tag{6.11}$$

Equations (6.10) and (6.11) shows that the moment at zero momentum, $M_n(0)$, do not have information on transport coefficients. In the following, we thus focus on the momentum derivatives of $M_n(p)$, especially those of two lowest order ones with $n = 0$ and 2. Because $M_n(p)$ are even functions of p, their second derivatives are lowest nonzero ones.

6.2.2 Inequalities

We now introduce crucial assumptions on the structure of the spectral function. First, we assume that the high energy part $\rho_{\rm L}^{\rm high}(\omega, 0)$ is solely positive semi-definite, i.e.

$$\rho_{\rm L}^{\rm high}(\omega, 0) \geq 0 \qquad \text{for } \omega > 0. \tag{6.12}$$

Although $\rho_{\rm L}(\omega, \boldsymbol{p}) \geq 0$ is generally satisfied as discussed in the previous section, the condition Eq. (6.12) is not satisfied. This condition, however, should be satisfied when the ranges of ω at which hydrodynamic and high-energy parts take large values are well separated. This is the case, for example, for heavy quark current with quark mass m_q, because in this case $\rho_{\rm L}^{\rm high}(\omega, 0)$ becomes nonzero for $\omega \gtrsim 2m_q$, while the strength of $\rho_{\rm L}^{\rm hydro}(\omega, 0)$ is concentrated around $\omega \lesssim \tau_{\rm R}^{-1}$. Since $\tau_{\rm R}^{-1} \sim m_q^{-1}$ becomes smaller as m_q increases, the separation between $\rho_{\rm L}^{\rm hydro}(\omega, 0)$ and $\rho_{\rm L}^{\rm high}(\omega, 0)$ becomes more prominent as m_q becomes larger. In this case, one thus can safely assume Eq. (6.12). Second, we assume that $\rho_{00}^{\rm high}(\omega, \boldsymbol{p})$ is analytic. Although $\rho_{00}(\omega, \boldsymbol{p})$ is not analytic at the origin, it is assumed that this singularity is attributed to $\rho_{00}^{\rm hydro}(\omega, \boldsymbol{p})$. Finally, it is assumed that $\chi(p)$ is analytic at $p = 0$ and thus can be expanded by p^2.

Once we accept these conditions, by taking p^2 derivative of $M_n^{\rm high}(p)$ and the small momentum limit we obtain

$$\partial_{\tilde{p}^2} M_n^{\rm high} = \int d\omega \left(\frac{\omega}{T}\right)^{n-2} \frac{\rho_{\rm L}^{\rm high}(\omega, 0)}{\sinh(\omega/2T)} \geq 0, \tag{6.13}$$

where Eqs. (6.8) and (5.30) are used. Substituting this inequality into Eq. (6.9), we obtain

$$\partial_{\tilde{p}^2} M_n^{\rm hydro} \leq \partial_{\tilde{p}^2} M_n, \tag{6.14}$$

for even n. Eq. (6.14) is the key inequality in the following argument.

Next, we turn our attention to the hydrodynamic part $M_n^{\rm hydro}(p)$. From Eqs. (5.24) and (6.8), the $\tilde{p}^2$ derivative of $M_0^{\rm hydro}(p)$ at $p = 0$ is calculated to be

$$\begin{aligned} \partial_{\tilde{p}^2} M_0^{\rm hydro} &= \lim_{p^2 \to 0} \frac{\partial}{\partial \tilde{p}^2} \int d\omega \frac{\rho_{00}^{\rm hydro}(\omega, \boldsymbol{p})}{\sinh(\omega/2T)} \\ &= h_0(\tilde{\tau}_{\rm R}) M_0 D T + \partial_{\tilde{p}^2} \chi T, \end{aligned} \tag{6.15}$$

where $\tilde{\tau}_{\rm R} = \tau_{\rm R} T$ and

$$h_0(\tilde{\tau}_{\rm R}) = -\frac{\ln 2}{\pi} + \tilde{\tau}_{\rm R} \left\{ 1 - F\left(\frac{1}{\tilde{\tau}_{\rm R}}\right) \right\} \xrightarrow[\tilde{\tau}_{\rm R} \to 0]{} -\frac{\ln 2}{\pi}, \tag{6.16}$$

$$\begin{aligned} F(b) &\equiv \frac{b}{\pi} \int_0^\infty dx \frac{x}{x^2 + 1} \frac{1}{\sinh(bx/2)} \\ &= -1 - \frac{b \ln 2}{\pi} - \frac{b}{\pi} \left[\Psi\left(\frac{b}{4\pi}\right) - \Psi\left(\frac{b}{2\pi}\right) \right], \end{aligned} \tag{6.17}$$

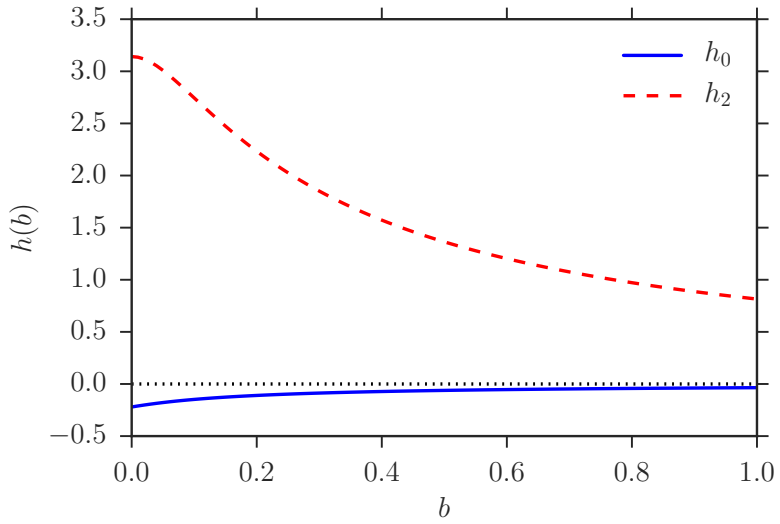

FIGURE 6.1: Behaviors of $h_0(\tilde{\tau}_R)$ and $h_2(\tilde{\tau}_R)$ in Eqs. (6.15) and (6.20) as functions of b.

and $\Psi(z) \equiv \frac{d}{dz}\ln\Gamma(z)$ is the digamma function. The behavior of $h_0(\tilde{\tau}_R)$ is shown in Fig. 6.1. As shown in the figure, $h_0(\tilde{\tau}_R) < 0$ for $b \geq 0$, and $|h_0(\tilde{\tau}_R)|$ is a monotonically decreasing function of b with $|h_0(0)| = \ln 2/\pi$.

Substituting Eq. (6.15) into Eq. (6.14), we find that the diffusion coefficient is constrained from below as

$$DT \geq D_L(\tilde{\tau}_R)T, \tag{6.18}$$

with

$$D_L(\tilde{\tau}_R)T = \frac{1}{h_0(\tilde{\tau}_R)}\left(\frac{\partial_{\tilde{p}^2}M_0}{M_0} - \frac{\partial_{\tilde{p}^2}\chi}{\chi}\right). \tag{6.19}$$

We note that $M_0(0) = \chi(0)T$ is satisfied, but for nonzero momentum $M_0(p)$ and $\chi(p)$ are different quantities.

The same manipulation for $M_2^{\rm hydro}(p)$ leads to

$$\partial_{\tilde{p}^2}M_2^{\rm hydro} = h_2(\tilde{\tau}_R)M_0 DT, \tag{6.20}$$

with

$$h_2(\tilde{\tau}_R) = \frac{1}{\tilde{\tau}_R}F\left(\frac{1}{\tilde{\tau}_R}\right) \xrightarrow[\tilde{\tau}_R\to 0]{} \pi. \tag{6.21}$$

We note that a term proportional to $\partial_{\tilde{p}^2}\chi$ does not appear in Eq. (6.20) unlike Eq. (6.15), because $M_2(0) = 0$. As shown in Fig. 6.1, $h_2(\tilde{\tau}_R)$ is a positive and a monotonically decreasing function with $h_2(0) = \pi$. From Eqs. (6.13) and (6.20), we obtain an upper limit of the diffusion coefficient,

$$DT \leq D_U(\tilde{\tau}_R)T, \tag{6.22}$$

with

$$D_U(\tilde{\tau}_R)T = \frac{1}{h_2(\tilde{\tau}_R)}\frac{\partial_{\tilde{p}^2}M_2}{M_0} \tag{6.23}$$

We note that the directions of inequalities, Eqs. (6.18) and (6.22), are opposite. This is caused by the opposite sign of $h_0(\tilde{\tau}_{\rm R})$ and $h_2(\tilde{\tau}_{\rm R})$.

By combining Eqs. (6.18) and (6.22), we obtain

$$D_{\rm L}(\tilde{\tau}_{\rm R}) \le DT \le D_{\rm U}(\tilde{\tau}_{\rm R}). \tag{6.24}$$

In particular, since $D_{\rm L}(0) \le D_{\rm L}(\tilde{\tau}_{\rm R})$ we have a lower bound of DT as

$$DT \ge D_{\rm L}(0) = -\frac{\pi}{\ln 2}\left(\frac{\partial_{\tilde{p}^2} M_0}{M_0} + \frac{\partial_{\tilde{p}^2}\chi}{\chi}\right), \tag{6.25}$$

irrespective of the value of $\tau_{\rm R}$.

We note that though $\partial_{\tilde{p}^2} M_n/M_0$ can be measured in the lattice simulation, we do not have a method measuring $\partial_{\tilde{p}^2}\chi/\chi$ on the lattice. Therefore, we have measured Eq. (6.24) on the lattice in the case of $\partial_{\tilde{p}^2}\chi \ll \chi$.

6.2.3 Discussions

Remarks on Eq. (6.24) are in order.

First, although we obtained the second inequality Eq. (6.22) from $G_{00}(\tau, \boldsymbol{p})$, one can obtain the same quantity from the spatial channel as

$$\partial_{\tilde{p}^2} M_2 = G_{\rm L}(\tau_{\rm mid}, 0) = \frac{1}{3} G_{ii}(\tau_{\rm mid}, 0). \tag{6.26}$$

Similarly, M_n for $n \ge 4$ can be also constructed from the spatial channel. Only the first inequality Eq. (6.18) is the unique result which can be obtained from $G_{00}(\tau, \boldsymbol{p})$.

Second, it is notable that $D_{\rm L}$ and $D_{\rm U}$ are given by the combination of the ratio $\partial_{\tilde{p}^2} M_n/M_0$ or $\partial_{\tilde{p}^2}\chi/\chi$. In the measurement of $M_n(p)$ (and $\chi(p)$) in lattice simulations, one has to take account of the discretization effect on the wave function renormalization of the operator $j_\mu(\tau, \boldsymbol{x})$. This renormalization coefficient, however, is automatically canceled out in the ratios $\partial_{\tilde{p}^2} M_n/M_0$ (and $\partial_{\tilde{p}^2}\chi/\chi$). The analysis of $D_{\rm L}$ and $D_{\rm U}$ thus can be carried out without the renormalization coefficient. As we will discuss later, this cancellation is one of the advantages to focus on $G_{00}(\tau, \boldsymbol{p})$ in the analysis of $D_{\rm U}$ in place of Eq. (6.26).

Third, the inequality Eq. (6.24) is the strongest one which can be obtained without introducing assumptions on $\rho_{\rm L}^{\rm high}(\omega, 0)$ except for its semi-positivity. For example, one can obtain the similar inequalities by considering Taylor expansion of $G_{00}(\tau, \boldsymbol{p})$ at $\tau \ne \tau_{\rm mid}$. It, however, is easily shown that the inequalities obtained in this way is weaker than Eq. (6.24) with the use of Eq. (6.5). One can also obtain inequalities from $\partial_{\tilde{p}^2} M_n$ for $n \ge 4$. However, these inequalities, which give an upper limit, again are weaker than Eq. (6.22).

Fourth, we comment on the relation between Eq. (6.22) and other studies on transport coefficients. In the recent analyses of transport coefficients with Kubo formula Eq. (5.33), the ansatz for the spectral function in spatial channel,

$$\rho_{ii}(\omega, 0) = \frac{\alpha\omega}{\omega^2 + \gamma^2} + \rho^{\rm cont}(\omega), \tag{6.27}$$

is sometimes employed with α and γ being fitting parameters [83]. Here, $\rho^{\rm cont}(\omega)$ represents the continuum part. Various forms for $\rho^{\rm cont}(\omega)$ are assumed in the literature, but in almost all studies $\rho^{\rm cont}(\omega) > 0$ is satisfied. In this case, the ansatz Eq. (6.27) is completely agrees with our assumption to obtain Eq. (6.22). In other words, the diffusion coefficient obtained with the ansatz Eq. (6.27) satisfies Eq. (6.22). On the other hand, Eq. (6.18) is the relation obtained for the first time by considering the correlator in temporal channel.

Finally, let us give some comments on the origin of terms in Eq. (6.24). In the small p limit, the integral Eq. (6.8) for $n = 0$ is dominated by the contribution of the sharp peak in $\rho_{00}^{\mathrm{hydro}}(\omega, \boldsymbol{p})$, while the contribution of $\rho_{00}^{\mathrm{high}}(\omega, \boldsymbol{p})$ vanishes. From this fact, one may naïvely expect that the contribution of $\rho_{00}^{\mathrm{high}}(\omega, \boldsymbol{p})$ in Eq. (6.18) should vanish. The integral for $M_0(p)$, however, simply gives χ with $p = 0$, and information on the transport coefficients appears only at the order of p^2 of $M_0(p)$. At this order, however, the high energy part also has nonzero contribution. When one considers $\partial_{\tilde{p}^2} M_0$, both contributions have nonzero value. Next, the existence of the τ_{R} dependence in Eq. (6.24) is understood from the solution of Maxwell-Cattaneo equation Eq. (5.10). While the integral Eq. (6.8) is dominated by the lower energy mode with $\omega = \lambda_-$ in the small p limit, overall coefficient of this mode has τ_{R} dependence at the order p^2 as in Eq. (5.11). This τ_{R} dependence is responsible for those in Eq. (6.24).

6.3 Lattice set up

In this section we introduce the brief lattice set up for studies in this thesis. Both of the studies require the non-zero momentum correlators. We have adopted the anisotropic lattice for these studies owing to almost same but slightly different reasons. In the first study, the resolution of the MEM analysis is partially depend on the number of the input data points. In our analysis, the input data points corresponds to the number of the imaginary time slices. Since the temporal extent of the lattice is restricted by the temperature, the naive solution is using the lattice with a small lattice spacing. On the other hand, however, since the momenta of bosons on the lattice is discretized as

$$p_i = \frac{2}{a_\sigma} \sin\left(\frac{\pi \hat{p}_i}{N_\sigma}\right), \tag{6.28}$$

the analysis of momentum dependence of lattice observables with a good resolution requires a large spatial extent. When we adopt a isotropic lattice with a small lattice spacing, the required spatial discretization number N_σ becomes large and the numerical cost become large as N_σ^3 naively. Furthermore, we have to have the correlator with the temperature under T_{c} as the reference of the vacuum contribution. When we perform the simulations with the fixed lattice spacing, the simulation under T_{c} requires larger temporal extent, which corresponds to the inverse of the temperature, than the simulations at high temperature. Therefore, adopting the anisotropic lattice with a temporal lattice spacing smaller than the spatial one is a good solution for these requirements. In the second study, since the inequality for the diffusion coefficient Eq. (6.24) is defined by the derivatives of the observables with respect to momentum, a good momentum resolution is required to define these quantities by the numerical difference of the lattice observables. Since the hydrodynamic picture is valid for the low energy region, the momenta of correlators for the analysis of the transport coefficient should be much smaller than temperature, $p/T << 1$. Therefore, this requirement of a large spatial extent is more crucial than that of the first study. On the other hand, since we are interested in the diffusion coefficient of the charm quark in deconfined phase, the required temporal discretization number N_τ is smaller than that for the first study.

Our simulation is performed on quenched anisotropic lattices with the ratio of spatial and temporal lattice spacings $\xi = a_\sigma/a_\tau = 4$. We use the standard Wilson gauge action Eq. (2.73) and Wilson fermion Eq. (2.74) with $\beta = 7.0$, the spatial hopping parameter $\kappa_\sigma = 0.08285$ and the fermion anisotropy $\gamma_F = 3.476$ [39]. The temporal lattice spacing in physical unit is $a_\tau = 0.00975$ fm, and the critical temperature on this lattice is $T_{\mathrm{c}} = 272(2)$ MeV [39]. Each configuration is separated by 500 sweeps, where one sweep consists of one pseudo heat bath and five over-relaxation updates. We study the temperature dependence by changing the temporal lattice size N_τ with fixed a_τ.

This analysis is called the fixed scale method. The spatial lattice size N_σ is different for two studies. $N_\sigma = 128$ for the first study and $N_\sigma = 64$ for the second study because though both the studies prefer the large spatial extent as we discussed above paragraph, the second study requires the large temporal extent. Moreover, the statistics of the input data is an important factor for the MEM analysis.

To improve statistics, we have measured the correlation functions eight times on each gauge configuration with different positions of the point source. The eight sources are located on two timeslices separated by $N_\tau/2$ with four sources in each timeslice with maximal separation. The correlation function on a configuration is then defined by the average of these eight measurements. We have checked that the statistics improves about $\sqrt{8}$ times with this treatment, suggesting that the correlation between eight measurements is well suppressed.

Chapter 7

Dynamical property of charmonia at the finite temperature

We show the dispersion relations and the momentum dependence of the strength of the peaks of the spectral function for charmonia in the pseudoscalar and vector channel, which correspond to η_c and J/ψ, respectively, on the basis of the method shown in Sec. 6.1.

This chapter is organized as follows. In Sec. 7.1, we show the detailed lattice set up. Next we show the numerical results. First, we show the temporal Euclidean correlators with nonzero momentum in Sec. 7.2. Sec. 7.3 shows the spectral functions reconstructed by MEM. We see the temperature dependence and the momentum dependence of the spectral function. Finally, the dispersion relation and the momentum dependence of the peak of the spectral functions analyzed by MEM are shown in Sec. 8.4.

7.1 Simulation set up

TABLE 7.1: Lattice simulation parameters.

T/T_c	N_τ	N_σ	$N_{\rm conf}$
1.70	44	64	700
1.62	46	64	500
1.56	48	64	500
1.49	50	64	500
1.38	54	64	500
0.78	96	64	500

In this study, we measure the momentum dependence of charmonium correlation functions Eq. (3.30) in the vector and pseudoscalar channels on the quenched anisotropic lattice. The lattice action and its parameters are shown in Chap. 6. In Table. 7.1, we summarize the lattice volumes $N_\sigma^3 \times N_\tau$, the temperature T in the unit of T_c [39], and the number of configurations $N_{\rm conf}$. We fix the lattice size for spatial direction to $N_\sigma = 64$. With the aid of the large anisotropy, our lattice has a large spatial volume; in physical unit the spatial length is $L_\sigma \simeq 2.5$ fm. The aspect ratio $\xi N_\sigma/N_\tau$ is 5.1 for $N_\tau = 50$. The large spatial extent enables a detailed study of the momentum dependence of the quantities on the lattice. With a periodic boundary condition along spatial direction, the momentum of bosons on the lattice is discretized as Eq.(6.28). In the analysis of Euclidean correlators we take the momentum along 1 direction, i.e. $\boldsymbol{p} = (p, 0, 0)$. The largest lattice with $N_\tau = 96$ and $T/T_c = 0.78$ is regarded as the vacuum one, in which the medium effects are well suppressed.

In the MEM analysis of spectral functions, we use a default model $m(\omega) = m_0\omega^2 + m_1 T\omega$ [80], where $m_0 = 1.15$ for the pseudoscalar channel and $m_0 = 0.40$ for the vector channel [39]. We analyzed the default model dependence of the reconstructed spectral

function by changing m_0 and m_1: m_0 is varied in the 50% range from the above values, while the dependence on m_1 is also checked in the range $0 \leq m_1 \leq 2.0$. We found that the dependence on m_0 and m_1 is well suppressed in this range near the peak of the J/ψ and η_c; the change of the spectral image caused by the variation of m_0 and m_1 in these ranges around the charmonium peak is less than a few percent. In the following analyses we thus set $m_1 = 0$. For nonzero p and large ω, it may be better to replace the default model by $m(\omega) = m_0(\omega^2 - p^2)$ as suggested from Lorentz invariance. We have performed MEM analysis with a default model

$$m(\omega) = \begin{cases} m_0(\omega^2 - p^2) & \omega^2 \geq p^2 + \epsilon \\ m_0\epsilon & \omega^2 < p^2 + \epsilon \end{cases}, \tag{7.1}$$

with several choices of small parameter ϵ. We, however, found that the default model dependence of our results is well suppressed again around the peak of the J/ψ and η_c, and the following numerical results hardly change.

For the analysis of $A_{\mathrm{T}}(\omega, p)$ and $A_{\mathrm{PS}}(\omega, p)$, we reconstruct them from the corresponding correlators $G_{\mathrm{T}}(\tau, p) = (G^2(\tau, \boldsymbol{p}) + G^3(\tau, \boldsymbol{p}))/2$ and $G_{\mathrm{PS}}(\tau, p) = G^5(\tau, \boldsymbol{p})$. On the other hand, $A_{\mathrm{L}}(\omega, p)$ can become negative and one cannot apply MEM to this channel directly. We thus analyze $A^1(\omega, \boldsymbol{p})$ from $G^1(\tau, \boldsymbol{p})$ with MEM and obtain $A_{\mathrm{L}}(\omega, p)$ using Eq. (3.43).

For sets of gauge configurations with $N_\tau = 48$ and 54, we observed that the reconstructed spectral images obtained in MEM analysis behave in an unreasonable way in some channels. We found that the error of the spectral functions tends to become large when such behaviors are observed. For example, although the spectral functions $A^i(\omega, \boldsymbol{p})$ with $\boldsymbol{p} = 0$ should be degenerated for $i = 1, 2$, and 3 because of rotational invariance, for $N_\tau = 48$ and 54, we observed that the reconstructed images of $A^i(\omega, \boldsymbol{p})$ behave in qualitatively different ways. It is also found that $P(\alpha)$ as a function of α has rapid changes for some values of α when such a pathological behavior is observed in MEM analysis. We have checked that these results do not come from the numerical resolution in our MEM algorithm by changing the numerical precision of our code. We have also checked that they do not depend on the choice of the default model. This problem is discussed in detail in Appendix A. In this study, we simply exclude $N_\tau = 48$ and 54 in the following discussion and concentrate on $N_\tau = 44,\ 46,\ 50$, and 96, which do not show such behaviors.

In the analysis of the dispersion relation Eq. (6.4) and the weight of the peak Eq. (6.2), the interval $I = [\omega_{\mathrm{min}}, \omega_{\mathrm{max}}]$ has to be chosen appropriately. In this study, we set $\omega_{\mathrm{min}} = 3$ GeV, while for the upper bound ω_{max} we use the value of ω at which the spectral function takes the first local minimum on the right of the peak corresponding to the J/ψ or η_c. We found that our numerical results for $\bar{Z}(p)$ and $\bar{E}(p)$, as well as their errors, are insensitive to the choice of the lower bound ω_{min}; for example, these quantities do not change within the numerical precision even if ω_{min} is set to 2 GeV. Our numerical analysis suggests that the results of $\bar{Z}(p)$ and $\bar{E}(p)$ hardly change for a variation of the lower and/or upper limits of I in the range where the reconstructed image takes a small value. The dependence of our results on the choice of ω_{max} will be discussed in Sec. 7.4.

7.2 Correlation function

In this section, we show the numerical results. We first see the momentum dependence of the correlation functions. Figure 7.1 shows the correlation functions $G^1(\tau, \boldsymbol{p})$ and

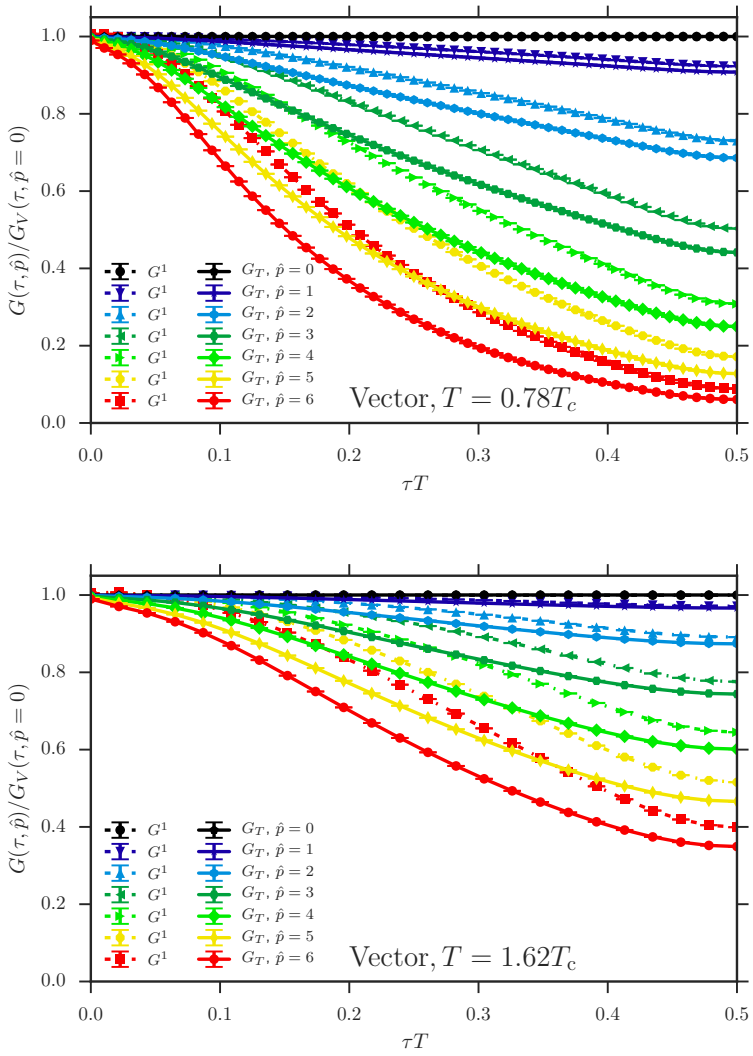

FIGURE 7.1: Momentum dependence of correlation functions for the vector channel, $G^1(\tau, \boldsymbol{p})$ and $G_{\mathrm{T}}(\tau, p)$, normalized by the correlation function with zero momentum $G_{\mathrm{V}}(\tau, 0)$ for $T = 0.78T_{\mathrm{c}}$ (upper) and $T = 1.62T_{\mathrm{c}}$ (lower). The dashed and solid lines represent $G^1(\tau, \boldsymbol{p})$ and $G_{\mathrm{T}}(\tau, p)$, respectively.

$G_{\mathrm{T}}(\tau, p)$ in the vector channel normalized by those with zero momentum,

$$G_{\mathrm{V}}(\tau, 0) = \frac{1}{3} \sum_{i=1,2,3} G^i(\tau, 0), \tag{7.2}$$

for various values of $\hat{p}$ below and above T_{c}. In the figure, the ratios $G^1(\tau, \boldsymbol{p})/G_{\mathrm{V}}(\tau, 0)$ and $G_{\mathrm{T}}(\tau, p)/G_{\mathrm{V}}(\tau, 0)$ are plotted by the dashed and solid lines, respectively. The errors in the figure are estimated for the ratios $G^1(\tau, \boldsymbol{p})/G_{\mathrm{V}}(\tau, 0)$ and $G_{\mathrm{T}}(\tau, p)/G_{\mathrm{V}}(\tau, 0)$ by the jackknife method; because of the strong correlation between correlation functions with different p, these errors are suppressed compared with those of the correlation functions themselves. The figure shows that the ratios $G^1(\tau, \boldsymbol{p})/G_{\mathrm{V}}(\tau, 0)$ and $G_{\mathrm{T}}(\tau, p)/G_{\mathrm{V}}(\tau, 0)$ become smaller as p is increased. This behavior is consistent with Eqs. (3.32) and (3.36) because as $E(p)$ becomes larger, the contribution of the bound state to the correlation function is more suppressed. The figure also shows that $G^1(\tau, \boldsymbol{p})$ and $G_{\mathrm{T}}(\tau, p)$ behave differently even at $T = 0.78T_{\mathrm{c}}$. As momentum become larger, the separation becomes

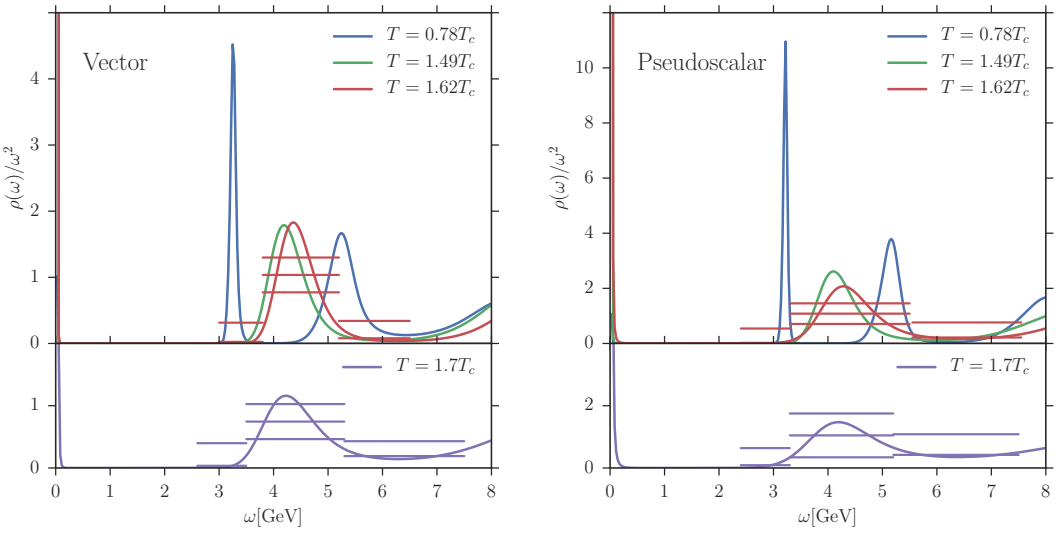

FIGURE 7.2: Spectral functions at $T/T_c = 0.78,\ 1.49,\ 1.62$, and 1.7 at zero momentum. The left and right panels show the vector and pseudoscalar channels, respectively. The horizontal lines show the averages of the spectral functions for some ranges of ω and their errors at $T/T_c = 1.62$ and 1.70.

more prominent with $G_T(\tau, p) < G^1(\tau, \boldsymbol{p})$. As we discussed in Sec. 3.2, $A_T(\omega, \boldsymbol{p}) = A_L(\omega, \boldsymbol{p}) = A_V(P^2)$ in the vacuum. From Eq. (3.43) we thus have

$$A_T(\omega, p) = \frac{\omega^2 - p^2}{\omega^2} A_1(\omega, \boldsymbol{p}). \tag{7.3}$$

Because the factor $(\omega^2 - p^2)/\omega^2$ is always smaller than unity, we have $A_T(\omega, p) \leq A_1(\omega, \boldsymbol{p})$, which leads to $G_T(\tau, p) \leq G^1(\tau, \boldsymbol{p})$. Similar behavior is observed for $T = 1.62T_c$.

7.3 Spectral function

Next, we analyze the T dependence of the spectral functions with MEM and study the existence of the peaks corresponding to the J/ψ and η_c at finite temperature. The left and right panels of Fig. 7.2 show the spectral functions with zero momentum in the vector and pseudoscalar channels, respectively. The error bars for the average of the spectral function for some intervals of ω estimated by Eq. (4.12) are shown by three horizontal lines for $T/T_c = 1.62$ and 1.70. The central lines show the averages of the spectral functions in the interval covered by the line, and the top and bottom ones indicate its 1σ error band. The result of the error analysis in the vector channel suggests that the peak corresponding to the J/ψ exists at $T = 1.62T_c$ with probabilistic significance. On the other hand, for the pseudoscalar channel at $T = 1.62T_c$, the error for the peak structure corresponding to the η_c has a small overlap with the error which is put for the right side valley of the structure. This shows that the plausibility of the existence of the peak is smaller than that for the vector channel. In other words, absence of the peak of η_c at $T = 1.62T_c$ cannot be excluded by 1σ.

In order to discuss the existence of the peak in the pseudoscalar channel at $T = 1.62T_c$ and the momentum dependence of the peaks, we next show the momentum dependence of the spectral functions in the vector and pseudoscalar channels at $T = 1.62T_c$ in the upper and lower panels in Fig. 7.3, respectively. In the upper panel, $A_T(\omega, p)$ and $A_L(\omega, p)$ are shown by the solid and dashed lines, respectively. In the lower panel, the

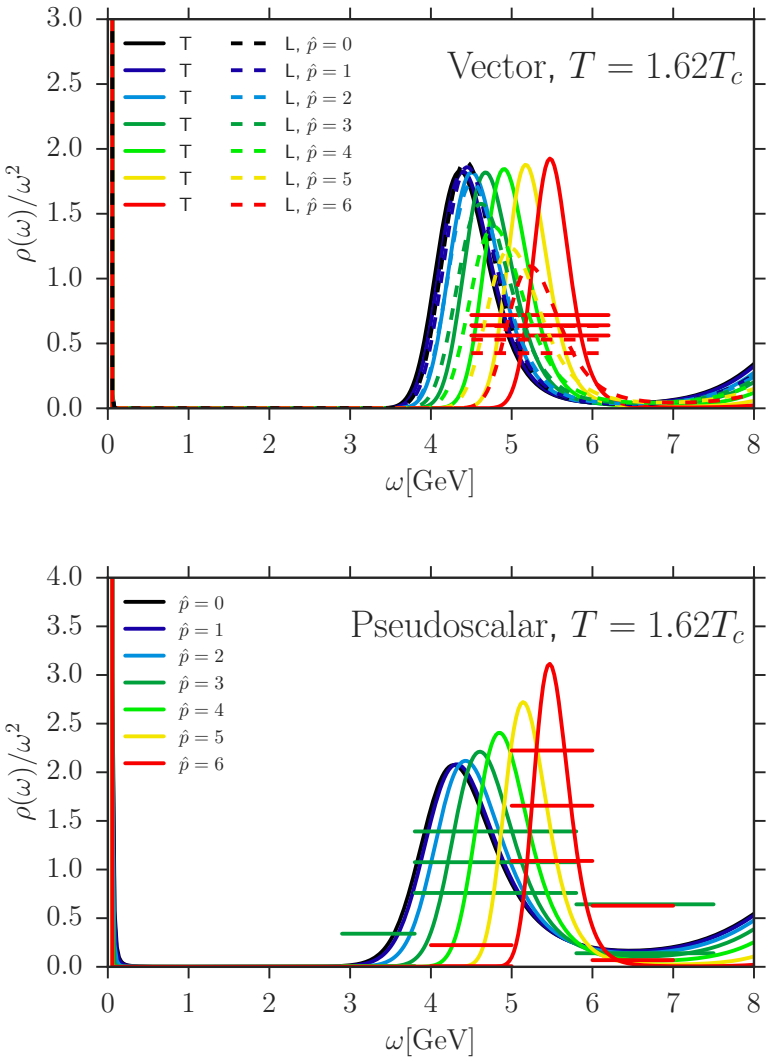

FIGURE 7.3: Momentum dependence of the spectral functions at $T = 1.62T_c$. The upper and lower panels show the vector and pseudoscalar channels, respectively. The error bars are shown for averages of the spectral functions for the vector channel at $\hat{p} = 6$ and for the pseudoscalar channel at $\hat{p} = 3$ and 6.

errors for the peaks of the spectral functions in the pseudoscalar channel are shown for $\hat{p} = 3$ and 6. The lower panel suggests that the peak corresponding to the η_c exists at $\hat{p} = 3$ and 6. The existence of the J/ψ peak in the vector channel at nonzero momenta is also indicated from the upper panel. We thus suppose that the J/ψ and η_c survive up to $T = 1.62T_c$, which is a consistent result as in previous works [39, 40], The possibility that the existence of the peak depends on p for $T = 1.62T_c$, however, is not excluded in these analyses.

Figure 7.3 also shows that the peaks corresponding to the J/ψ and η_c are well isolated from the second structure in the spectral functions. This suggests that the dependence of $\bar{Z}(p)$ and $\bar{E}(p)$ on $\omega_{\rm max}$ is suppressed so that these quantities can be analyzed with small ambiguity.

In Fig. 7.4, we show the momentum dependence of the spectral functions in the vector channel, $A_{\rm T}(\omega, p)$ and $A_{\rm L}(\omega, p)$, for $T = 0.78T_c$. To see the separation of the transverse and longitudinal channels, we show the errors for the averages of $A_{\rm T}(\omega, p)$ and $A_{\rm L}(\omega, p)$ with the same energy interval for $\hat{p} = 4$ and 6. From the figure, one

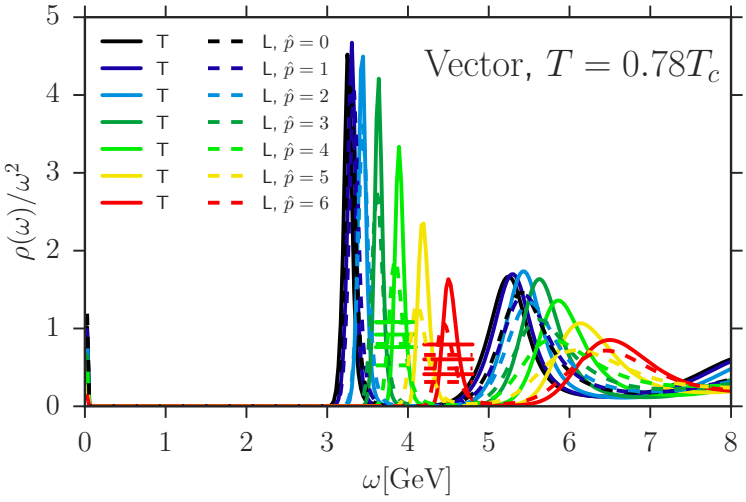

FIGURE 7.4: Momentum dependence of the spectral functions $A_{\mathrm{T}}(\omega, p)$ and $A_{\mathrm{L}}(\omega, p)$ in the vector channel at $T = 0.78T_{\mathrm{c}}$. Errors for the average of the spectral functions are shown for $\hat{p} = 4$ and 6.

observes that the spectral functions in the transverse and longitudinal channels agree with each other within the error. This result is consistent with the vacuum property of the spectral functions discussed in Sec. 3.2. It, however, is worth emphasizing that this agreement is obtained although $A_{\mathrm{T}}(\omega, p)$ and $A_{\mathrm{L}}(\omega, p)$ are constructed from completely different correlation functions as shown in Fig. 7.1. From the upper panel in Fig. 7.3, one also finds that the degeneracy of $A_{\mathrm{T}}(\omega, p)$ and $A_{\mathrm{L}}(\omega, p)$ is observed even for $T = 1.62T_{\mathrm{c}}$. This is a nontrivial result because these functions can behave differently because of the lack of Lorentz invariance.

7.4 Residue and dispersion relation

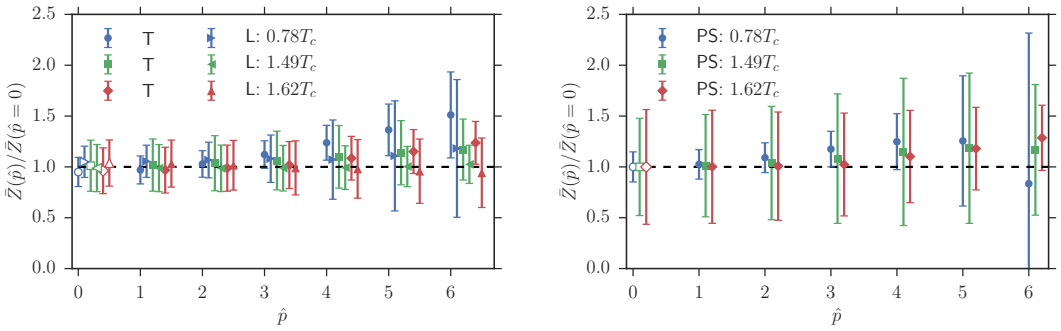

FIGURE 7.5: Ratio of the residues of the peaks, $\bar{Z}(p)/\bar{Z}(0)$, corresponding to the J/ψ (upper) and η_c (lower). The transverse (T) and longitudinal (L) components are shown in the upper panel.

Next, we turn to $\bar{Z}(p)$ and $\bar{E}(p)$. In Fig. 7.5, we show the momentum dependence of $\bar{Z}(p)$ obtained with Eq. (6.2) for the vector and pseudoscalar channels for $T/T_{\mathrm{c}} = 0.78$, 1.49, and 1.62. In the figure, the normalized results, $\bar{Z}(p)/\bar{Z}(0)$, are plotted in order to see the momentum dependence of $\bar{Z}(p)$. The errors in the figure include only the one of the numerator of the ratio estimated by MEM. The figure shows that $\bar{Z}(p)$ does not have momentum dependence within the error for all the temperatures and all the

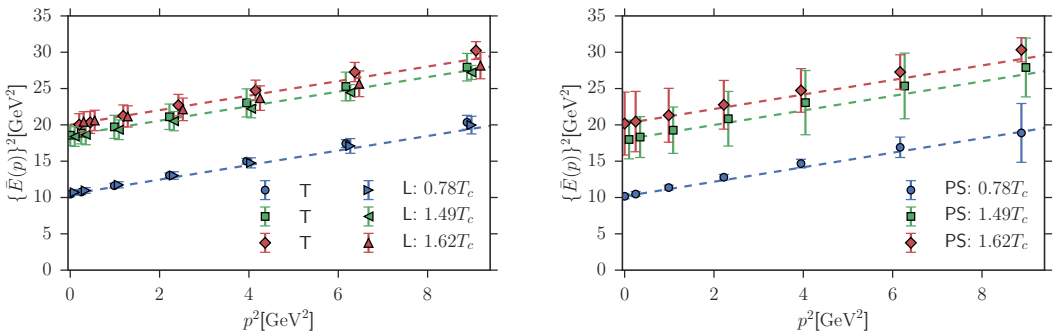

FIGURE 7.6: Dispersion relations $\bar{E}(p)$ of the J/ψ (upper) and η_c (lower) for $T/T_c = 0.78$, 1.49, and 1.62. The dashed lines indicate the vacuum dispersion relation Eq. (3.37) with $m = \bar{E}(0)$.

T/T_c	0.78	1.49	1.62
J/ψ	3.24(6)	4.30(16)	4.47(16)
η_c	3.19(5)	4.24(31)	4.49(48)

TABLE 7.2: Masses of the ground states of the charmonia in the vector and pseudoscalar channels defined by $\bar{m} = \bar{E}(0)$.

channels for which we carried out the analysis. This result is reasonable for $T/T_c = 0.78$, at which the medium effects should be well suppressed. Our analysis, however, shows that $\bar{Z}(p)$ is insensitive to p even at $T/T_c = 1.49$ and 1.62, which is a nontrivial result.

We note that the errors of $\bar{Z}(p)/\bar{Z}(0)$ in Fig. 7.5 would be reduced if we take into account the correlation between $\bar{Z}(p)$ and $\bar{Z}(0)$. In order to estimate the correlation, however, one has to perform the MEM analysis for two different correlation functions in a single analysis. Because we perform the MEM analysis for individual momenta, this correlation cannot be estimated in our analysis.

To see the medium effects on the dispersion relation, we show the results on $\bar{E}(p)$ in Fig. 7.6. In the figure, we plot the square of this quantity $(\bar{E}(p))^2$ as a function of p^2, since this plot is convenient to see the deviation of $\bar{E}(p)$ from the vacuum dispersion relation Eq. (3.37). From the figure, one first observes that the masses of the charmonia, defined by $\bar{m} = \bar{E}(0)$, become larger as T is increased. The values of $\bar{m}$ in the vector and pseudoscalar channels at $T/T_c = 0.78$, 1.49, and 1.62 are listed in Table 7.2.

Since the number of data points N_τ is different for each temperature, this difference may be the origin of the mass shift. Then, the mass shift summarized in Table. 7.2 can be an artifact of the MEM analysis and not be physical. To clarify this possibility we analyze the spectral function from the reconstructed correlator $G^{\rm rec}(\tau, 0, 2T; T)$ with $T = 0.78T_c$ given by Eq. (3.29). N_τ for $G^{\rm rec}(\tau, 0, 2T; T)$ is half of that for the original one $G(\tau, 0, T)$, since $G^{\rm rec}(\tau, 0, 2T; T)$ and $G(\tau, 0, T)$ are given by integrating the same spectral function $\rho(\omega, 0, T)$ with the different kernels, $K(\tau, \omega, 2T)$ and $K(\tau, \omega, T)$ in Eq. (3.33), respectively. The spectral function analyzed from $G^{\rm rec}(\tau, 0, 2T; T)$ is shown in Fig. 7.7 together with the original one. The peak positions of the first peak obtained from the original correlator and the reconstructed one is also compared in Table. 7.3. From the

correlator	$G(\tau, 0, T)$	$G^{\rm rec}(\tau, 0, 2T; T)$
$\bar{m}$	3.24(6)	3.40(90)

TABLE 7.3: Masses of the ground state of the charmonia in the vector channel defined by $\bar{m} = \bar{E}(0)$ analyzed from $G(\tau, 0, T)$ and $G^{\rm rec}(\tau, 0, 2T; T)$ with $T = 0.78T_c$.

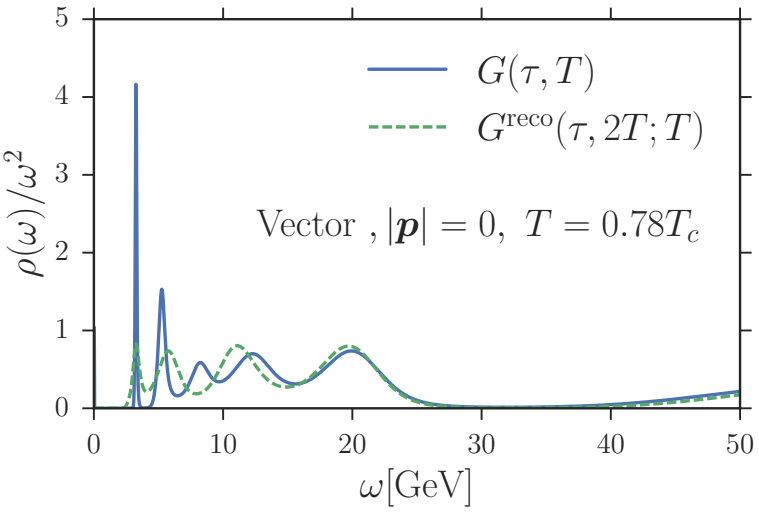

FIGURE 7.7: Spectral functions reconstructed from $G(\tau, 0, T)$ (solid line) and $G^{\mathrm{rec}}(\tau, 0, 2T; T)$ (dashed line) with $T = 0.78T_{\mathrm{c}}$.

these results we see that the shift of the first peak location is not observed, though the resolution of MEM becomes worse as N_τ is decreased. When we focus on the second and higher peaks, the numbers of the peak-like structures are different. Although these peaks are interpreted as the contribution of the doublers [41], the result suggests that the small number of the data points affect the resolution of MEM [117] and we have to take care the resolution of MEM in the analysis. Since the mass shift is obtained by analyzing the correlators with $N_\tau = 46,\ 50$, and 96, the possibility that this mass shift is the artifact of the MEM analysis is small. We thus conclude that the mass shift is physical.

Although such a mass shift in MEM analyses were suggested in previous study [51], our analysis confirms the medium effects on the mass of the charmonia with a quantitative error analysis for the first time.

In Fig. 7.6, the vacuum dispersion relation Eq. (3.37) with $m = \bar{m}$ is shown by the dashed lines. The figure shows that the functional form of $\bar{E}(p)$ is consistent with Eq. (3.37) within statistics even at $T/T_{\mathrm{c}} = 1.49$ and 1.62.

In order to see the dependence of these results on the choice of the interval $I = [\omega_{\mathrm{min}}, \omega_{\mathrm{max}}]$, in Fig. 7.8 we show the ω_{max} dependence of $\bar{E}(p = 0)$ for $N_\tau = 46$ in the vector channel with $\omega_{\mathrm{min}} = 3$ GeV. The value of ω_{max} used in Fig. 7.6, i.e. the minimum of the spectral function between the first and second peaks, is shown by the vertical dashed line. The figure shows that the value and error of $\bar{E}(p)$ are insensitive to the choice of ω_{max}. In fact, the variation of the result with the change of ω_{max} in ± 500 MeV is about four times smaller than the error. The same conclusions holds also for the other cases and for $\bar{Z}(p)$. As discussed already in Sec. 6.1, the numerical results hardly change with the variation of ω_{min}. For example, when we choose the lower bound as $\omega_{\mathrm{min}} = 2$ GeV, the numerical result overlaps with that in Fig. 7.8 within numerical precision. These results suggest that our analysis of $\bar{E}(p)$ is insensitive to the choice of the interval I and thus is well justified.

The results in Figs. 7.5 and 7.6 suggest that the momentum dependence of the charmonia hardly changes from the Lorentz covariant one in Eqs. (3.36) and (3.37) even well above T_{c}, although the rest mass m is significantly increased as T is raised. In vector channels, we do not observe difference between the transverse and longitudinal components within the error in MEM analysis even at finite temperature. These results are nontrivial because Lorentz symmetry is lost in medium, and quite interesting from

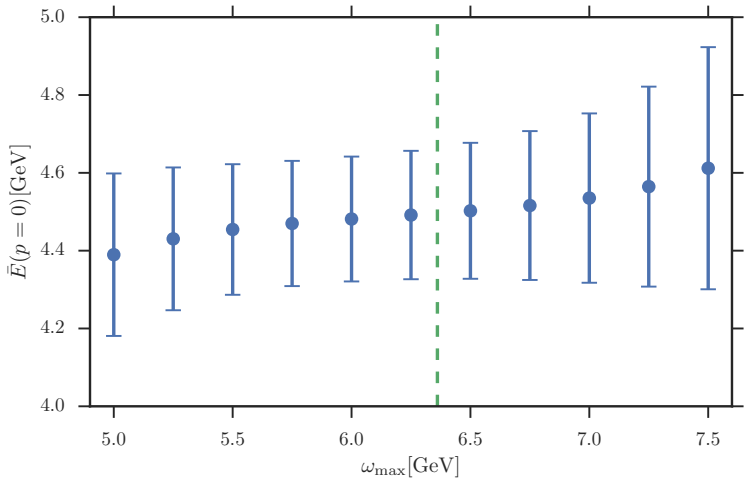

FIGURE 7.8: $\omega_{\max}$ dependence of $\bar{E}(p=0)$ for $N_\tau = 46$ for the J/ψ peak in the vector channel. The lower bound is fixed to $\omega_{\min} = 3$ GeV. The vertical dashed line shows the local minimum between the first and second peaks.

the phenomenological points of view.

Chapter 8

Charm quark diffusion coefficient and relaxation time

We have analyzed the charm quark diffusion coefficient on the lattice using the inequality Eq. (6.24) discussed in Chap. 6. The characteristics of this study is the use of the current-current correlator in temporal channel at nonzero momentum. This is contrasted to the previous studies with the Kubo formulas which analyze the spatial channel at zero momentum. At zero momentum, owing to the charge conservation the Euclidean correlator in temporal channel is given by a constant proportional to susceptibility. The correlator at nonzero momentum, on the other hand, is dependent on imaginary time and contain the information on dynamics. As we will see later, the temporal channel at nonzero momentum is more sensitive to the low-energy part of dynamical properties than the spatial one. The purpose of the present study is to exploit this sensitivity in the analysis of the transport coefficients.

This chapter is organized as follows. In Sec. 8.1 we show you the detailed simulation parameters. Next we show the numerical results. First, we show the temporal Euclidean correlators with nonzero momentum in Sec. 8.2. Sec. 8.3 shows the difference of the correlators with respect to momentum and linear extrapolation of $\tilde{p}^2$. Finally, the constraint for the diffusion coefficient and the relaxation time is shown in Sec. 8.4.

8.1 Simulation set up

As we discussed in Chap. 6, the large spatial extent of the lattice is important for this analysis and we have adopted the anisotropic lattice simulation owing to necessity of the correlators with a small nonzero momentum. The lattice action and its parameters are shown in Chap. 6. In the case of a naïve boson and the spatial lattice size N_σ, the discretized momentum is given by Eq.(6.28). Therefore, the lowest nonzero momentum is thus given by

$$\frac{p_{\rm min}}{T} \simeq 2\pi \frac{N_\tau}{\xi N_\sigma}. \tag{8.1}$$

In order to study the momentum dependence of $G_{00}(\tau, \boldsymbol{p})$ in the range $|\boldsymbol{p}|/T \lesssim 1$ at which hydrodynamic description of the system would be justified, we have to perform the simulation with small $N_\tau/(\xi N_\sigma)$. The anisotropic lattice is suitable to fulfill this requirement. We also perform the simulation with relatively large lattice size $N_\sigma = 128$ for each temperature. The value of $p_{\rm min}/T$ for each T is shown in Table 8.1. They are considerably smaller than unity. Our analysis thus can study p dependence for $p/T < 1$. In addition to this analysis, the simulation with $N_\sigma = 64$ is also carried out for $N_\tau = 32$ to study the finite volume effect.

For the charm quark current on the lattice, we use the local current operator $j_\mu(x) = \bar{c}(x)\gamma_\mu c(x)$ with $c(x)$ and $\bar{c}(x)$ are located on a same lattice site. As we will discuss later, the use of the conserved current operator would improve the analysis with a fixed lattice

TABLE 8.1: Lattice simulation parameters.

N_τ	T/T_c	N_σ	$p_{\min}/T$	$N_{\rm conf}$
16	4.67	128	0.196	361
20	3.73	128	0.245	229
24	3.11	128	0.294	240
28	2.67	128	0.344	91
32	2.33	128	0.397	100
32	2.33	64	0.794	304
36	2.07	128	0.442	100
40	1.87	128	0.491	100
44	1.70	128	0.540	89

spacing. The current-current correlators $G_{\mu\nu}(\tau, \boldsymbol{p})$ are measured with various choices of $\boldsymbol{p} = (p_x, p_y, p_z)$ to perform the analysis for possible integer values of $\tilde{p}^2$.

8.2 Correlation function

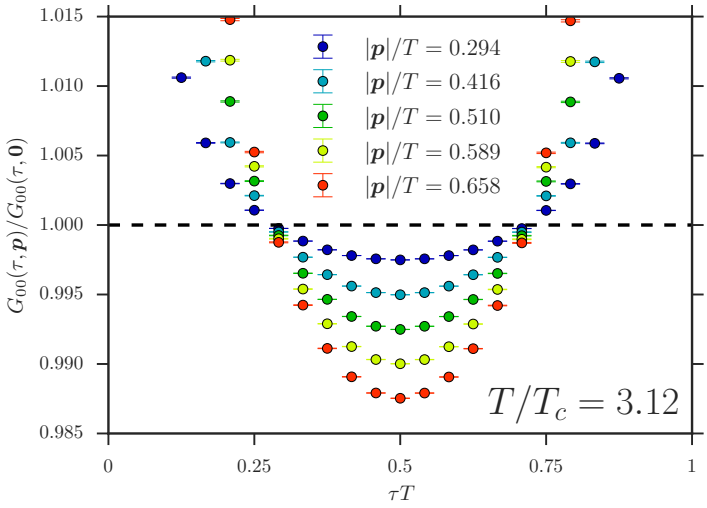

FIGURE 8.1: Momentum dependence of $G_{00}(\tau, \boldsymbol{p})$ normalized by $G_{00}(\tau, 0)$ for $N_\tau = 24$ and $N_\sigma = 128$.

In Fig. 8.1 we show the ratio $G_{00}(\tau, \boldsymbol{p})/G_{00}(\tau, 0)$ for the same correlator. The error is estimated by the jackknife analysis, which takes the correlation between $G_{00}(\tau, \boldsymbol{p})$ and $G_{00}(\tau, 0)$ into account. One finds that the ratio is determined with small statistical error of order 0.001%. The strong correlation between the correlators with different momenta measured on a same configuration suppresses the error of the ratio.

Focusing on the midpoint $\tau_{\rm mid} = 1/(2T)$, we see that $M_0(p) = G_{00}(\tau_{\rm mid}, \boldsymbol{p})$ is decreased as p is increased. This behavior means that $\partial_{\tilde{p}^2} M_0$ is negative. Because $\partial_{\tilde{p}^2} M_0^{\rm high}$ is positive, the negative $\partial_{\tilde{p}^2} M_0$ shows that $|\partial_{\tilde{p}^2} M_0^{\rm hydro}(p)| > \partial_{\tilde{p}^2} M_0^{\rm high}$. From the figure, one also finds that the second derivative of $G_{00}(\tau, \boldsymbol{p})$ at the midpoint is positive for $p > 0$ and increases as p becomes larger. This behavior indicates a positive $\partial_{\tilde{p}^2} M_2$.

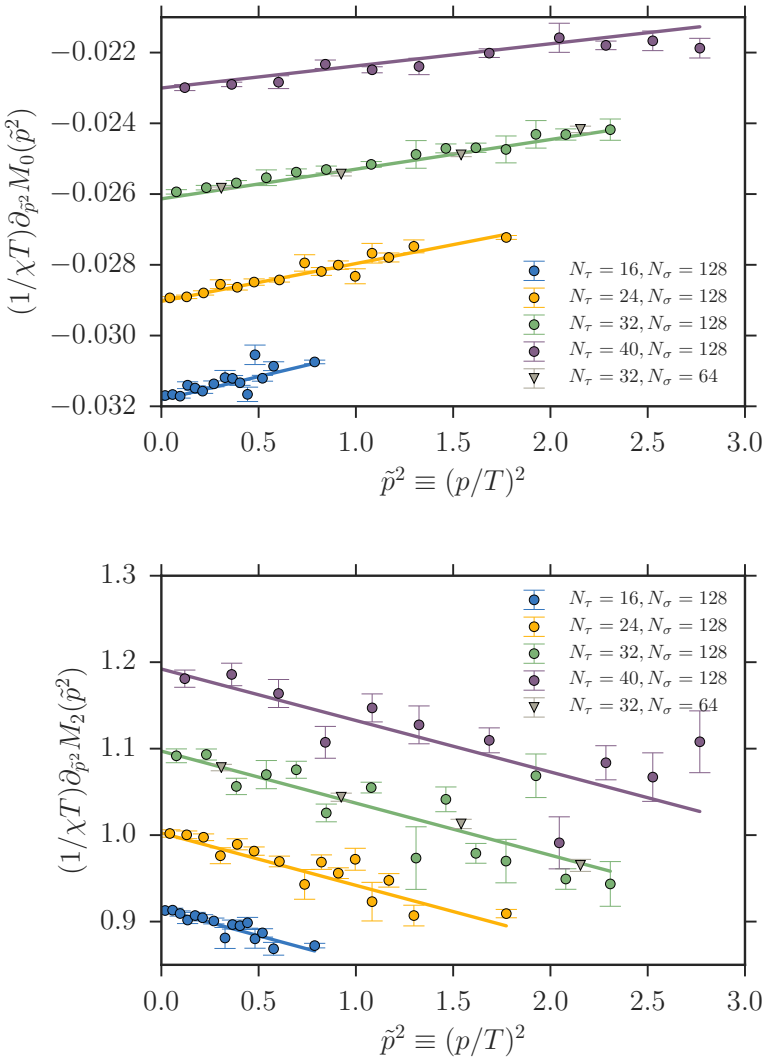

FIGURE 8.2: Momentum dependence of $\partial_{\tilde{p}^2} M_0(p^2)$ (upper) and $\partial_{\tilde{p}^2} M_2(p^2)$ (lower) normalized by χT. as functions of $\tilde{p}^2 = (p/T)^2$. The solid lines represents the result of linear fits with 6 data points from lower momentum.

8.3 Momentum derivatives

We next analyze $\partial_{\tilde{p}^2} M_0$ and $\partial_{\tilde{p}^2} M_2$. In our analysis, $M_0(p)$ for individual $\boldsymbol{p}$ is defined directly from the midpoint correlator as $M_0(p) = G_{00}(\tau_{\rm mid}, \boldsymbol{p})$. The value of $M_2(p)$ is estimated using $G_{00}(\tau, \boldsymbol{p})$ at five τ values around the midpoint by fitting the data with the correlated chi-square fit with the fitting function

$$G_{00}(\tau, \boldsymbol{p}) = m_0 + m_2(\tau - \tau_{\rm mid})^2 + m_4(\tau - \tau_{\rm mid})^4. \tag{8.2}$$

We then define the $\tilde{p}^2$ derivatives of $M_0(p)$ and $M_2(p)$ from the difference of $M_n(p)$ at the neighboring values of $\tilde{p}^2$. The $\tilde{p}^2$ dependences of $\partial_{\tilde{p}^2} M_0(p)$ and $\partial_{\tilde{p}^2} M_2(p)$ obtained in this way is shown in the upper and lower panels of Fig. 8.2, respectively, for several values of N_τ. The figure shows that these quantities behave almost linearly as functions of $\tilde{p}^2$. We thus take the zero momentum extrapolations of $M_n(p)$ by the linear extrapolation of $\tilde{p}^2$. The correlated chi-square fit is performed using six data points from small $\tilde{p}^2$. The result of $\partial_{\tilde{p}^2} M_0$ and $\partial_{\tilde{p}^2} M_2$ after the zero momentum extrapolation are summarized in Table 8.2. The same extrapolation is performed with five and seven data points, and

TABLE 8.2: Results of $\partial_{\tilde{p}^2} M_0/M_0$ and $\partial_{\tilde{p}^2} M_2/M_0$ after $p \to 0$ extrapolation. The first error shows the statistical one, while the second error is the systematic one estimated from the number of data points used for the linear extrapolations.

N_τ	N_σ	$-\partial_{\tilde{p}^2} M_0/M_0$	$\partial_{\tilde{p}^2} M_2/M_0$
16	128	0.03181(4)(1)	0.914(2)(1)
20	128	0.03045(7)(11)	0.965(3)(1)
24	128	0.02903(19)(9)	1.002(4)(2)
28	128	0.02745(24)(4)	1.043(7)(0)
32	128	0.02614(10)(13)	1.097(5)(1)
32	64	0.02621(6)(0)	1.094(4)(0)
36	128	0.02442(11)(7)	1.139(9)(5)
40	128	0.02300(15)(6)	1.192(11)(0)
44	128	0.02178(36)(19)	1.235(12)(0)

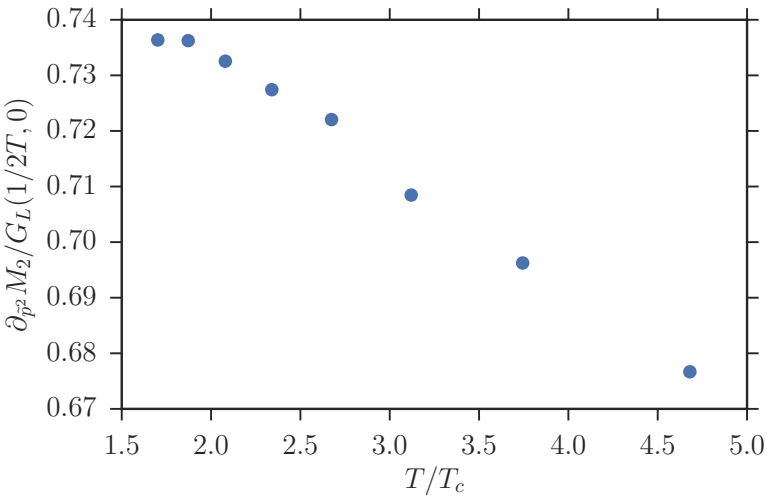

FIGURE 8.3: $\partial_{\tilde{p}^2} M_2/G_L(1/2T,0)$.

the largest difference is taken into account as a systematic error, which are shown by the second error in Table 8.2. The result of the fit is shown in Fig. 8.2 by solid lines. The nonzero slope of these lines suggest nonzero value of $\partial^2_{\tilde{p}^2} M_n(p)$. The values of χ^2/dof of the linear extrapolation is in the range $0.1 \sim 7.8$ which is slightly large. This would imply that the effect of $\partial^3_{\tilde{p}^2} M_n(p)$, which is not considered in the linear extrapolation, is not negligible, and thus the statistics of our data is high enough to analyze not only $\partial^2_{\tilde{p}^2} M_n(p)$ but also $\partial^3_{\tilde{p}^2} M_n(p)$.

In order to see the spatial volume dependence of these results, in Fig. 8.2 we show the results on the $N_\tau = 32$ and $N_\sigma = 64$ lattice. As the figure and the extrapolated values in Table 8.2 show, no difference is observed between $N_\sigma = 128$ and 64 for $N_\tau = 32$ within statistics. We thus conclude that the spatial volume dependence is well suppressed with $N_\sigma = 128$.

As in Eq. (6.26), $\partial_{\tilde{p}^2} M_2$ is also estimated from the correlator in spatial channel $G_{ii}(\tau, 0)$. We have performed this analysis, and found that the value of $\partial_{\tilde{p}^2} M_2(p)$ obtained from $G_{ii}(\tau_{\rm mid}, \boldsymbol{p})$ overestimates the value compared with those in Table 8.2 obtained from $G_{00}(\tau, 0)$. $\partial_{\tilde{p}^2} M_2/G_L(1/2T, 0)$ is shown in Fig. 8.3. We can see that the values from $G_{00}(\tau, 0)$ is about 30% smaller than that from $G_{ii}(\tau, \boldsymbol{p})$, and $\partial_{\tilde{p}^2} M_2/G_L(1/2T, 0)$ are not constant for different N_τ. This inconsistency would be attributed to the lattice artifact. First, because we employ the anisotropic lattice, the renormalization factor for

$j_\mu(\tau, \boldsymbol{x})$ arising from the discretization effect can be different for spatial and temporal channels. Second, the discretization effect violates the exact conservation law of $j_\mu(\tau, \boldsymbol{x})$ on the lattice. In particular, the use of the local current operator $j_\mu(\tau, \boldsymbol{x})$ in our analysis would make this effect large. Because Eq. (6.26) is obtained from the continuity equation Eq. (5.1), the violation of the conservation law can be the origin of the discrepancy. In this study, we employ the value obtained from $G_{00}(\tau, \boldsymbol{p})$. This choice is expected to suppress both of the above discretization effects, since (1) the renormalization factor is canceled out with this choice, and (2) the definition with $G_{00}(\tau, 0)$ is the one obtained directly from Eq. (5.5) without using the conservation law.

8.4 Diffusion coefficient and relaxation time

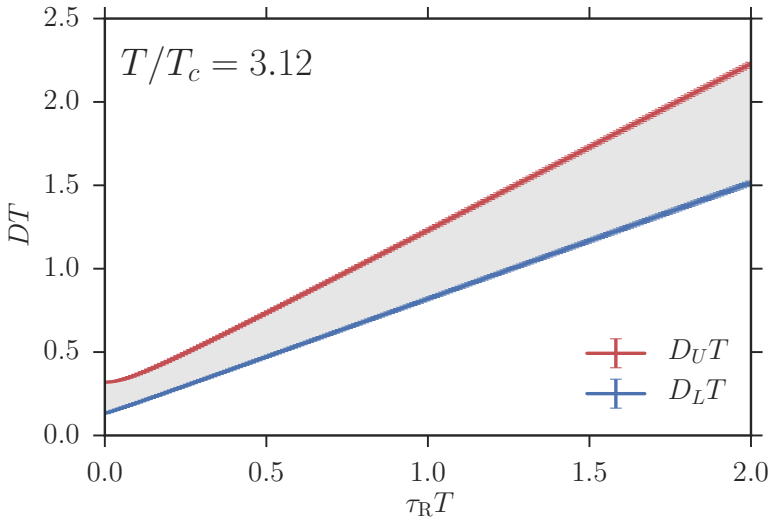

FIGURE 8.4: $\tilde{\tau}_R = \tau_R T$ dependences of $D_L(\tilde{\tau}_R)$ and $D_U(\tilde{\tau}_R)$ for $N_\tau = 24$ ($T/T_c = 3.12$). The region of D and τ_R allowed by Eq. (6.24) is shown by the shaded color.

In Fig. 8.4, we show $\tilde{\tau}_R$ dependences of $D_L(\tilde{\tau}_R)$ and $D_U(\tilde{\tau}_R)$ for $N_\tau = 24$ with $\partial_{\tilde{p}^2} M_n$ obtained in the previous section. The errors are smaller than the thickness of the lines. The shaded area in the figure shows the values of D and τ_R allowed by the inequality Eq. (6.24). The figure shows that the area is strongly constrained by Eq. (6.24) and the numerical results in the D–τ_R plane.

In the upper panel of Fig. 8.5, we show the T dependences of $D_L(\tilde{\tau}_R)$ and $D_U(\tilde{\tau}_R)$ with $\tilde{\tau}_R = 0,\ 0.5,\ 1.0$ and 1.5. One finds that the difference between $D_L(\tilde{\tau}_R)$ and $D_U(\tilde{\tau}_R)$ becomes small with increasing T. This suggests that the contribution of $\rho_{00}^{\text{high}}(\omega, \boldsymbol{p})$ on $\partial_{\tilde{p}^2} M_0(p)$ and $\partial_{\tilde{p}^2} M_2(p)$ is relatively suppressed as T becomes larger. The value of $D_L(0)$ provides the lower bound of D irrespective of the value of τ_R. As shown in the panel, the value is $0.15 < D_L(0)T < 0.25$ for $1.7 < T/T_c < 4.7$. Comparing the result in the panel with the previous studies [87, 88, 93] shown in Fig. 1.5, this lower bound is consistent with the value of D obtained in these study. The comparison of the panel with these previous studies also suggests that our result on D is consistent with the previous ones with $0.5 \lesssim \tilde{\tau}_R \lesssim 1.5$.

The inequality Eq. (6.24), however, is not responsible for the determination of the values of D and τ_R themselves as Fig. 8.4 shows. Additional constraints thus are required to obtain their values. In the heavy quark limit, it is known that D and τ_R are related

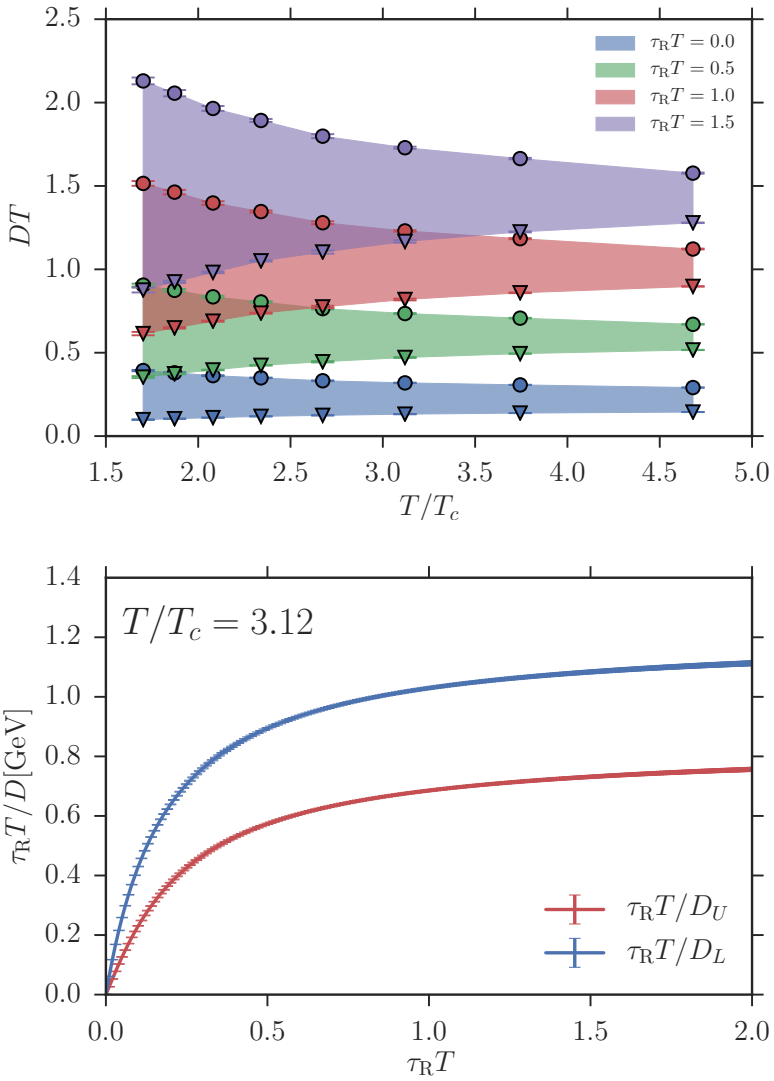

FIGURE 8.5: The T dependences of $D_{\mathrm{L}}(\tilde{\tau}_{\mathrm{R}})$ and $D_{\mathrm{U}}(\tilde{\tau}_{\mathrm{R}})$ with $\tilde{\tau}_{\mathrm{R}} = 0.0,\ 0.5,\ 1.0$, and 1.5 (upper). $\tilde{\tau}_{\mathrm{R}}$ dependences of $\tau_{\mathrm{R}}T/D_{\mathrm{L}}$ and $\tau_{\mathrm{R}}T/D_{\mathrm{U}}$ for $N_\tau = 24$ (lower). See Eq. (8.3) for discussion.

to the quark mass m_q as [86]

$$\frac{\tau_{\mathrm{R}}T}{D} = m_q. \tag{8.3}$$

In the lower panel of Fig. 8.5 we shows $\tilde{\tau}_{\mathrm{R}}$ dependence of $\tau_{\mathrm{R}}T/D_{\mathrm{L}}(\tilde{\tau}_{\mathrm{R}})$ and $\tau_{\mathrm{R}}T/D_{\mathrm{U}}(\tilde{\tau}_{\mathrm{R}})$ as functions of $\tilde{\tau}_{\mathrm{R}}$ for $T = 3.12T_{\mathrm{c}}$. Assuming the validity of Eq. (8.3) for charm quarks and $m_q \simeq 1$ GeV, The panel suggests $\tau_{\mathrm{R}}T \gtrsim 1$.

Chapter 9

Summary

In this thesis we measured charmonia correlators at the finite temperature with nonzero momenta in anisotropic quenched lattices. We adopted the anisotropic Wilson gauge action with $\beta = 7.0$ and the renormalized anisotropy $\xi = 4.0$, and the Wilson fermion action with the spatial hopping parameter $\kappa_\sigma = 0.08285$ and the fermion anisotropy $\gamma_F = 3.476$ for the calculations. The temporal lattice spacing in physical unit is $a_\tau = 0.00975$fm. The simulations on the anisotropic lattices with the spatial lattice spacing four times larger than the temporal one and the spatial lattice sizes $N_\sigma = 64$ and 128 enable the detailed analysis of the momentum dependence of the correlators at the finite temperature. We studied the temperature dependence of the correlators by changing the temporal lattice size with the fixed lattice spacing. The temporal lattice sizes are $N_\tau = 32,\ 44,\ 46,\ 48,\ 50,\ 54$, and 96 for $N_\sigma = 64$ and $N_\tau = 16,\ 20,\ 24,\ 28,\ 32,\ 36,\ 40$, and 44 for $N_\sigma = 128$.

We have applied MEM to the correlators with $N_\sigma = 64$ at $T/T_\mathrm{c} = 0.78 \sim 1.70$. We have analyzed the momentum dependence of the peaks of the spectral functions corresponding to η_c and J/ψ in the vacuum and in medium. In addition to the standard analysis of spectral functions, we focus on the residue and dispersion relations for charmonia. To analyze these quantities with error in MEM, we have introduced the definitions in Eqs. (6.2) and (6.3). We have numerically checked that the peaks corresponding to the J/ψ and η_c can be studied by this analysis, as they are well isolated and the results are insensitive to the choice of the interval I.

In the vacuum, the dispersion relations for charmonia in all channels, pseudoscalar and vector, are consistent with the Lorentz covariant form and the residues for the bound states do not show the momentum dependence. In the vector channel, the peaks for the transverse and longitudinal components agree with each other within probabilistic significance. At finite temperature, we find the significant mass enhancement of charmonia as medium effects. On the other hand, the dispersion relations are consistent with that in the vacuum even at $T \simeq 1.6T_\mathrm{c}$ within probabilistic significance in MEM. Difference of the spectral functions between the transverse and longitudinal components in the vector channel is not observed. These results suggest an interesting observation that the medium effect on momentum dependence is well suppressed, although further improvement in statistics is required to obtain more accurate conclusion. We finally remark that these results cannot be explained by the naïve potential model. It is not explained by the threshold enhancement [118], either. These results suggest that the mass shift at finite temperature is caused by the nonperturbative interaction between charmonia and gluons in the medium.

We derived inequality Eq. (6.24) constraining the values of D and τ_R using the momentum derivatives of Euclidean correlator. The analysis of the lattice correlators for $1.7 < T/T_\mathrm{c} < 4.7$ shows that these transport coefficients are nicely constrained in the D–τ_R plane. This result suggests that the correlator $G_{00}(\tau, \boldsymbol{p})$ is useful for the study of the transport coefficients. Although in the present study we used $G_{00}(\tau, \boldsymbol{p})$ only to derive the inequality Eq. (6.24), it is interesting to pursue a better usage of this correlator in the analysis of the transport coefficients. One of such a possibility is to introduce a constraint on the form of $\rho_\mathrm{L}^\mathrm{high}(\omega, \boldsymbol{p})$ using, for example, the knowledge on the high energy

behavior obtained from perturbative QCD [119]. As we obtained inequalities Eq. (6.24) without assumptions on $\rho_{\mathrm{L}}^{\mathrm{high}}(\omega, 0)$ except for its semi-positivity, further constraint on this function strengthen the restriction of the transport coefficients.

Another interesting possibility is the simultaneous use of the correlators $G_{00}(\tau, \boldsymbol{p})$ and $G_{ii}(\tau, \boldsymbol{p})$ in the analysis of the spectral function. Because of Eq. (5.29), these correlators are sensitive to different regions of ω. Therefore, the mixed use of two information will lead us to more robust analysis of the spectral function. A first step along this direction may be the use of $\rho_{00}^{\mathrm{high}}(\omega, \boldsymbol{p})$ estimated from $G_{ii}(\tau, \boldsymbol{p})$ in the analysis of $G_{00}(\tau, \boldsymbol{p})$. Ultimately, the Bayesian analysis of the spectral function with the simultaneous use of $G_{00}(\tau, \boldsymbol{p})$ and $G_{ii}(\tau, \boldsymbol{p})$ would also be possible. As discussed in Sec. 8.3, however, in the present numerical analysis we observed a mismatch between the value of $\partial_{\tilde{p}^2} M_2$ obtained from $G_{00}(\tau, \boldsymbol{p})$ and $G_{ii}(\tau, \boldsymbol{p})$, presumably due to the violation of the conservation law owing to lattice artifact. The suppression of this effect is a crucial step to perform the above analyses with the use of Eq. (5.29). The use of the continuum extrapolated correlators [83] would be able to avoid the problem.

Although in this study we restricted ourselves to the analysis of the current-current correlator, the formalism in Chap. 5 can be extended to the correlator of energy-momentum tensor in a straightforward manner [90]. In this case, one obtains an equality for sound velocity and inequalities to constrain shear and bulk viscosities. The analysis of these transport coefficients with the momentum dependences of the correlator is an important future study. Of coarse, the analyses of diffusion coefficients of quarks with different masses, such as bottom, strange and light quarks, are another direct applications of the present study.

Appendix A

Failure of MEM analysis

As discussed in Sec. 7.1, in our MEM analysis we observed that the output spectral images behave in an unreasonable way in some channels and momenta on several sets of configurations. In this appendix, we discuss this problem in detail and show a criterion to remove them from the analysis.

Let us first specify the problem. In Fig. A.1, we show the spectral functions in the vector channel at zero momentum $\rho^i(\omega, \boldsymbol{p} = 0)$ obtained by MEM for $i = 1$, 2, and 3 with $N_\tau = 54$ ($T = 1.38T_c$). Because of rotational symmetry, these three spectral functions have to degenerate. Moreover, since our analysis discussed in Sec. 7.3 shows the existence of a peak corresponding to the J/ψ at $T/T_c = 1.49$ and 1.62, the spectral function for $T = 1.38T_c$ should also have the pea In Fig. A.1, we indeed observe the peak in $\rho^2(\omega, 0)$ and $\rho^3(\omega, 0)$. The peak, however, is not observed in $\rho^1(\omega, 0)$. This result shows that the reconstruction of the spectral image in MEM does not work well for $\rho^1(\omega, 0)$. In the figure, the errors for the averages of $\rho^i(\omega, 0)$ around the J/ψ peak are also shown. The result shows that the averages for all channels agree with one another within the error, although the error for $\rho^1(\omega, 0)$ is large. In this sense, the MEM analysis gives the consistent results for these three channels. It, however, seems obvious from the figure that the MEM analysis for $\rho^1(\omega, 0)$ is not working well compared with the other two channels.

We observed this kind of unstable results in some channels and momenta for $N_\tau = 48$ and 54. We have checked that the increase of statistics does not always resolve this problem; this problem sometimes manifests itself when the number of gauge configurations is increased. We have also checked that this problem does not come from the finite numerical precision in our MEM code by confirming that the same problem shows up even if we change the numerical precision in our code from double to quadruple. It has been also checked that the change of the default model does not cure this problem.

We found that when the output spectral image shows an unstable behavior, the probability $P(\alpha)$ in Eq. (4.9) behaves pathologically as a function of α. In Fig. A.2, we show the probabilities $P^i(\alpha)$ for the three channels corresponding to the results in Fig. A.1. In the figure, $P^i(\alpha)$ is shown for 25 jackknife samples, i.e. the results for 25 sets of configurations in which 1/25 succeeding configurations are removed from the total configurations. From the figure, one finds that $P^1(\alpha)$ has an almost discontinuous kink structure while $P^2(\alpha)$ and $P^3(\alpha)$ behave smoothly as a function of α. The figure also shows that the existence of the kink is robust against the small variation of the set of gauge configurations. We found that when $P(\alpha)$ has such kink structures, the output spectral image behaves in an unstable way as in $\rho^1(\omega, \boldsymbol{p})$ in Fig. A.1.

At present, we have not clarified the origin of this pathological behaviors. One possibility for the origin of this behavior is the numerical precision of the lattice simulation and correlation functions. The numerical simulations, however, have been performed in double precision and it is difficult to alter the precision.

The pathological behavior of $P(\alpha)$ is observed on the analysis for $N_\tau = 54$ and 48, while we do not observe it for $N_\tau = 96$, 50, 46, and 44. In our study, we simply exclude the results of $N_\tau = 54$ and 48 from our analysis and concentrate on the other four N_τ values, which do not have the problem.

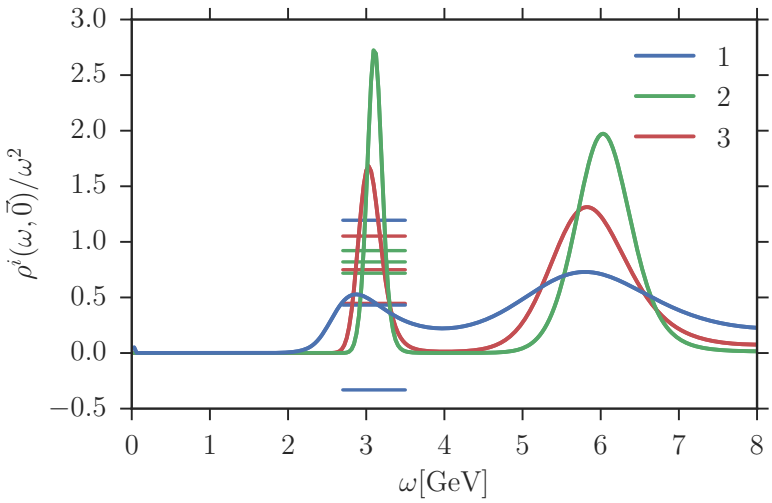

FIGURE A.1: Reconstructed spectral images $\rho^i(\omega, 0)$ with $i = 1,\ 2$, and 3 and for $N_\tau = 54$. The errors for the first peak in the spectral functions are measured at the same ω interval.

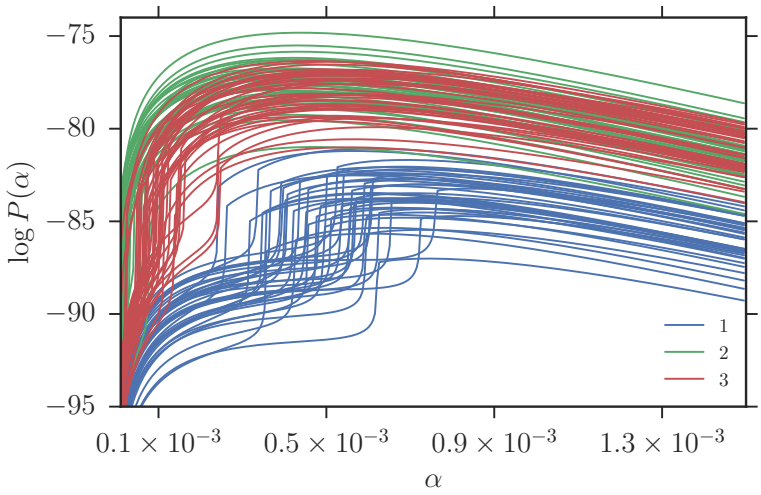

FIGURE A.2: α dependence of $P^i(\alpha)$ with $i = 1, 2$, and 3. The results are shown for 25 jackknife samples for each i. The reference point of the vertical axis is arbitrary.

Bibliography

[1] C.-N. Yang, and R. L. Mills, "Conservation of Isotopic Spin and Isotopic Gauge Invariance", Phys. Rev. **96**, 191–195 (1954).

[2] G. 't Hooft, "Renormalization of Massless Yang-Mills Fields", Nucl. Phys. **B33**, 173–199 (1971).

[3] G. 't Hooft, "Renormalizable Lagrangians for Massive Yang-Mills Fields", Nucl. Phys. **B35**, 167–188 (1971).

[4] D. J. Gross, and F. Wilczek, "Ultraviolet Behavior of Nonabelian Gauge Theories", Phys. Rev. Lett. **30**, 1343–1346 (1973).

[5] H. D. Politzer, "Reliable Perturbative Results for Strong Interactions?", Phys. Rev. Lett. **30**, 1346–1349 (1973).

[6] M. Gell-Mann, "A Schematic Model of Baryons and Mesons", Phys. Lett. **8**, 214–215 (1964).

[7] G. Zweig, "An SU(3) model for strong interaction symmetry and its breaking. Version 1", (1964).

[8] M. Y. Han, and Y. Nambu, "Three Triplet Model with Double SU(3) Symmetry", Phys. Rev. **139**, B1006–B1010 (1965).

[9] C. Patrignani, et al., "Review of Particle Physics", Chin. Phys. **C40**, 100001 (2016).

[10] S. L. Glashow, J. Iliopoulos, and L. Maiani, "Weak interactions with lepton-hadron symmetry", Phys. Rev. D **2**, 1285–1292 (1970).

[11] J. E. Augustin, et al., "Discovery of a Narrow Resonance in e^+e^- Annihilation", Phys. Rev. Lett. **33**, 1406–1408 (1974).

[12] J. J. Aubert, et al., "Experimental Observation of a Heavy Particle J", Phys. Rev. Lett. **33**, 1404–1406 (1974).

[13] M. Kobayashi, and T. Maskawa, "CP Violation in the Renormalizable Theory of Weak Interaction", Prog. Theor. Phys. **49**, 652–657 (1973).

[14] S. W. Herb, et al., "Observation of a Dimuon Resonance at 9.5-GeV in 400-GeV Proton-Nucleus Collisions", Phys. Rev. Lett. **39**, 252–255 (1977).

[15] F. Abe, et al., "Observation of top quark production in $\bar{p}p$ collisions", Phys. Rev. Lett. **74**, 2626–2631 (1995), arXiv:hep-ex/9503002 [hep-ex].

[16] S. Abachi, et al., "Search for high mass top quark production in $p\bar{p}$ collisions at $\sqrt{s} = 1.8$ TeV", Phys. Rev. Lett. **74**, 2422–2426 (1995), arXiv:hep-ex/9411001 [hep-ex].

[17] J. C. Collins, and M. J. Perry, "Superdense Matter: Neutrons Or Asymptotically Free Quarks?", Phys. Rev. Lett. **34**, 1353 (1975).

[18] N. Cabibbo, and G. Parisi, "Exponential Hadronic Spectrum and Quark Liberation", Phys. Lett. **B59**, 67–69 (1975).

[19] Y. Aoki, Z. Fodor, S. D. Katz, and K. K. Szabo, "The QCD transition temperature: Results with physical masses in the continuum limit", Phys. Lett. **B643**, 46–54 (2006), arXiv:hep-lat/0609068 [hep-lat].

[20] Y. Aoki, S. Borsanyi, S. Durr, Z. Fodor, S. D. Katz, S. Krieg, and K. K. Szabo, "The QCD transition temperature: results with physical masses in the continuum limit II.", JHEP **06**, 088 (2009), arXiv:0903.4155 [hep-lat].

[21] A. Bazavov, et al., "The chiral and deconfinement aspects of the QCD transition", Phys. Rev. **D85**, 054503 (2012), arXiv:1111.1710 [hep-lat].

[22] S. Borsanyi, S. Durr, Z. Fodor, C. Holbling, S. D. Katz, S. Krieg, D. Nogradi, K. K. Szabo, B. C. Toth, and N. Trombitas, "QCD thermodynamics with continuum extrapolated Wilson fermions II", Phys. Rev. **D92**, 014505 (2015), arXiv:1504.03676 [hep-lat].

[23] K. Yagi, T. Hatsuda, and P. Y. Miake, *Quark-gluon plasma: from big bang to little bang*, first edition (Cambridge University Press, Cambridge; New York, Oct. 30, 2008), 468 pp.

[24] T. Ludlam, and L. McLerran, "What have we learned from the Relativistic Heavy Ion Collider?", Phys. Today **56N10**, 48–54 (2003).

[25] E. Iancu, "QCD in heavy ion collisions", 197–266 (2014), arXiv:1205.0579 [hep-ph].

[26] T. Hashimoto, K. Hirose, T. Kanki, and O. Miyamura, "Mass Shift of Charmonium Near Deconfining Temperature and Possible Detection in Lepton Pair Production", Phys. Rev. Lett. **57**, 2123 (1986).

[27] T. Matsui, and H. Satz, "J/ψ Suppression by Quark-Gluon Plasma Formation", Phys. Lett. **B178**, 416–422 (1986).

[28] H. Satz, "Colour deconfinement and quarkonium binding", J. Phys. **G32**, R25 (2006), arXiv:hep-ph/0512217 [hep-ph].

[29] N. Brambilla, et al., "Heavy quarkonium: progress, puzzles, and opportunities", Eur. Phys. J. **C71**, 1534 (2011), arXiv:1010.5827 [hep-ph].

[30] A. Andronic, et al., "Heavy-flavour and quarkonium production in the LHC era: from proton – proton to heavy-ion collisions", Eur. Phys. J. **C76**, 107 (2016), arXiv:1506.03981 [nucl-ex].

[31] D. Kharzeev, C. Lourenco, M. Nardi, and H. Satz, "A Quantitative analysis of charmonium suppression in nuclear collisions", Z. Phys. **C74**, 307–318 (1997), arXiv:hep-ph/9612217 [hep-ph].

[32] M. L. Miller, K. Reygers, S. J. Sanders, and P. Steinberg, "Glauber modeling in high energy nuclear collisions", Ann. Rev. Nucl. Part. Sci. **57**, 205–243 (2007), arXiv:nucl-ex/0701025 [nucl-ex].

[33] B. B. Abelev, et al., "Centrality, rapidity and transverse momentum dependence of J/ψ suppression in Pb-Pb collisions at $\sqrt{s_{\rm NN}}$=2.76 TeV", Phys. Lett. **B734**, 314–327 (2014), arXiv:1311.0214 [nucl-ex].

[34] B. Abelev, et al., "J/ψ suppression at forward rapidity in Pb-Pb collisions at $\sqrt{s_{NN}}$ = 2.76 TeV", Phys. Rev. Lett. **109**, 072301 (2012), arXiv:1202.1383 [hep-ex].

[35] A. Adare, et al., "J/ψ suppression at forward rapidity in Au+Au collisions at $\sqrt{s_{NN}}$ = 200 GeV", Phys. Rev. **C84**, 054912 (2011), arXiv:1103.6269 [nucl-ex].

[36] W. Israel, and J. M. Stewart, "Transient relativistic thermodynamics and kinetic theory", Annals Phys. **118**, 341–372 (1979).

[37] B. Müller, "Investigation of Hot QCD Matter: Theoretical Aspects", Phys. Scripta **T158**, 014004 (2013), arXiv:1309.7616 [nucl-th].

[38] A. Adare, et al., "Heavy-quark production and elliptic flow in Au+Au collisions at $\sqrt{s_{NN}}$ = 62.4 GeV", Phys. Rev. **C91**, 044907 (2015), arXiv:1405.3301 [nucl-ex].

[39] M. Asakawa, and T. Hatsuda, "J/ψ and η_c in the deconfined plasma from lattice QCD", Phys. Rev. Lett. **92**, 012001 (2004), arXiv:hep-lat/0308034 [hep-lat].

[40] S. Datta, F. Karsch, P. Petreczky, and I. Wetzorke, "Behavior of charmonium systems after deconfinement", Phys. Rev. **D69**, 094507 (2004), arXiv:hep-lat/0312037 [hep-lat].

[41] T. Umeda, K. Nomura, and H. Matsufuru, "Charmonium at finite temperature in quenched lattice QCD", Eur. Phys. J. **C39S1**, 9–26 (2005), arXiv:hep-lat/0211003 [hep-lat].

[42] S. Datta, F. Karsch, P. Petreczky, and I. Wetzorke, "Meson correlators above deconfinement", J. Phys. **G31**, S351–S356 (2005), arXiv:hep-lat/0412037 [hep-lat].

[43] A. Jakovac, P. Petreczky, K. Petrov, and A. Velytsky, "Quarkonium correlators and spectral functions at zero and finite temperature", Phys. Rev. **D75**, 014506 (2007), arXiv:hep-lat/0611017 [hep-lat].

[44] T. Umeda, "A Constant contribution in meson correlators at finite temperature", Phys. Rev. **D75**, 094502 (2007), arXiv:hep-lat/0701005 [hep-lat].

[45] H. Ohno, S. Aoki, S. Ejiri, K. Kanaya, Y. Maezawa, H. Saito, and T. Umeda, "Charmonium spectral functions with the variational method in zero and finite temperature lattice QCD", Phys. Rev. **D84**, 094504 (2011), arXiv:1104.3384 [hep-lat].

[46] H. T. Ding, A. Francis, O. Kaczmarek, F. Karsch, H. Satz, and W. Soeldner, "Charmonium properties in hot quenched lattice QCD", Phys. Rev. **D86**, 014509 (2012), arXiv:1204.4945 [hep-lat].

[47] S. Borsanyi, et al., "Charmonium spectral functions from 2+1 flavour lattice QCD", JHEP **04**, 132 (2014), arXiv:1401.5940 [hep-lat].

[48] M. Jarrell, and J. E. Gubernatis, "Bayesian inference and the analytic continuation of imaginary-time quantum Monte Carlo data", Phys. Rept. **269**, 133–195 (1996).

[49] M. Asakawa, T. Hatsuda, and Y. Nakahara, "Maximum entropy analysis of the spectral functions in lattice QCD", Prog. Part. Nucl. Phys. **46**, 459–508 (2001), arXiv:hep-lat/0011040 [hep-lat].

[50] S. Datta, F. Karsch, S. Wissel, P. Petreczky, and I. Wetzorke, "Charmonia at finite momenta in a deconfined plasma", in 6th International Conference on Strong and Electroweak Matter (SEWM 2004) Helsinki, Finland, June 16-19, 2004 (2004), arXiv:hep-lat/0409147 [hep-lat].

[51] C. Nonaka, M. Asakawa, M. Kitazawa, and Y. Kohno, "Charmonium spectral functions at finite momenta in the gluon plasma from lattice QCD", J. Phys. **G38**, 124109 (2011).

[52] M. B. Oktay, and J.-I. Skullerud, "Momentum-dependence of charmonium spectral functions from lattice QCD", (2010), arXiv:1005.1209 [hep-lat].

[53] G. Aarts, C. Allton, S. Kim, M. P. Lombardo, M. B. Oktay, S. M. Ryan, D. K. Sinclair, and J.-I. Skullerud, "S wave bottomonium states moving in a quark-gluon plasma from lattice NRQCD", JHEP **03**, 084 (2013), arXiv:1210.2903 [hep-lat].

[54] H.-T. Ding, "Momentum dependences of charmonium properties from lattice QCD", Nucl. Phys. **A904-905**, 619c–622c (2013), arXiv:1210.5442 [nucl-th].

[55] H. Liu, K. Rajagopal, and U. A. Wiedemann, "An AdS/CFT Calculation of Screening in a Hot Wind", Phys. Rev. Lett. **98**, 182301 (2007), arXiv:hep-ph/0607062 [hep-ph].

[56] M. L. Bellac, *Thermal field theory*, Revised.ver. (Cambridge University Press, Cambridge, Oct. 1, 2000), 272 pp.

[57] E. V. Shuryak, "Physics of the pion liquid", Phys. Rev. **D42**, 1764–1776 (1990).

[58] R. D. Pisarski, and M. Tytgat, "Propagation of cool pions", Phys. Rev. **D54**, R2989–R2993 (1996), arXiv:hep-ph/9604404 [hep-ph].

[59] L. Van Hove, "The occurrence of singularities in the elastic frequency distribution of a crystal", Phys. Rev. **89**, 1189–1193 (1953).

[60] E. Braaten, R. D. Pisarski, and T.-C. Yuan, "Production of Soft Dileptons in the Quark - Gluon Plasma", Phys. Rev. Lett. **64**, 2242 (1990).

[61] M. Kitazawa, T. Kunihiro, and Y. Nemoto, "Possible generation of anomalously soft quark excitations at nonzero temperature: Nonhyperbolic dispersion of the parapion and van Hove singularity", Phys. Rev. **D89**, 056002 (2014), arXiv:1312.3022 [hep-ph].

[62] T. Kim, M. Asakawa, and M. Kitazawa, "Dilepton production spectrum above Tc with a lattice quark propagator", Phys. Rev. **D92**, 114014 (2015), arXiv:1505.07195 [nucl-th].

[63] F. Karsch, and H. W. Wyld, "Thermal Green's Functions and Transport Coefficients on the Lattice", Phys. Rev. **D35**, 2518 (1987).

[64] G. Policastro, D. T. Son, and A. O. Starinets, "The Shear viscosity of strongly coupled N=4 supersymmetric Yang-Mills plasma", Phys. Rev. Lett. **87**, 081601 (2001), arXiv:hep-th/0104066 [hep-th].

[65] P. B. Arnold, G. D. Moore, and L. G. Yaffe, "Transport coefficients in high temperature gauge theories. 2. Beyond leading log", JHEP **05**, 051 (2003), arXiv:hep-ph/0302165 [hep-ph].

[66] P. Kovtun, D. T. Son, and A. O. Starinets, "Viscosity in strongly interacting quantum field theories from black hole physics", Phys. Rev. Lett. **94**, 111601 (2005), arXiv:hep-th/0405231 [hep-th].

[67] A. Nakamura, and S. Sakai, "Transport coefficients of gluon plasma", Phys. Rev. Lett. **94**, 072305 (2005), arXiv:hep-lat/0406009 [hep-lat].

[68] H. B. Meyer, "A Calculation of the shear viscosity in SU(3) gluodynamics", Phys. Rev. **D76**, 101701 (2007), arXiv:0704.1801 [hep-lat].

[69] H. B. Meyer, "A Calculation of the bulk viscosity in SU(3) gluodynamics", Phys. Rev. Lett. **100**, 162001 (2008), arXiv:0710.3717 [hep-lat].

[70] N. Christiansen, M. Haas, J. M. Pawlowski, and N. Strodthoff, "Transport Coefficients in Yang–Mills Theory and QCD", Phys. Rev. Lett. **115**, 112002 (2015), arXiv:1411.7986 [hep-ph].

[71] J. Adams, et al., "Experimental and theoretical challenges in the search for the quark gluon plasma: The STAR Collaboration's critical assessment of the evidence from RHIC collisions", Nucl. Phys. **A757**, 102–183 (2005), arXiv:nucl-ex/0501009 [nucl-ex].

[72] K. Adcox, et al., "Formation of dense partonic matter in relativistic nucleus-nucleus collisions at RHIC: Experimental evaluation by the PHENIX collaboration", Nucl. Phys. **A757**, 184–283 (2005), arXiv:nucl-ex/0410003 [nucl-ex].

[73] B. Abelev, et al., "D meson elliptic flow in non-central Pb-Pb collisions at $\sqrt{s_{\rm NN}}$ = 2.76TeV", Phys. Rev. Lett. **111**, 102301 (2013), arXiv:1305.2707 [nucl-ex].

[74] B. B. Abelev, et al., "Azimuthal anisotropy of D meson production in Pb-Pb collisions at $\sqrt{s_{\rm NN}} = 2.76$ TeV", Phys. Rev. **C90**, 034904 (2014), arXiv:1405.2001 [nucl-ex].

[75] H. van Hees, and R. Rapp, "Thermalization of heavy quarks in the quark-gluon plasma", Phys. Rev. **C71**, 034907 (2005), arXiv:nucl-th/0412015 [nucl-th].

[76] G. D. Moore, and D. Teaney, "How much do heavy quarks thermalize in a heavy ion collision?", Phys. Rev. **C71**, 064904 (2005), arXiv:hep-ph/0412346 [hep-ph].

[77] Y. Akamatsu, T. Hatsuda, and T. Hirano, "Heavy Quark Diffusion with Relativistic Langevin Dynamics in the Quark-Gluon Fluid", Phys. Rev. **C79**, 054907 (2009), arXiv:0809.1499 [hep-ph].

[78] G. Aarts, and J. M. Martinez Resco, "Transport coefficients, spectral functions and the lattice", JHEP **04**, 053 (2002), arXiv:hep-ph/0203177 [hep-ph].

[79] S. Gupta, "The Electrical conductivity and soft photon emissivity of the QCD plasma", Phys. Lett. **B597**, 57–62 (2004), arXiv:hep-lat/0301006 [hep-lat].

[80] G. Aarts, C. Allton, J. Foley, S. Hands, and S. Kim, "Spectral functions at small energies and the electrical conductivity in hot, quenched lattice QCD", Phys. Rev. Lett. **99**, 022002 (2007), arXiv:hep-lat/0703008 [HEP-LAT].

[81] H.-T. Ding, A. Francis, O. Kaczmarek, F. Karsch, E. Laermann, and W. Soeldner, "Thermal dilepton rate and electrical conductivity: An analysis of vector current correlation functions in quenched lattice QCD", Phys. Rev. **D83**, 034504 (2011), arXiv:1012.4963 [hep-lat].

[82] G. Aarts, C. Allton, A. Amato, P. Giudice, S. Hands, and J.-I. Skullerud, "Electrical conductivity and charge diffusion in thermal QCD from the lattice", JHEP **02**, 186 (2015), arXiv:1412.6411 [hep-lat].

[83] B. B. Brandt, A. Francis, B. Jäger, and H. B. Meyer, "Charge transport and vector meson dissociation across the thermal phase transition in lattice QCD with two light quark flavors", Phys. Rev. **D93**, 054510 (2016), arXiv:1512.07249 [hep-lat].

[84] H.-T. Ding, O. Kaczmarek, and F. Meyer, "Thermal dilepton rates and electrical conductivity of the QGP from the lattice", arXiv:1604.06712 [hep-lat] (2016).

[85] P. Petreczky, and D. Teaney, "Heavy quark diffusion from the lattice", Phys. Rev. **D73**, 014508 (2006), arXiv:hep-ph/0507318 [hep-ph].

[86] S. Caron-Huot, M. Laine, and G. D. Moore, "A Way to estimate the heavy quark thermalization rate from the lattice", JHEP **04**, 053 (2009), arXiv:0901.1195 [hep-lat].

[87] H. T. Ding, A. Francis, O. Kaczmarek, F. Karsch, H. Satz, and W. Soldner, "Heavy Quark diffusion from lattice QCD spectral functions", J. Phys. **G38**, 124070 (2011), arXiv:1107.0311 [nucl-th].

[88] D. Banerjee, S. Datta, R. Gavai, and P. Majumdar, "Heavy Quark Momentum Diffusion Coefficient from Lattice QCD", Phys. Rev. **D85**, 014510 (2012), arXiv:1109.5738 [hep-lat].

[89] A. Francis, O. Kaczmarek, M. Laine, T. Neuhaus, and H. Ohno, "Nonperturbative estimate of the heavy quark momentum diffusion coefficient", Phys. Rev. **D92**, 116003 (2015), arXiv:1508.04543 [hep-lat].

[90] L. P. Kadanoff, and P. C. Martin, "Hydrodynamic equations and correlation functions", Annals of Physics **24**, 419–469 (1963).

[91] H. B. Meyer, "Transport Properties of the Quark-Gluon Plasma: A Lattice QCD Perspective", Eur. Phys. J. **A47**, 86 (2011), arXiv:1104.3708 [hep-lat].

[92] O. Kaczmarek, F. Karsch, M. Kitazawa, and W. Soldner, "Thermal mass and dispersion relations of quarks in the deconfined phase of quenched QCD", Phys. Rev. **D86**, 036006 (2012), arXiv:1206.1991 [hep-lat].

[93] O. Kaczmarek, "Continuum estimate of the heavy quark momentum diffusion coefficient κ", Nucl. Phys. **A931**, 633–637 (2014), arXiv:1409.3724 [hep-lat].

[94] P. Kovtun, D. T. Son, and A. O. Starinets, "Holography and hydrodynamics: Diffusion on stretched horizons", JHEP **10**, 064 (2003), arXiv:hep-th/0309213 [hep-th].

[95] S. Caron-Huot, and G. D. Moore, "Heavy quark diffusion in perturbative QCD at next-to-leading order", Phys. Rev. Lett. **100**, 052301 (2008), arXiv:0708.4232 [hep-ph].

[96] H.-T. Ding, F. Karsch, and S. Mukherjee, "Thermodynamics of strong-interaction matter from Lattice QCD", Int. J. Mod. Phys. **E24**, 1530007 (2015), arXiv:1504.05274 [hep-lat].

[97] A. Ikeda, M. Asakawa, and M. Kitazawa, "In-medium dispersion relations of charmonia studied by the maximum entropy method", Phys. Rev. D **95**, 014504 (2017), arXiv:1610.07787 [hep-lat].

[98] K. G. Wilson, "Confinement of Quarks", Phys. Rev. **D10**, [,45(1974)], 2445–2459 (1974).

[99] M. Creutz, "Confinement and the Critical Dimensionality of Space-Time", Phys. Rev. Lett. **43**, [Erratum: Phys. Rev. Lett.43,890(1979)], 553–556 (1979).

[100] M. Creutz, and K. J. M. Moriarty, "Numerical Studies of Wilson Loops in SU(3) Gauge Theory in Four-dimensions", Phys. Rev. **D26**, 2166 (1982).

[101] I. Montvay, and G. Münster, *Quantum Fields on a Lattice*, Cambridge Monographs on Mathematical Physics (Cambridge Univ. Press, Cambridge, 1994).

[102] H. J. Rothe, *Lattice gauge theories: an introduction* (World Scientific, Singapore; Hackensack N.J., 2012).

[103] 青木慎也, **格子上の場の理論** (丸善出版, 東京都, Apr. 20, 2012).

[104] H. B. Nielsen, and M. Ninomiya, "Absence of Neutrinos on a Lattice. 1. Proof by Homotopy Theory", Nucl. Phys. **B185**, [,533(1980)], 20 (1981).

[105] H. B. Nielsen, and M. Ninomiya, "Absence of Neutrinos on a Lattice. 2. Intuitive Topological Proof", Nucl. Phys. **B193**, 173–194 (1981).

[106] T. R. Klassen, "The Anisotropic Wilson gauge action", Nucl. Phys. **B533**, 557–575 (1998), arXiv:hep-lat/9803010 [hep-lat].

[107] J. Harada, A. S. Kronfeld, H. Matsufuru, N. Nakajima, and T. Onogi, "O(a) improved quark action on anisotropic lattices and perturbative renormalization of heavy - light currents", Phys. Rev. **D64**, 074501 (2001), arXiv:hep-lat/0103026 [hep-lat].

[108] A. X. El-Khadra, A. S. Kronfeld, and P. B. Mackenzie, "Massive fermions in lattice gauge theory", Phys. Rev. **D55**, 3933–3957 (1997), arXiv:hep-lat/9604004 [hep-lat].

[109] M. Okamoto, et al., "Charmonium spectrum from quenched anisotropic lattice QCD", Phys. Rev. **D65**, 094508 (2002), arXiv:hep-lat/0112020 [hep-lat].

[110] J. Engels, F. Karsch, and T. Scheideler, "Determination of anisotropy coefficients for SU(3) gauge actions from the integral and matching methods", Nucl. Phys. **B564**, 303–324 (2000), arXiv:hep-lat/9905002 [hep-lat].

[111] S. Borsanyi, G. Endrodi, Z. Fodor, S. D. Katz, and K. K. Szabo, "Precision SU(3) lattice thermodynamics for a large temperature range", JHEP **07**, 056 (2012), arXiv:1204.6184 [hep-lat].

[112] S. Aoki, et al., "Quenched light hadron spectrum", Phys. Rev. Lett. **84**, 238–241 (2000), arXiv:hep-lat/9904012 [hep-lat].

[113] J. W. Negele, and H. Orland, *Quantum many-particle systems*, Revised.ver. (Perseus, Reading, MA, Nov. 27, 1998), 476 pp.

[114] J. I. Kapusta, and C. Gale, *Finite-temperature field theory: principles and applications.* (Cambridge University Press, Cambridge, 2006).

[115] R. K. Bryan, "Maximum entropy analysis of oversampled data problems", Eur Biophys J **18**, 165–174 (1990).

[116] M. Asakawa, and M. Kitazawa, "Fluctuations of conserved charges in relativistic heavy ion collisions: An introduction", Prog. Part. Nucl. Phys. **90**, 299–342 (2016), arXiv:1512.05038 [nucl-th].

[117] K.-J. Araki, K. Ohtani, P. Gubler, and M. Oka, "QCD sum rules on the complex Borel plane", PTEP **2014**, 073B03 (2014), arXiv:1403.6299 [hep-ph].

[118] Á. Mócsy, and P. Petreczky, "Can quarkonia survive deconfinement?", Phys. Rev. D **77**, 014501 (2008), arXiv:0705.2559 [hep-ph].

[119] Y. Burnier, and M. Laine, "Towards flavour diffusion coefficient and electrical conductivity without ultraviolet contamination", Eur. Phys. J. **C72**, 1902 (2012), arXiv:1201.1994 [hep-lat].

Acknowledgements

I wish to thank my supervisor professor Masayuki Asakawa very much for the discussions and advises. I am deeply grateful to assistant professor Masakiyo Kitazawa for teaching me and the constant support for this work. I would like to thank associate professor Toru Sato, research associate Yukinao Akamatsu and Satoshi Nakamura, and all colleagues of nuclear theory group at Osaka University for many stimulating discussions and encouragements. Finally I want thank my family.